ABSTRACT

Title of dissertation: SIMULATIONS OF SMALL MASS
                           STRUCTURES IN THE LOCAL
                           UNIVERSE TO CONSTRAIN THE
                           NATURE OF DARK MATTER

                           Emil Polisensky, Doctor of Philosophy, 2014

Dissertation directed by: Professor Massimo Ricotti
                           Department of Astronomy

I use N-body simulations of the Milky Way and its satellite population of dwarf
galaxies to probe the small-scale power spectrum and the properties of the unknown
dark matter particle. The number of dark matter satellites decreases with decreasing
mass of the dark matter particle. Assuming that the number of dark matter satellites
exceeds or equals the number of observed satellites of the Milky Way, I derive a
lower limit on the dark matter particle mass of $m_{WDM} > 2.1$ keV for a thermal dark
matter particle, with 95% confidence. The recent discovery of many new dark matter
dominated satellites of the Milky Way in the Sloan Digital Sky Survey allows me to
set a limit comparable to constraints from the complementary methods of Lyman-α
forest modeling and X-ray observations of the unresolved cosmic X-ray background
and of halos from dwarf galaxy to cluster scales.

I also investigate the claim that the largest subhalos in high resolution dissi-
pationless cold dark matter (CDM) simulations of the Milky Way are dynamically
inconsistent with observations of its most luminous satellites. I quantify the ef-

fects of the adopted cosmological parameters on the satellite densities and show the tension between observations and simulations adopting parameters consistent with WMAP9 is greatly diminished. I explore warm dark matter (WDM) cosmologies for 1–4 keV thermal relics. In 1 keV cosmologies subhalos have circular velocities at kpc scales 60% lower than their CDM counterparts, but are reduced by only 10% in 4 keV cosmologies. Recent reports of a detected X-ray line in emission from galaxy clusters has been argued as evidence of sterile neutrinos with properties similar to a 2 keV thermal relic. If confirmed, my simulations show they would naturally reconcile the densities of the brightest satellites and be consistent with the abundance of ultra-faint dwarfs.

I conclude by using N-body simulations of a large set of dark matter halos in different CDM and WDM cosmologies to demonstrate that the spherically averaged density profile of dark matter halos has a shape that depends on the power spectrum of initial conditions. Virialization isotropizes the velocity dispersion in the inner regions of the halo but does not erase the memory of the initial conditions in phase space. I confirm that the slope of the inner density profile in CDM cosmologies depends on the halo mass with more massive halos exhibiting steeper profiles. My simulations support analytic models of halo structure that include angular momentum and argue against a universal form for the density profile.

SIMULATIONS OF SMALL MASS STRUCTURES IN THE LOCAL UNIVERSE TO CONSTRAIN THE NATURE OF DARK MATTER

by

Emil Joseph Polisensky

Dissertation submitted to the Faculty of the Graduate School of the
University of Maryland, College Park in partial fulfillment
of the requirements for the degree of
Doctor of Philosophy
2014

Advisory Committee:
Professor Massimo Ricotti, Chair/Advisor
Professor Kevork Abazajian
Professor Michael Boylan-Kolchin
Professor Jordan Goodman
Professor Cole Miller

Preface

"Who can argue against the glories of art, music, and literature that existed long before science did? And what can science offer us to compare with such beauty?

For one thing, it is possible to point out that the vision of the Universe made apparent by the careful labor of four centuries of modern scientists far outweighs in beauty and majesty (for those who would take the trouble to look) all the creations of all human artists put together, or all the imaginings of mythologists, for that matter."

–Isaac Asimov, *Best Foot Backward*

The material presented in this thesis has been published in three refereed journal articles:

E. Polisensky, M. Ricotti, 2011, "Constraints on the dark matter particle mass from the number of Milky Way satellites," PhRvD, 83, 4

E. Polisensky, M. Ricotti, 2014, "Massive Milky Way satellites in cold and warm dark matter: dependence on cosmology," MNRAS, 437, 2922

E. Polisensky, M. Ricotti, 2014, "Fingerprints of the initial conditions on the density profiles of cold and warm dark matter haloes," MNRAS, (to be submitted)

I have given four talks on this material:

E. Polisensky, M. Ricotti, 2014, "Too Big To Fail: A Sensitive Test of Cosmological Parameters and Dark Matter Properties," 223rd Meeting of the American Astronomical Society, 408.03, Washington, DC, January 2014

E. Polisensky, M. Ricotti, K. Keating, K. Holley-Bockelmann, G. Langston, "Constraints on Particle Mass and the Origins of HI Clouds with Dark Matter Simulations," Near Field Cosmology as a Probe of Dark Matter, Early Universe and Gravity, Annapolis, MD, 29 November - 1 December 2011

E. Polisensky, M. Ricotti, "Constraints on Particle Mass and the Origins of HI Clouds with Dark Matter Simulations", GUN meeting, College Park, MD, 20 April 2012

E. Polisensky, M. Ricotti, "Constraints on Warm Dark Matter from the Local Group of Galaxies," Nuclear Particle Astrophysics and Cosmology Lunch, Physics Dept. UMD, College Park, MD, 21 April 2011

The material in Chapter 3 was chosen for a featured article in the 2011 yearly review of research and development projects at the Naval Research Laboratory. Fewer than 10% of submitted abstracts and chosen for inclusion in the review, and only five of those for featured articles.

E. Polisensky, M. Ricotti, "Constraining the Very Small with the Very Large: Particle Physics and the Milky Way," 103, 2011 NRL Review

The images in Figures 3.3, 4.2, and 4.3 were created with software I developed myself for visualizing N-body simulations.

Dedication

To the next generation, may you be better fitted to this world than the current.

Acknowledgments

This thesis is the culmination of a long journey that would not have been possible without the support of many people.

I'd like to thank my advisor, Professor Massimo Ricotti for teaching me about and giving me a chance to do research in the field of cosmology. I also thank the members of my committee for their service and suffering through the reading of a document of this length.

I owe an immeasurable debt to my supervisors, Dr. Namir Kassim and Dr. Kurt Weiler, at the Naval Research Laboratory for allowing me to participate in the Edison Memorial Graduate Training Program and attend school while employed. Without their continued support, and incredible patience, I never would've made it.

I also owe a great many thanks to Dr. William Erickson for setting me on the right path and getting this journey started. And even further back, many thanks to Dr. Paul Krehbiel for taking a young undergrad under his wing. If I had a second lifetime I'd be a lightning researcher.

Additional thanks to the high performance computing support staff at the Air Force Research Lab, U.S. Army Engineer Research and Development Center, and the University of Maryland. Without their assistance I wouldn't have made it very far beyond saying hello to the world.

To my wife for all her love and support and sharing the waking nightmare of being a graduate student while holding a full-time job. To my family and friends for sharing a sense of humor and helping the days go by. To my coworkers at NRL

who make it an enjoyable place to work and the wonderful secretarial staff for help

dealing with the never ending harassment of paperwork.

Table of Contents

List of Tables

List of Figures

Chapter 1: Science Motivation and Structure of Thesis

Evidence that the majority of gravitating mass in the universe is composed of an unseen form was first presented by Zwicky in the 1930s (Zwicky 1933, 1937). By measuring the line of sight velocities of galaxies in clusters the dynamical mass to light ratio was determined $M/L > 100$, and is more than an order of magnitude greater than typical of the older stellar populations found in elliptical galaxies, $M/L \sim 10$.

The first imaging X-ray observatories discovered most baryonic matter in clusters is in the form of hot gas unbound to member galaxies. This gas emits bremsstrahlung radiation at X-ray energies. If the cluster is relaxed and the gas in hydrostatic equilibrium it can be used as a probe of the gravitational potential (Fabricant et al. 1980; Böhringer 1995). Cluster masses have been determined from the gas density and temperature, determined from the X-ray emissivity and spectral cutoff, and confirms the high mass to light ratios in these systems.

Further evidence comes from the flat rotation curves observed in galaxies (Rubin et al. 1978). The circular velocity v at radius R depends on the enclosed mass M, $v^2 = GM/R$. For the rotation curve to be flat the mass must increase linearly with distance but the distribution of light from stars and gas drops off much more

rapidly. The mass to light ratio increases rapidly in outer parts of galaxies indicating most of the matter in galaxies is dark.

Secondary evidence comes from simulations of interacting galaxies that cannot produce the tidal tails observed unless galaxies have extended halos of dark matter (Dubinski et al. 1996). Simulations have also shown dark matter halos are needed to stabilize the disks of spiral galaxies against bar formation (Ostriker and Peebles 1973).

Several lines of evidence point to a non-baryonic composition for dark matter. The rate of neutron capture in the early era of universal nucleosynthesis is dependent on the density of baryons and the resulting abundance of light elements (Deuterium, Helium, Lithium, and Beryllium) are also sensitive to the amount of baryonic matter. Measurements of the primordial abundances of these elements show baryonic matter can only account for about 17% of the mass in the universe (Cooke et al. 2014).

Non-baryonic dark matter is also required to form galaxies below cluster scales. The Cosmic Microwave Background (CMB) is the primordial radiation at redshift $z \sim 1000$ when the baryonic plasma recombined and decoupled from the radiation, allowing the photons to propagate freely. The CMB is observed to be highly homogenous with temperature variations of only 10^{-5}. Prior to this epoch the baryonic matter was coupled to the radiation field by Compton scattering and would have density fluctuations of the same magnitude as the temperature fluctuations. Adiabatic perturbations grow proportional to $(1 + z)$ in the matter dominated era. Density variations on the order of one are seen at the current time on 8 Mpc scales. To produce overdensities of one today the perturbations must be on the order of

10^{-3} at $z \sim 1000$, much greater than the observed temperature fluctuations. Non-baryonic dark matter perturbations are required to provide the seeds for galaxy formation since they dynamically decouple from the radiation earlier and grow for a longer period of time.

An alternative explanation for the observed dynamics of galaxies and clusters is a modification to the theory of gravity at the small accelerations observed on large scales (Milgrom 1983). However, observations of the merging cluster 1E 0657-558 show that due to the merger the dominant baryonic component, the collisional X-ray emitting gas, has been displaced from the collisionless stellar component. Gravitational lensing was used to map the gravitational potential and show the source of gravity traces the auxiliary galaxies, providing empirical evidence that dark matter exists and is collisionless in nature (Clowe et al. 2006).

Cosmology has entered an age of precision where studies of the CMB, supernovae, and cluster surveys have determined the cosmological parameters to $\lesssim 10\%$. The universe is geometrically flat and composed of approximately 4% baryonic matter, 23% dark matter, and 73% dark energy (Hinshaw et al. 2012). Additionally, the recently reported detection of polarization in the B-mode power spectrum of the CMB is consistent with gravitational waves from an early era of inflation (BICEP2 Collaboration et al. 2014). Many nonbaryonic particles are predicted to exist in proposed extensions to the standard model of particle physics. Many of these models (but not all) predict the dark matter to be composed of weakly interacting massive particles (WIMPs) with masses ~ 100 GeV. These particles decouple from the other particle species in the early universe with non-relativistic velocities

and represent a class of models called cold dark matter (CDM). Recently, excessive gamma rays with energies $1 - 5$ GeV have been observed from the Galactic Center (GC) region by the Fermi Gamma-ray Space Telescope and claimed as evidence for WIMPs of mass ~ 30 GeV annihilating to quarks (Goodenough and Hooper 2009; Hooper and Goodenough 2011; Daylan et al. 2014). Gamma ray spectral lines have been observed at 110 and 130 GeV toward the GC and in observations of clusters (Su and Finkbeiner 2012; Weniger 2012; Finkbeiner et al. 2013; Hektor et al. 2013) and have also been claimed as evidence of WIMP annihilations, although of WIMPs with a different mass. Before either of these signals can be confidently attributed to dark matter other astrophysical explanations have to be ruled out (Abazajian and Kaplinghat 2012; Abazajian et al. 2014; Finkbeiner et al. 2013). Despite very sensitive searches, direct detection experiments have been unsuccessful in discovering the dark matter particle (LUX Collaboration et al. 2013). All particle theories for dark matter are based on extrapolations beyond the range of energies explored experimentally. In the absence of direct detection cosmological studies offer the important possibility of constraining theories of elementary particles at ultra-high energies.

Cold dark matter models have been extremely successful at describing the large scale features of matter distribution in the universe but face potential problems on sub-Mpc scales. CDM predicts numbers of satellite galaxies for Milky Way-sized halos about an order of magnitude in excess of the number observed (Klypin et al. 1999; Moore et al. 1999a). Also, there is a dynamical discrepancy between high-resolution CDM simulations and observations of the stellar velocities in the most

luminous satellites (Boylan-Kolchin et al. 2011, 2012a). Additional issues include the number of galaxies in voids and observed density cores in low surface brightness and dwarf galaxies (van den Bosch and Swaters 2001; Swaters et al. 2003; Weldrake et al. 2003; Donato et al. 2004; Gentile et al. 2005; Simon et al. 2005; Gentile et al. 2007; Salucci et al. 2007; Kuzio de Naray et al. 2010).

One solution to the issues with CDM is the power spectrum of density fluctuations may be truncated which can arise if the dark matter particles are "warm" with masses ~ 1 keV. Warm dark matter (WDM) particles have relativistic velocities in the early universe and only become nonrelativistic when less than a Galactic mass ($\sim 10^{12} M_\odot$) is within the horizon. Streaming motions while the particles are still relativistic can erase density fluctuations on sub-Galactic scales and reduce the number of satellites in Milky Way-sized galaxies as well as the number of galaxies in voids. Halo formation on dwarf scales is also delayed in WDM resulting in lower densities for the brightest satellites in agreement with the observations.

WDM models are also useful for exploring the role of substructure and mergers in determining the structural and dynamical profiles of relaxed halos. It is generally accepted that the density profiles of halos are universal in form with all information about the initial conditions and assembly history erased in the process of virialization. However, some analytic models and simulation studies have found a dependence of the inner profile on the power spectrum with a flattening of the inner profile with decreasing halo mass.

A frequently studied class of WDM particles are thermal relics. These particles couple to the relativistic cosmic plasma in the early universe and achieve thermal

equilibrium prior to the time of their decoupling. A candidate for a thermal relic WDM particle is the gravitino, the superpartner of the graviton in supersymmetry theories. The lightest stable particle (LSP) in supersymmetry theories is a natural dark matter candidate. If the scale where supersymmetry is spontaneously broken is $\lesssim 10^6$ GeV, as predicted by theories where supersymmetry breaking is mediated by gauge interactions, then the gravitino is likely to be the lightest stable particle and can have a mass reaching into the keV regime (Gorbunov et al. 2008). Galaxy formation in gravitino cosmologies was first investigated by Blumenthal et al. (1982).

In general WDM particles may have decoupled before achieving thermal equilibrium or may already be decoupled from the cosmic plasma at the time of their production. These WDM particle models are called nonthermal relics. An example of a nonthermal WDM relic is the sterile neutrino (see Kusenko 2009 and references therein), a theoretical particle added to standard electroweak theory. Sterile neutrinos have been proposed (Gninenko 2010; Gninenko and Gorbunov 2010; Karagiorgi et al. 2009; Sorel et al. 2004; Melchiorri et al. 2009; Maltoni and Schwetz 2007; Päs et al. 2005; Akhmedov and Schwetz 2010) as an explanation for the anomalous excess of oscillations observed between muon and electron neutrinos and antineutrinos (Athanassopoulos et al. 1995, 1996, 1998a,b; Aguilar-Arevalo et al. 2007, 2009, 2010). There have been recent reports of the detection of a X-ray emission line in the spectrum of galaxy clusters consistent with a decay line from sterile neutrinos of mass $m_s = 7.1 \pm 0.7$ keV (Bulbul et al. 2014; Boyarsky et al. 2014). Abazajian (2014) calculated the transfer function for one of the sterile neutrino production mechanisms and showed it approximates that of a thermal particle of mass ~ 2 keV. This

detection is provisional but if confirmed has important implications for the observations of small scale structure in the local universe, as my work in this thesis will show.

There are also ways other than WDM to reduce small scale power. Broken-scale invariance inflation models (Kamionkowski and Liddle 2000) have a cutoff length below which power is suppressed. Particle theories where the LSP dark matter particle arises from the decay of the next lightest supersymmetric particle (NLSP) can also suppress small scale power if the NLSP is charged and coupled to the photon-baryon plasma (Sigurdson and Kamionkowski 2004) or if the NLSP decay imparts a large velocity to the LSP (Kaplinghat 2005). Further possibilities include composite dark matter models where stable charged heavy leptons and quarks bind to helium nuclei by Coulomb attraction and can play the role of dark matter with suppression of small scale density fluctuations (Khlopov 2005, 2006; Belotsky et al. 2006a,b; Khlopov and Kouvaris 2008a,b; Khlopov 2008). Wilkinson et al. (2013) showed CDM with a non-zero elastic scattering cross section with photons can reduce power at small scales. The method used in this work could potentially be applied to constrain these models as well, however, I do not examine the consequences my work has on these theories.

I review in Chapter 2 the foundations of structure formation in an expanding universe and the dependence of that structure on the nature of the dark matter. I show in Chapter 3 how the faint population of dwarf satellites discovered in the Sloan Digital Sky Survey (SDSS) allow an improved lower limit to be set on the dark matter particle mass. I study the effects of WDM on the densities of the largest

satellites in Chapter 4 and quantify the dependence of the densities on the adopted cosmological parameters. I conclude in Chapter 5 by using WDM simulations to examine the claim that the virialization process in gravitationally collapsed dark matter halos erases all information about the initial conditions from which they form.

Chapter 2:   Foundations of Structure Formation

2.1   Cosmological Principle

Most cosmological models rely on the Cosmological Principle that on suffi-
ciently large scales the universe is homogeneous and isotropic. Since gravity is the
dominant force on large scales every cosmological model requires a theory of gravity.
Modern cosmology uses general relativity which is a geometric theory that makes
gravity a property of space-time. The geometry of space-time is given by the met-
ric tensor and related to the mass-energy content given by the energy-momentum
tensor. In colloquial terms, mass-energy affects the curvature of space-time while
the curvature of space-time affects how mass-energy moves. The interval ds^2 be-
tween two events in space-time depends on the metric. For a universe in which
the Cosmological Principle applies space-time can be taken to be a continuous fluid
with geometric properties described by the Robertson-Walker metric in comoving
spherical polar coordinates:

$$ds^2 = c^2 dt^2 - a^2(t) \left[\frac{dr^2}{1 - Kr^2} + r^2 \left(d\theta^2 + \sin^2 \theta d\phi^2 \right) \right], \qquad (2.1)$$

where $a(t)$ is the time variable scale factor and related to the observable redshift
$a/a_0 = (1 + z)^{-1}$, where a_0 is the scale factor at present. K is the curvature

9

parameter and is -1, 0, and 1, for open, flat, and closed universes, respectively. It is useful to characterize the expansion rate with the Hubble parameter, $H \equiv \dot{a}/a$, where the dot represents a derivative with respect to proper time. In a flat universe the proper distance is simply the comoving distance scaled by the scale factor and it is convenient to set the present value of the scale factor $a_0 = 1$. The Hubble parameter at the current epoch then measures the universal expansion rate at the current time and is ≈ 70 km s^{-1} Mpc^{-1}. It is conventional to express the Hubble parameter at the current time in terms of a dimensionless parameter h: $H_0 = 100h$ km s^{-1} Mpc^{-1}, with $h = 0.7$.

2.2 Friedmann Equations

For universes described by the Robertson-Walker metric, Einstein's field equations of general relativity can be written in the form of the Friedmann Equations:

$$\ddot{a} = -\frac{4\pi G a}{3}\left(\rho + 3\frac{P}{c^2}\right) + \frac{\Lambda c^2 a}{3} \tag{2.2}$$

$$\dot{a}^2 + Kc^2 = \frac{8\pi G}{3}\rho a^2 + \frac{\Lambda c^2 a^2}{3} \tag{2.3}$$

for a perfect fluid of inertial mass density ρ and pressure P with a cosmological constant Λ. It is useful to define the critical density, $\rho_c = 3H^2/8\pi G$, and the density parameter for each fluid component $\Omega_X = \rho_X/\rho_c$. The total density of mass-energy Ω is the sum of the individual components, radiation Ω_r, matter Ω_m, curvature Ω_K, and cosmological constant Ω_Λ. The second equation can be written in terms of the

10

Hubble parameter:

$$H^2 = H_0^2 \left[\Omega_{0r} \left(\frac{a}{a_0} \right)^{-4} + \Omega_{0m} \left(\frac{a}{a_0} \right)^{-3} + \Omega_{0K} \left(\frac{a}{a_0} \right)^{-2} + \Omega_{0\Lambda} \right], \qquad (2.4)$$

where "0" indicates values at the current time. The curvature term in a flat universe is zero.

In this form the Friedmann equation can readily be solved for the evolution of the scale factor with time when one component is dominant. In a matter dominated universe $a = a_0 \, (3/2 \, H_0 \sqrt{\Omega_{0m}} \, t \,)^{2/3}$. In a radiation dominated universe $a = a_0 \, (2 H_0 \sqrt{\Omega_{0r}} \, t \,)^{1/2}$. A cosmological constant dominated universe grows exponentially, $a = a_0 \, e^{H_0 \sqrt{\Omega_{0\Lambda}} t}$.

The dependence of the matter and radiation densities on the scale factor can be determined from thermodynamics. For a system with volume V and pressure P expanding adiabatically the change in internal energy E is equal to the work done by the system, $dE = -PdV$. This equation can be solved for $\rho(a)$ if the pressure is known since $V \propto a^3$ and $E = \rho c^2 V$. For non-relativistic matter, $P = 0$, and $\rho_m = \rho_{0m} a^{-3}$. For radiation and relativistic matter, $P = \rho c^2/3$, and $\rho_r = \rho_{0r} a^{-4}$. The radiation dominates the density of the universe at early times when the scale factor is small, but it dilutes faster than matter resulting in an epoch of equality between the matter and radiation densities after which matter dominates. This is an important epoch and is given by $1 + z_{eq} = 2.6 \times 10^4 \, \Omega_{0m} h^2$.

Different regions of the universe can only communicate by causal processes when they are within each other's particle horizon. The particle horizon is given by:

$$R_H(t) = a(t) \int_0^t \frac{c \, dt'}{a(t')}. \qquad (2.5)$$

11

When the universe is radiation dominated the particle horizon is $R_H = 2ct \propto a^2$, while in the matter dominated regime $R_H = 3ct \propto a^{3/2}$. These results have important consequences for the growth of density perturbations.

2.3   Jeans Instability

The condition for a self-gravitating region to be unstable to gravitational collapse was first analyzed by Jeans (1902) in the context of star formation. Jeans found there is a minimum mass for collapse determined by the condition that the free fall time is less than the sound crossing time. His analysis also applies to cosmological density perturbations with the exception that the expanding background slows the rate of collapse from exponential to a power law.

The equations of motion for a self-gravitating fluid in a smooth background with velocity and pressure fields $\vec{v}$ and P, and gravitational potential ϕ are:

$$\frac{\partial \rho}{\partial t} + \nabla \cdot \rho\,\vec{v} \ = \ 0 \tag{2.6}$$

$$\frac{\partial \vec{v}}{\partial t} + (\vec{v} \cdot \nabla)\,\vec{v} + \frac{1}{\rho}\nabla P + \nabla\phi \ = \ 0 \tag{2.7}$$

$$\nabla^2\phi - 4\pi G\rho \ = \ 0. \tag{2.8}$$

Small perturbations are then applied to the fields: $\phi = \phi_0 + \delta\phi$, $\vec{v} = \vec{v_0} + \delta\vec{v}$, $\rho = \rho_0 + \delta\rho$, $P = P_0 + \delta P$. The equations of motion are expanded to first order in small quantities and the solutions for the unperturbed field subtracted. The density contrast is defined as $\delta \equiv \delta\rho/\rho$, and the adiabatic sound speed is given by $v_s^2 = \delta P/\delta\rho$. Wave solutions are sought for δ of the form $\delta = \delta_0 e^{i(\vec{k}\cdot\vec{r}-\omega t)}$, which give

the wave equation in an expanding background:

$$\ddot{\delta} + 2\left(\frac{\dot{a}}{a}\right)\dot{\delta} = \delta(4\pi G\rho_0 - k^2 v_s^2) \tag{2.9}$$

The scale separating gravitational collapse from internal pressure supported stability is the same as for a static medium with $\dot{a} = 0$. This gives the dispersion relation for wave solutions:

$$\omega^2 = v_s^2 k^2 - 4\pi G\rho_0 \tag{2.10}$$

The scale separating collapse from stability is given by $\omega = 0$ and is called the Jeans scale. The Jeans scale is expressed in terms of wavelength, $\lambda = 2\pi/k$:

$$\lambda_J = v_s \left(\frac{\pi}{G\rho_0}\right)^{1/2}. \tag{2.11}$$

Gravitational collapse occurs when $\lambda > \lambda_J$, otherwise the perturbations oscillate in density as sound waves with angular frequency ω.

There are two solutions for the growth rate of perturbations above the Jeans scale, a growing mode and a decaying mode. In the matter dominated era the decaying mode $\delta \propto t^{-1}$ and quickly becomes unimportant. The growing mode solution is $\delta \propto t^{2/3}$. Since $a = (3/2\,H_0\,t)^{2/3}$, the amplitude of the density contrast grows linearly with the scale factor in the matter dominated era, $\delta \propto a$.

In the radiation dominated era the Jeans analysis must be conducted for a relativistic fluid with $P = \rho c^2/3$ and $v_s = c/\sqrt{3}$. In this case the growing mode solution is $\delta \propto t$. Since $a = (2H_0\,t)^{1/2}$, the amplitude of the density contrast grows with the square of the scale factor in the radiation dominated era, $\delta \propto a^2$. The sound speed for radiation is a constant making the Jeans mass proportional to $\rho^{-1/2}$. Since

13

$\rho_r \propto a^{-4}$ and $a \propto t^{1/2}$, the Jeans scale is a linear function of time in the radiation era and grows at the same rate as the horizon scale.

In an expanding universe the Jeans length is time dependent and perturbations can switch between stability and growth depending on when they enter the horizon and which component is dominating the inertial mass of the universe. This has important consequences for the development of perturbations. It must be noted the Jeans analysis is valid only for collisional particles such as baryons. For dark matter the collisionless Boltzmann equation must be solved. If the phase space distribution of particles is Maxwellian the result is similar to Equation 2.11 but with the sound speed replaced with the particle thermal velocity dispersion. Dark matter particles can free-stream out of overdense regions and damp perturbations on the smallest scales, as discussed in the next section.

2.4   The Power Spectrum

Models of the inflation epoch predict the field of density perturbations, $\delta(\vec{x})$, at the end of inflation will be adiabatic and Gaussian random with statistically independent wave modes and random phases. A Gaussian random field is completely described by its power spectrum.

The Fourier transform of the density perturbation field is given by:

$$\delta(\vec{x}) = \frac{1}{(2\pi)^3} \int \delta_{\vec{k}} \, \mathrm{e}^{-i\vec{k}\cdot\vec{x}} d^3k. \tag{2.12}$$

Applying Parseval's Theorem that the integral of the square of a function is equal

to the integral of the square of its Fourier transform:

$$\int \delta^2(\vec{x})d^3x = \frac{1}{(2\pi)^3}\int |\delta_{\vec{k}}|^2 d^3k. \tag{2.13}$$

The left hand term is the mean square amplitude of density fluctuations, $\langle\delta^2\rangle$. On the right hand side, $|\delta_{\vec{k}}|^2$, is the power spectrum of the perturbation field written $P(k)$. Thus,

$$\langle\delta^2\rangle = \frac{1}{(2\pi)^3}\int P(k)d^3k. \tag{2.14}$$

Inflation models give a primordial power spectrum at the end of inflation $P(k) \propto k^{n_s}$ with $n_s \approx 1$. The power spectrum is altered from its primordial form by the changes in the horizon scale and Jeans scale during the radiation era.

In the radiation dominated era both the horizon scale and the Jeans scale are of the same magnitude and scale at the same rate. Density perturbations outside the horizon grow linearly with time until they enter the horizon. When they enter the horizon they become smaller than the Jeans scale and growth stops. Baryonic perturbations are coupled to the radiation via Compton scattering and oscillate with the radiation as sound waves. Dark matter perturbations do not oscillate but their growth is stalled because the radiation dominates the inertial mass. This is called the Meszaros effect (Meszaros 1974). At the epoch of equality the dynamics of the expansion and the inertial mass become dominated by the matter. Dark matter perturbations within the horizon resume their growth while perturbations just entering the horizon continue to grow uninterrupted. The baryonic plasma, however, remains coupled to the radiation where the Jeans scale reaches a peak value at equality and remains nearly constant until recombination. Baryonic perturbations

less than the horizon scale at equality continue to oscillate until the epoch of recombination and experience Silk damping due to photon diffusion. After recombination the baryonic Jeans scale drops and perturbations are regenerated as they fall into the potential wells of the perturbations in the dark matter. The Meszaros effect causes the power spectrum of density fluctuations to peak at the horizon scale at equality and turnover at smaller scales. This can be seen in the power spectrum plotted in Figure 2.1.

In hot and warm dark matter models the dark matter particles decouple from the other particle species with relativistic velocities allowing them to stream out of overdense regions as they enter the horizon in the radiation dominated era. These streaming motions damp perturbations below the horizon scale at the time the particles become non-relativistic resulting in a truncation in the power spectrum. The scale of the truncation is related to the mass of the dark matter particle with lighter particles decoupling earlier and able to stream longer. Although they are non-relativistic when they decouple, CDM particles have a small streaming scale due to their non-zero thermal velocities. The damping scale of CDM perturbations is about a Jupiter mass on a scale approximately that of the Solar System (to the distance of the Oort Cloud; Green et al. 2004; Loeb and Zaldarriaga 2005). Figure 2.1 shows the effects of streaming on the power spectrum for cold, warm, and hot dark matter (HDM) cosmologies. HDM models damp perturbations up through cluster scales and are ruled out observationally.

The changes in the linear power spectrum from its primordial form caused by the physics of the early universe are parameterized by a transfer function, $T(k) \in$
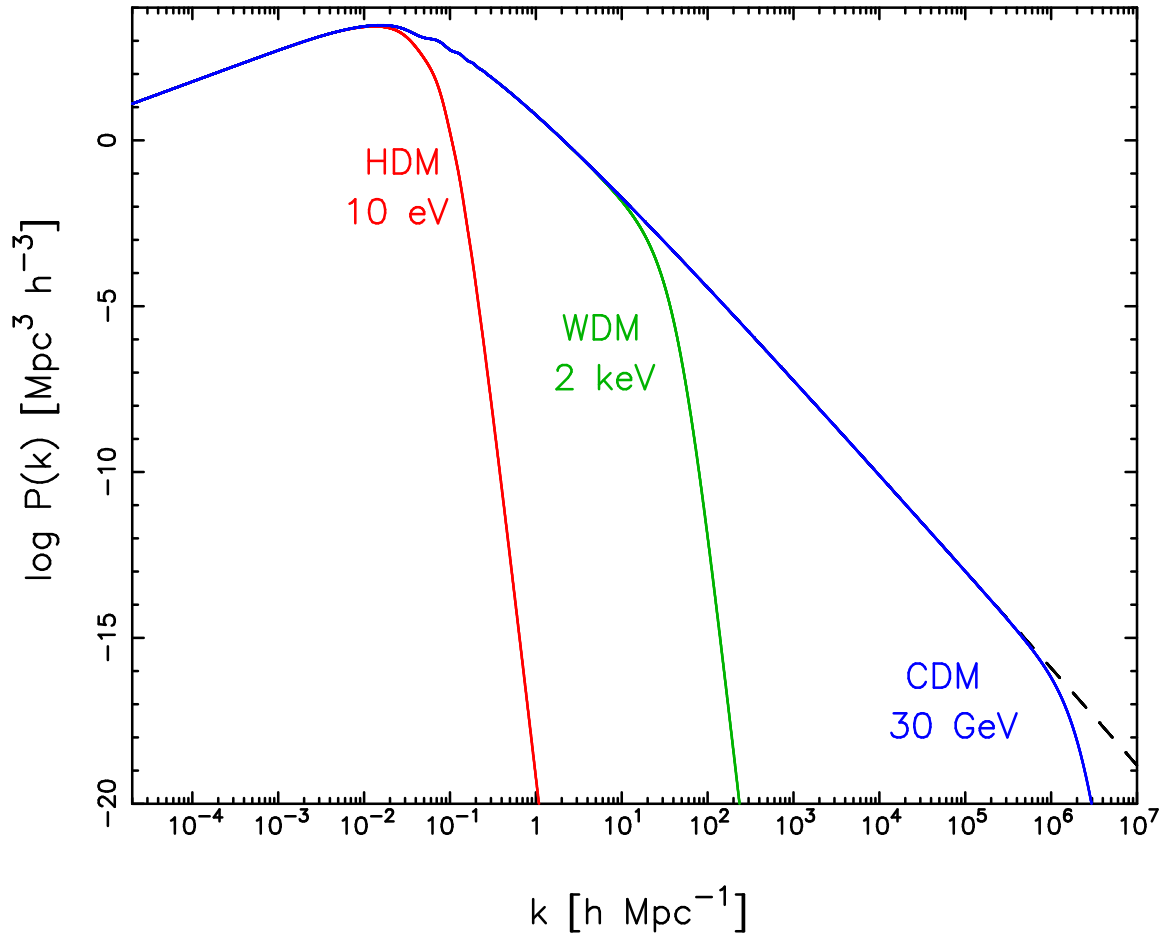
Figure 2.1: Power spectra for cold, warm, and hot dark matter cosmologies. The dashed line shows the ideal cold dark matter condition of zero thermal velocities.

[0, 1]. At any time t the power spectrum is given by:

$$P(k,t) = T^2(k) \frac{D^2(t)}{D^2(t_0)} P_i(k), \qquad (2.15)$$

where P_i is the primordial power spectrum at the end of the inflation era and D is the linear growth factor at time t normalized by its value at present. The transfer function can be calculated numerically with software such as CAMB (Lewis and Bridle 2002), CMBFAST (Seljak and Zaldarriaga 1996), and LINGER (Bertschinger 2001); or by using fitting functions that are accurate to a few percent (Eisenstein and Hu 1998). In practice the transfer function in Equation 2.15 is calculated for the ideal CDM case with zero thermal velocities. In WDM models the ideal CDM power spectrum is used but weighted by a second transfer function to account for the effects of streaming.

Normalization of the power spectrum is determined observationally, either from observations of the CMB or by the standard deviation of perturbations on 8 Mpc scales at the present epoch, σ_8.

The variance of perturbations on a comoving spatial scale R at time t is:

$$\sigma^2(R) = \langle |\delta_R^2| \rangle = \frac{1}{2\pi^2} \frac{D^2(t)}{D^2(t_0)} \int_0^\infty P(k)\, W(k)\, k^2\, dk, \qquad (2.16)$$

where $W(k)$ is a window function in Fourier space and can be chosen to be a top hat. On most scales the power spectrum can be approximated as a power law in k over the filtered scales, $P(k) \propto k^n$:

$$\sigma^2(R) \propto \int_0^{1/R} P(k) k^2 dk \propto \int_0^{1/R} k^{n+2} dk \propto R^{-(n+3)} \qquad (2.17)$$

18

Since $R^3 \propto M$, the variance can be given in terms of mass scales:

$$\sigma^2 \propto R^{-(n+3)} \propto M^{-(n+3)/3} \tag{2.18}$$

In CDM cosmologies $n > -3$ and smaller scales have larger variance resulting in bottom-up galaxy formation with smaller halos collapsing first. In WDM the power spectrum below the truncation scale has $n < -3$, smaller scales have smaller variance leading to top-down galaxy formation where the first structures to form are just above the streaming scale. In the next section it is shown how the variance can be used to calculate the mass function of collapsed halos at any epoch.

2.5   Abundance of Dark Matter Halos

A method for estimating the number density of dark matter halos and the fraction of matter in halos of a given mass at any time was pioneered by Press and Schechter (1974). An outline of their method is given below.

The probability, P, that different regions with the same mass M will have perturbation amplitudes between δ and $\delta + d\delta$ is a Gaussian distribution with zero mean and variance $\sigma^2(M)$:

$$\mathrm{P}(\sigma)d\delta = \frac{1}{\sqrt{2\pi\sigma^2}}\, \mathrm{e}^{-\delta^2/2\sigma^2} d\delta \tag{2.19}$$

The fraction of collapsed perturbations, Ω_c, at scale M is found by integrating the probability distribution above the collapse criterion δ_c:

$$\Omega_c = \int_{\delta_c}^{\infty} \mathrm{P}(\delta)d\delta = \frac{1}{2}\left[1 - \mathrm{erf}\left(\frac{\delta_c}{\sqrt{2}\sigma(M)}\right)\right], \tag{2.20}$$

$$\mathrm{erf}(x) = \frac{2}{\sqrt{\pi}}\int_0^x \mathrm{e}^{-t^2} dt \tag{2.21}$$

The criterion for collapse in linear theory is given by $\delta_c = 1.69$.

Equation 2.20 needs to be multiplied by a factor of two because it does not account for underdense regions that collapse when they are embedded within a larger volume above the collapse criterion. This was shown with excursion set formalism by Bond et al. (1991).

The collapsed fraction per halo mass is found by differentiating:

$$\frac{d\Omega_c}{dM} = -\sqrt{\frac{2}{\pi}}\frac{\delta_c}{\sigma^2}\frac{d\sigma}{dM}e^{-\delta_c^2/2\sigma^2} \tag{2.22}$$

The number density of halos per mass is found from $Mdn = \bar{\rho}d\Omega_c$:

$$\frac{dn}{dM} = \bar{\rho}\sqrt{\frac{2}{\pi}}\frac{\delta_c}{M\sigma^2}\frac{d\sigma}{dM}e^{-\delta_c^2/2\sigma^2} \tag{2.23}$$

The number density is characterized by an exponential cutoff at high masses and $dn/dM \propto M^{-2}$ at small masses in CDM. In WDM, streaming motions erase perturbations below the streaming scale and reduce the abundances of small mass halos. This fact is used in Chapter 3 where the Milky Way satellites are used to set limits on the streaming scale.

2.6 Beyond Linear Theory - Spherical Halo Collapse

An overdense sphere can be treated like a closed universe with $K = 1$ in the Robertson-Walker metric and provides a simple model for the nonlinear evolution of a density perturbation. The Friedmann equations have parametric solutions leading to the well-known result that closed universes have oscillatory behavior, expanding to a maximum then contracting in a Big Crunch to a single point.

The equations of motion for the sphere's radius is the same as for the scale factor of a closed universe. For a matter dominated universe the equations for the proper radius of the sphere and time are:

$$r = A(1 - \cos\theta) \qquad t = B(\theta - \sin\theta) \tag{2.24}$$

$$A = \frac{\Omega_0}{2(\Omega_0 - 1)} \qquad B = \frac{\Omega_0}{2H_0(\Omega_0 - 1)^{3/2}} \tag{2.25}$$

These equations can be solved for the nonlinear evolution of the density contrast and compared to the extrapolations of linear theory. Expanding the equations to fifth order in θ gives the linear approximation:

$$\delta \simeq \frac{3}{20}\left(\frac{6t}{B}\right)^{2/3} \tag{2.26}$$

The turnaround point where the sphere stops expanding and begins collapsing is at $\theta = \pi$. The density enhancement within the sphere is $\delta = 9\pi^2/16 \simeq 5.55$. Extrapolation of linear theory predicts $\delta_{lin} = (3/20)(6\pi)^{2/3} \simeq 1.06$.

The sphere collapses to a point at $\theta = 2\pi$ with density contrast $\delta = (6\pi)^2/2 \simeq 178$. Extrapolating linear theory to this time gives $\delta_{lin} = (3/20)(12\pi)^{2/3} \simeq 1.69$. This is the collapse criterion used in the Press-Schechter formalism of the last section.

In practice real structures will not collapse to a singularity because the assumptions of no internal pressure and no shell crossing will be violated. Dynamical processes will result in an extended, gravitationally bound halo in an equilibrium satisfying the virial theorem, described in the next section. The radius enclosing a density contrast of 178 is called the virial radius of the halo and the enclosed mass is called the halo virial mass.

2.6.1   The Virial Theorem

For a system of N point particles of mass m_i and Cartesian coordinates $(x_i,$ $y_i,$ $z_i)$ interacting only through gravity the moment of inertia, I, for the system is given by:

$$I = \sum_{i=1}^{N} m_i(x_i^2 + y_i^2 + z_i^2) \tag{2.27}$$

Differentiating twice with respect to time gives:

$$\frac{1}{2}\ddot{I} = 2\sum_{i=1}^{N} \frac{m_i}{2}\left(\dot{x}_i^2 + \dot{y}_i^2 + \dot{z}_i^2\right) + \sum_{i=1}^{N} m_i\left(x_i\ddot{x}_i + y_i\ddot{y}_i + z_i\ddot{z}_i\right) \tag{2.28}$$

The first summation on the right is a summation over the kinetic energy of each particle and gives the total kinetic energy of the system, K. In the second summation on the right, the components of the force vector can be recognized $(m_i\ddot{x}_i, m_i\ddot{y}_i, m_i\ddot{z}_i)$. The forces are generated as the gradient of the gravitational potential, U:

$$m_i\ddot{x}_i = -\frac{\partial U}{\partial x_i}, \quad m_i\ddot{y}_i = -\frac{\partial U}{\partial y_i}, \quad m_i\ddot{z}_i = -\frac{\partial U}{\partial z_i} \tag{2.29}$$

The second term can then be written:

$$\sum_{i=1}^{N} m_i(x_i\ddot{x}_i + y_i\ddot{y}_i + z_i\ddot{z}_i) = -\sum_{i=1}^{N}\left(x_i\frac{\partial U}{\partial x_i} + y_i\frac{\partial U}{\partial y_i} + z_i\frac{\partial U}{\partial z_i}\right) = U \tag{2.30}$$

The last part of this expression uses the fact that the potential is inversely proportional to distance, making it a homogeneous function of order $n = -1$. Applying Euler's theorem for homogeneous functions, $x_i\partial f/\partial x_i = nf$, shows that the second term is simply the total gravitational potential energy of the system.

For a system near equilibrium, $\ddot{I} = 0$, and Equation 2.28 becomes:

$$2K + U = 0 \tag{2.31}$$

This is the important virial theorem that for a system of self-gravitating particles in equilibrium the absolute value of the potential energy is equal to twice the kinetic energy.

Dark matter halos in simulations are seldom in complete equilibrium and it is useful to define a "virial ratio" as:

$$\frac{2K}{|U|} - 1 \tag{2.32}$$

as a metric of the halo relaxation. This is used in Chapter 5.

2.6.2 The NFW Profile

The seminal work of Navarro et al. (1997, 1996) found that the density structure of relaxed dark matter halos are well represented by what has become known as the NFW profile:

$$\rho(r) = \frac{\rho_s}{(r/r_s)(1 + r/r_s)^2}, \tag{2.33}$$

where $\rho(r)$ is the density in a spherical shell at distance r from the halo center. By scaling the free parameters r_s and ρ_s, which define a characteristic length and density, the NFW profile can fit dark matter halos from dwarf galaxy to cluster scales.

Defining a halo concentration as the ratio of the virial radius to r_s, the concentration was found to correlate with mass such that smaller mass halos are more concentrated. This was understood as a consequence of the earlier formation epoch of small mass halos in the bottom-up structure formation of CDM. Since small halos collapse earlier their inner regions reflect the higher universal density of matter at

earlier times. Reducing the power spectrum, either by changing the cosmological parameters or by introducing a truncation, delays halo formation to later epochs and reduces halo concentrations.

I investigate how dark matter models affect the concentration of the largest Milky Way satellites in Chapter 4. I explore in Chapter 5 the effects of erasing small scale perturbations on the mass and dynamical profiles of collapsed halos in detail.

2.7 Beyond Linear Theory - Simulations

Linear theory breaks down when $\delta \sim 1$. Phases of the Fourier modes become non-Gaussian and cross-talk between modes affects the power spectrum of perturbations. In the non-linear regime N-body simulations must be employed. N-body simulations use high performance computing techniques to numerically integrate the equations of motion for particles started from small initial perturbations in the linear regime.

Initial conditions for starting simulations are generated using the Zeldovich approximation (Zel'dovich 1970) relating the density perturbation field to the positions and velocities of a distribution of particles. The initial time t_i is chosen by the resolution of the simulation so that the smallest scales are in the linear regime. The initial conditions employed in my simulations are generated from a uniform grid of point masses. Random unit vectors are generated for each particle and multiplied by $\sqrt{P(k, t_0)}D(t_i)/D(t_0)$ to give δ_k. The velocity field in Fourier space is determined from δ_k and inverse Fourier transformed to get the spatial velocity

field. Displacements from the uniform grid for each particle are then determined from $\Delta x = \vec{v}(x_i, t_i)t_i$. Initial conditions for both CDM and WDM are generated by adopting the appropriate power spectrum $P(k, t_0)$.

Chapter 3:   Particle Mass Constraints from Subhalo Abundances

3.1   Overview

The cold dark matter paradigm has been extremely successful at describing the large scale features of matter distribution in the Universe but has problems on small scales. Below the Mpc scale CDM predicts numbers of satellite galaxies for Milky Way-sized halos about an order of magnitude in excess of the number observed. This is the 'missing satellites' problem (Klypin et al. 1999; Moore et al. 1999a). One proposed solution is that, due to feedback mechanisms, some dark matter satellites do not form stars and remain nonluminous dark halos (Efstathiou 1992; Thoul and Weinberg 1996; Bullock et al. 2001b; Ricotti and Ostriker 2004; Ricotti et al. 2005). Another solution is the power spectrum of density fluctuations may be truncated which may arise if the dark matter is warm (particle mass ~ 1 keV) instead of cold (particle mass ~ 1 GeV). WDM particles have relativistic velocities in the early Universe and only become nonrelativistic when about a Galactic mass ($\sim 10^{12} M_\odot$) is within the horizon. Streaming motions while the particles are still relativistic can erase density fluctuations on sub-Galactic scales and reduce the number of satellites. WDM models have been studied by a number of authors (Colín et al. 2000; Avila-Reese et al. 2001; Bode et al. 2001; Knebe et al. 2002, 2003; Zentner

and Bullock 2003; Maccio' and Fontanot 2009) in relation to the missing satellites problem and other issues with CDM such as the apparent density cores in spiral and dwarf galaxies (van den Bosch and Swaters 2001; Swaters et al. 2003; Weldrake et al. 2003; Donato et al. 2004; Gentile et al. 2005; Simon et al. 2005; Gentile et al. 2007; Salucci et al. 2007; Kuzio de Naray et al. 2010).

N-body simulations of WDM cosmologies are complicated by the formation of artificial halos produced by the discrete sampling of the gravitational potential with a finite number of particles (see Melott 2007 for a review). Matter perturbations collapse and form filaments with nonphysical halos separated by a distance equal to the mean particle spacing (see Fig. 3.1) (Wang and White 2007; Melott 2007). These halos are numerical artifacts. These halos may survive disruption as they accrete from filaments onto Milky Way-sized halos and may contaminate the satellite abundances and distributions in WDM simulations.
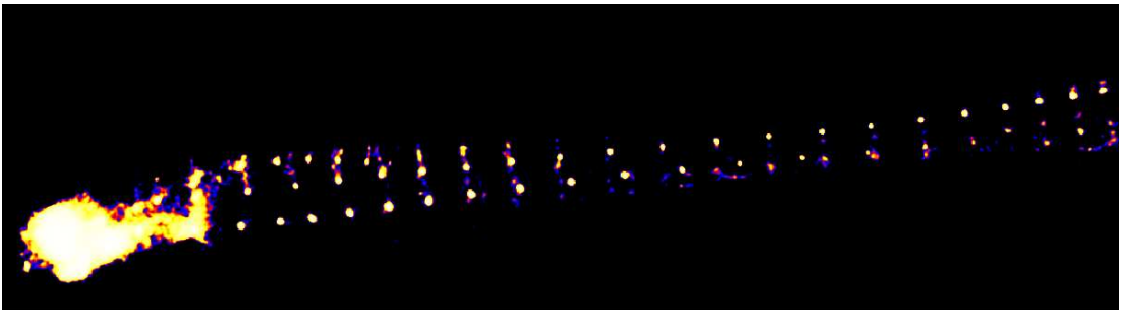
Figure 3.1: Nonphysical halos formed along a filament and accreting onto a larger halo at $z = 1$ in a WDM simulation ($m_{WDM} = 1$ keV). These halos are numerical artifacts.

In the past decade, 16 new dwarf spheroidal galaxies have been discovered in

the Sloan Digital Sky Survey (Castander 1998; see Table 3 and references therein). After correcting for completeness the estimated number of Milky Way (MW) satellites is > 60 (see Sec. 3.3.3). These new dwarfs have low luminosities, low surface brightnesses, and most appear to be dark matter dominated. Since the number of dark matter halos must be greater than or equal to the number of observed satellites, the new data from the SDSS may provide improved limits on the mass of the dark matter particle independent of complementary techniques.

Motivated by the recent increase in the number of observed Milky Way satellites, I have performed new simulations of the growth of Milky Way-like galaxies in CDM and WDM cosmologies for a variety of WDM particle masses. My goal is to constrain the dark matter particle mass by comparing the number of satellite halos in the simulated Milky Ways to the observed number of luminous satellites for the actual Milky Way. Maccio' and Fontanot (2009) combined N-body simulations with semianalytic models of galaxy formation to compare the simulated and observed Milky Way satellite luminosity functions for CDM and WDM cosmologies. I do not make any assumptions on how dark matter halos are populated with luminous galaxies in this work. I simply impose that the number of observed satellites is less than or equal to the number of dark matter halos for a range of Galactocentric radii. This guarantees a robust lower limit on the dark matter particle mass.

3.2 Simulations

All my simulations were conducted with the N-body cosmological simulation code GADGET2 (Springel 2005) assuming gravitational physics only. Values for cosmological parameters were adopted from the third year release of the WMAP mission (Spergel et al. 2007), $(\Omega_m, \Omega_\Lambda, h, \sigma_8, n_s) = (0.238, 0.762, 0.73, 0.751, 0.951)$ to facilitate comparison with the Via Lactea II (VL2) simulation (Diemand et al. 2008). For each simulation set a single realization of the density field was produced in the same periodic, comoving volume but with the power spectrum of fluctuations varied appropriately for CDM and WDM cosmologies. Initial conditions were generated on a cubic lattice using the GRAFIC2 software package (Bertschinger 2001). The power spectra for CDM and WDM are given by

$$P_{CDM}(k) \;\; \propto \;\; k^{n_s} T_{CDM}^2, \tag{3.1}$$

$$P_{WDM}(k) \;\; = \;\; P_{CDM} T_{WDM}^2, \tag{3.2}$$

respectively, with the normalization of P_{CDM} determined by σ_8. For the *set A* and *set B* simulations (described below) the transfer function for CDM adiabatic fluctuations given by Bardeen et al. (1986) (BBKS) was used:

$$T_{CDM}(k) = \frac{\ln(1 + 2.34q)}{2.34q} \left[1 + 3.89q + (16.1q)^2 + (5.46q)^3 + (6.71q)^4 \right]^{-0.25}, \tag{3.3}$$

where $q = k/(\Omega_m h^2)$. A potential problem with the BBKS transfer function is that it underestimates power on large scales. In Appendix A I investigate the effect that this choice for the CDM transfer function may have on the number of Milky Way

satellites. I run one of the simulations adopting the transfer functions from Eisenstein and Hu (1998) and find that this does not affect the results on the number of satellites. Additional CDM simulations (*set C*) were run using the transfer function calculated by the LINGER program in the GRAFIC2 package ($\Omega_b = 0.04$ was used for calculating the effects of baryons on the matter transfer function). LINGER integrates the linearized equations of general relativity, the Boltzmann equation, and the fluid equations governing the evolution of scalar metric perturbations, photons, neutrinos, baryons, and CDM. The mass and circular velocity functions of satellites are consistent across both transfer functions.

Assuming the WDM to be a thermal particle, a particle like the gravitino that was in thermal equilibrium with the other particle species at the time of its decoupling, the transfer function valid for thermal particles given by Bode et al. (2001) was used:

$$T_{WDM}(k) = [1 + (\alpha k/h)^\nu]^{-\mu}, \tag{3.4}$$

where $\nu = 2.4$, $\mu = 4.167$ and

$$\alpha = 0.0516 \left(\frac{m_{WDM}}{1 \text{ keV}}\right)^{-1.15} \left(\frac{\Omega_m}{0.238}\right)^{0.15} \left(\frac{h}{0.73}\right)^{1.3} \left(\frac{g_X}{1.5}\right)^{-0.29}. \tag{3.5}$$

The parameter g_X is the number of degrees of freedom for the WDM particle, conventionally set to the value for a light neutrino species: $g_X = 1.5$. The parameter k is the spatial wavenumber in Mpc^{-1} and m_{WDM} is the mass of the WDM particle in keV.

If the dark matter is composed of non-thermal particles like the sterile neutrino the situation is more complicated. There are several mechanisms by which sterile

neutrinos can be produced. In the standard mechanism proposed by Dodelson and Widrow (DW; Dodelson and Widrow 1994), sterile neutrinos are produced when oscillations convert some of the more familiar active neutrinos into the sterile variety. The amount produced depends on the sterile neutrino mass and the mixing angle but such details are not considered here and when analyzing the results for sterile neutrinos it is simply assumed they compose the entirety of the dark matter. The transfer function for DW sterile neutrinos with mass m_s is given by (Abazajian 2006):

$$T_s(k) = [1 + (\alpha k/h)^\nu]^{-\mu}, \tag{3.6}$$

where $\nu = 2.25$, $\mu = 3.08$, and

$$\alpha = 0.1959 \left(\frac{m_s}{1 \text{ keV}}\right)^{-0.858} \left(\frac{\Omega_m}{0.238}\right)^{-0.136} \left(\frac{h}{0.73}\right)^{0.692}. \tag{3.7}$$

Viel et al. (2005) give a scaling relationship between the mass of a thermal particle and the mass of the DW sterile neutrino for which the transfer functions are nearly identical:

$$m_s = 4.379 \text{ keV} \left(\frac{m_{WDM}}{1 \text{ keV}}\right)^{4/3} \left(\frac{\Omega_m}{0.238}\right)^{-1/3} \left(\frac{h}{0.73}\right)^{-2/3}. \tag{3.8}$$

Other sterile neutrino production mechanisms include that proposed by Shi & Fuller (SF; Shi and Fuller 1999) who showed the DW mechanism is altered in the presence of a universal lepton asymmetry where production can be enhanced by resonance effects. Sterile neutrinos can also be produced from decays of gauge-singlet Higgs bosons at the electroweak scale (Kusenko 2006). The momentum distribution of the sterile neutrinos depends on the production mechanism. In the absence of transfer function calculations the expressions in Kusenko (2009) for the free streaming length

and average momentum are used to derive approximate scaling factors for the SF and Higgs produced sterile neutrinos: $m_{DW}/m_{SF} = 1.5$, $m_{DW}/m_{Higgs} = 4.5$.

In my simulations I assume the dark matter is thermal and scale the results to the standard sterile neutrino mass using Eq. (3.8). The initial conditions include particle velocities due to the gravitational potential using the Zeldovich approximation but I do not add random thermal velocities appropriate for WDM to the simulation particles. Bode et al. (2001) argue that for warm particle masses greater than 1 keV thermal motions are unimportant for halos on scales of a kiloparsec and above. Regardless, it is expected thermal motions, if anything, would reduce the number of small mass halos and by not including thermal motions the mass limits derived from my simulations will be more conservative.

Simulations were conducted for CDM and WDM cosmologies with particle masses of $m_{WDM} = 1$, 2, 3, 4, and 5 keV ($m_s = 4.4$, 11.0, 18.9, 27.8, 37.4 keV). Figure 3.2 shows the power spectra for these cosmologies along with the spectrum for an 11 keV standard sterile neutrino using Eq. (3.8). Two separate sets of simulations were run, both consisting of a comoving cubic box 90 Mpc on a side. *Set A* consisted of 204^3 particles giving a 'coarse' particle mass of 3.0×10^9 M$_\odot$ and a force resolution of 8.8 kpc. All force resolutions were fixed in comoving coordinates. The HOP halo finding software (Eisenstein and Hut 1998) was used at $z = 0$ to identify Milky Way-sized halos with masses $1 - 2 \times 10^{12} M_\odot$. Halos were examined visually, one was chosen that was at least several Mpc away from clusters and other large structures so as to be relatively isolated. Its particles were identified in the initial conditions and a cubic refinement level, 6.2 Mpc on a side, was placed on the region. For

the refinement region in the low resolution simulations $11,239,424$ (224^3) particles were used with mass and force resolutions of $7.3 \times 10^5 M_\odot$ and 550 pc, respectively. Higher resolution simulations were run for CDM and WDM particle masses of 1, 2, and 4 keV with $89,915,392$ (448^3) particles in the refinement region and mass and force resolutions of $9.2 \times 10^4 M_\odot$ and 275 pc, respectively. The simulated Milky Way halo had a neighbor halo with mass $0.23 M_{MW}$ at a distance of 700 kpc in the low resolution simulations. The real Milky Way has a massive neighbor in M31, the Andromeda galaxy ($M_{M31} \sim 1 - 3 M_{MW}$), at a distance ~ 700 kpc. Being nonlinear and chaotic systems, small perturbations to the trajectories of dark matter halos can be amplified exponentially and in the higher resolution simulation this satellite is merging with the Milky Way at $z = 0$. Such a merger may disrupt the equilibrium of the halo and make it nonrepresentative of the actual Milky Way. The difference between the high and the low resolution simulations is significant and complicates the comparison between the resolutions; however, this merger is not a violation of the selection method used for the *set C* halos described below and excellent agreement is found across all simulation sets.

The need to explore the scatter between the subhalo distributions of different realizations of Milky Way-type halos, in addition to the complications arising with the high and low resolution simulations of *set A*, prompted a second set of simulations to be conducted. *Set B* consisted of 408^3 particles giving a coarse particle mass of $3.8 \times 10^8 M_\odot$ and a force resolution of 4.4 kpc. HOP was again used to identify halos with masses $0.8 - 2.2 \times 10^{12} M_\odot$. For each halo the nearest neighboring halo with mass $> 0.8 \times 10^{12} M_\odot$ was also found. A halo whose nearest massive neighbor
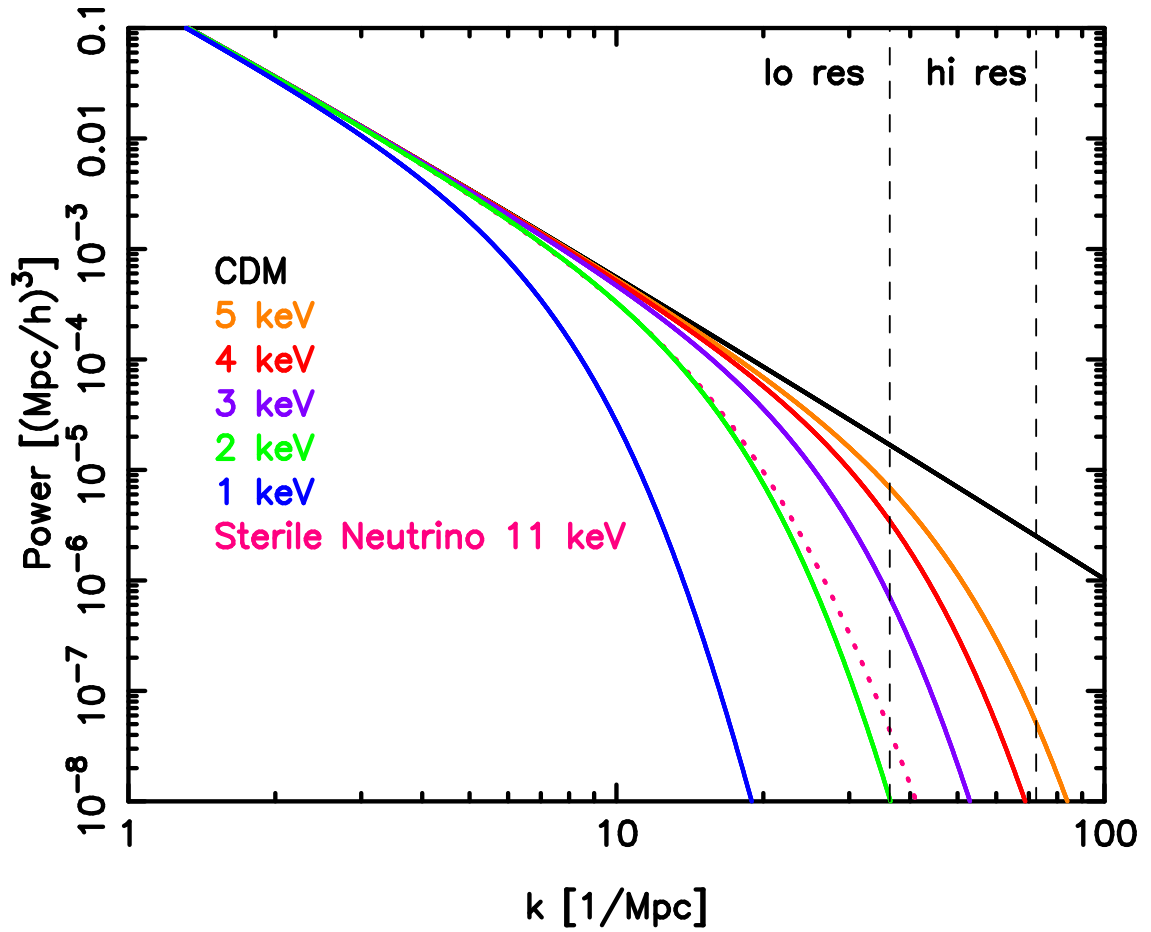
Figure 3.2: Power spectra for the simulations. The dotted line is the power spectrum for an 11 keV standard sterile neutrino Abazajian (2006). The neutrino spectrum is approximately the same as a 2 keV thermal particle, validating the scaling relation of Viel et al. (2005). The vertical dashed lines indicate the lattice cell size in the high and low resolution refinement levels.

was at least 5 Mpc away was selected and visually verified that the halo was indeed isolated. A rectangular refinement level $6.1 \times 7.0 \times 7.9$ Mpc was placed over this halo's particles in the initial conditions. Low and high resolutions were conducted with the same mass and force resolutions as *set A*. The low resolution simulations used $16,515,072 \, (\sim 255^3)$ particles in the refinement level while high resolution used $132,120,576 \, (\sim 510^3)$ particles in the refinement level. Figure 3.3 shows portraits of the Milky Way and the surrounding environment in the *set B* high resolution simulations.

A third set of CDM only, low resolution simulations was run to further explore the scatter between the subhalo distributions of different realizations of Milky Way-type halos and to explore the possibility of a bias introduced by the use of the BBKS transfer function. *Set C* consisted of 408^3 particles but the CDM transfer function was generated from the LINGER software in GRAFIC2 (Bertschinger 2001) after correcting a bug where the power spectrum for baryons was used for dark matter when calculating the transfer function. AMIGA's Halo Finder (AHF) software (Knollmann and Knebe 2009) was used to find MW-sized halos with no equal sized neighbor within two virial radii (defined below). Nine halos were selected for refinement at low resolution from a variety of environments, low density with few large halos to high density with many large halos. The rectangular refinement regions had lengths $7.5 - 15.8$ Mpc and $31,752,192 - 69,009,408 \, (316^3 - 410^3)$ particles.
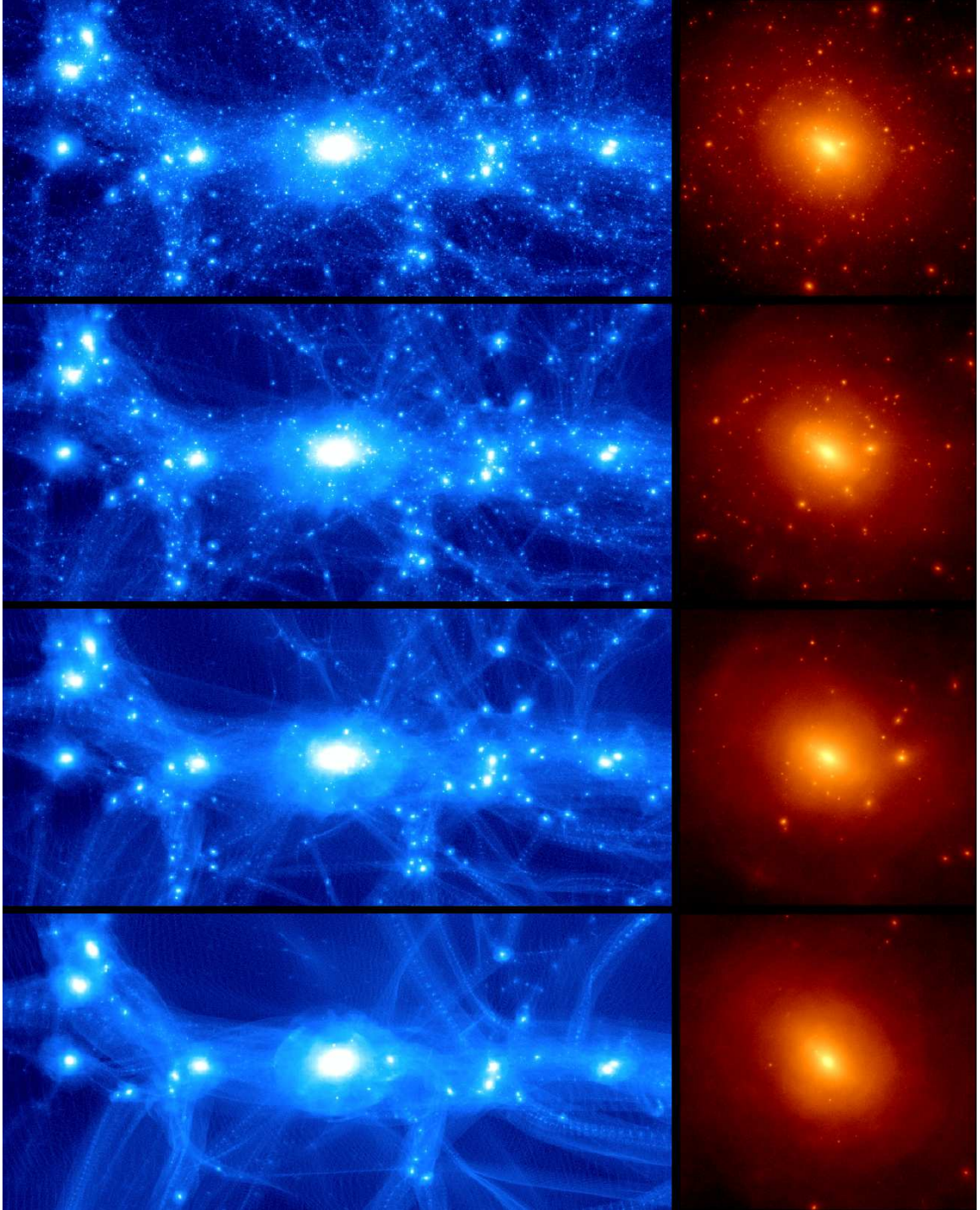
Figure 3.3: Portraits of the *set B* simulated Milky Way halo at $z = 0$ in the high resolution simulations. From top to bottom: CDM, 4 keV, 2 keV, 1 keV. The images at left are 4.5 Mpc × 2 Mpc centered on the Milky Way. Structures within 300 kpc of the MW center are shown at right.

Table 3.1 summarizes the properties calculated by AHF for all simulated Milky Way halos at $z = 0$. R_Δ is defined as the radius enclosing an overdensity Δ times the critical value. The mass and number of particles inside R_Δ are M_Δ and N_Δ, respectively; v_Δ is the circular velocity $v_\Delta^2 \equiv GM_\Delta/R_\Delta$ at R_Δ, and v_{max} is the maximum circular velocity of the halo. The value $\Delta = 178\Omega_m^{0.4} = 100$ is used (Eke et al. 1996; which is also very close to the value using the definition from Bryan and Norman 1998) for the virial radius of the MWs and subhalos within R_{100} are considered when comparing to other published work. The mass, radius, and velocity at $\Delta = 50$ are also used in the literature and these values are also listed in Table 3.1.

Figure 3.4 shows the density profiles of the A and B Milky Way halos calculated by breaking the halos into spherical shells. Small differences between the high and low resolution *set A* halos caused by the merging neighbor are apparent but generally the profiles are very similar across all simulations of each set. An inner flattening of the halos in the WDM simulations is not seen because thermal motions were not added to the simulation particles. If the gamma-ray excess observed by *Fermi* is due to annihilating ~ 30 GeV WIMPs, Daylan et al. (2014) showed the signal within $5°$ of the Galactic Center is consistent with a typical NFW-like density profile with inner slope ~ -1.2. In this case, Figure 3.4 shows CDM particles could have a truncated power spectrum at dwarf-scales and be consistent with the *Fermi* data.

Table 3.1: Properties of simulated Milky Way halos.

Simulation	M_{100} $[10^{12}M_\odot]$	R_{100} [kpc]	M_{50} $[10^{12}M_\odot]$	R_{50} [kpc]	v_{50} [km/s]	v_{max} [km/s]	N_{100}	N_{50}
			Set A					
CDM lo	1.4867	288.25	1.6786	378.47	138.11	183.02	$2,026,414$	$2,287,923$
5 keV lo	1.4964	288.86	1.6825	378.75	138.22	183.38	$2,039,597$	$2,293,239$
4 keV lo	1.5060	289.45	1.6833	378.82	138.24	183.87	$2,052,643$	$2,294,398$
3 keV lo	1.5141	290.00	1.6850	378.95	138.29	182.98	$2,063,747$	$2,296,714$
2 keV lo	1.5100	289.74	1.6702	377.84	137.88	181.59	$2,058,104$	$2,276,518$
1 keV lo	1.4983	289.00	1.6615	377.18	137.64	180.04	$2,042,264$	$2,264,672$
CDM hi	1.8403	309.49	2.0331	403.43	147.22	191.94	$20,067,182$	$22,169,072$
4 keV hi	1.8261	308.70	2.0383	403.77	147.34	189.69	$19,911,999$	$22,225,367$
2 keV hi	1.8326	309.06	2.0266	402.99	147.06	183.82	$19,982,705$	$22,098,268$
1 keV hi	1.8373	309.33	2.0244	402.85	147.01	179.39	$20,033,935$	$22,073,940$
			Set B					
CDM lo	1.9005	312.84	2.1325	409.89	149.58	195.87	$2,590,475$	$2,906,549$
5 keV lo	1.8862	312.04	2.1254	409.44	149.41	195.76	$2,570,982$	$2,896,920$
4 keV lo	1.8863	312.04	2.1212	409.16	149.32	195.84	$2,570,992$	$2,891,165$
3 keV lo	1.8800	311.70	2.1185	409.00	149.25	195.75	$2,562,445$	$2,887,566$
2 keV lo	1.8479	309.92	2.0936	407.38	148.67	195.24	$2,518,690$	$2,853,610$
1 keV lo	1.8263	308.70	2.0752	406.19	148.23	192.33	$2,489,258$	$2,828,485$
CDM hi	1.7533	304.53	1.9948	400.88	146.29	194.01	$19,117,720$	$21,751,717$
4 keV hi	1.7426	303.92	1.9781	399.75	145.88	188.52	$19,001,776$	$21,569,680$
2 keV hi	1.7288	303.11	1.9640	398.81	145.53	185.18	$18,850,480$	$21,415,983$
1 keV hi	1.6230	296.80	1.8655	392.01	143.06	179.59	$17,697,389$	$20,341,369$
			Set C					
CDM lo 1	2.4814	342.19	2.8071	449.22	163.93	214.42	$3,351,495$	$3,761,164$
CDM lo 2	2.3512	336.10	2.8287	450.37	164.35	213.86	$3,204,746$	$3,855,526$
CDM lo 3	1.9846	317.63	2.2133	415.01	151.45	203.23	$2,705,093$	$3,016,787$
CDM lo 4	2.2587	331.63	2.6486	440.60	160.79	199.95	$3,078,658$	$3,610,116$
CDM lo 5	1.7665	305.53	1.9226	345.21	154.77	193.06	$2,382,645$	$2,589,405$
CDM lo 6	1.6004	295.64	1.8977	394.26	143.88	187.76	$2,174,733$	$2,567,693$
CDM lo 7	1.8704	311.41	2.7754	447.52	163.31	187.56	$2,549,352$	$3,782,898$
CDM lo 8	1.9858	317.70	2.3401	422.78	154.29	194.43	$2,706,610$	$3,189,609$
CDM lo 9	1.6881	300.95	1.8936	393.97	143.77	201.23	$2,300,887$	$2,581,006$
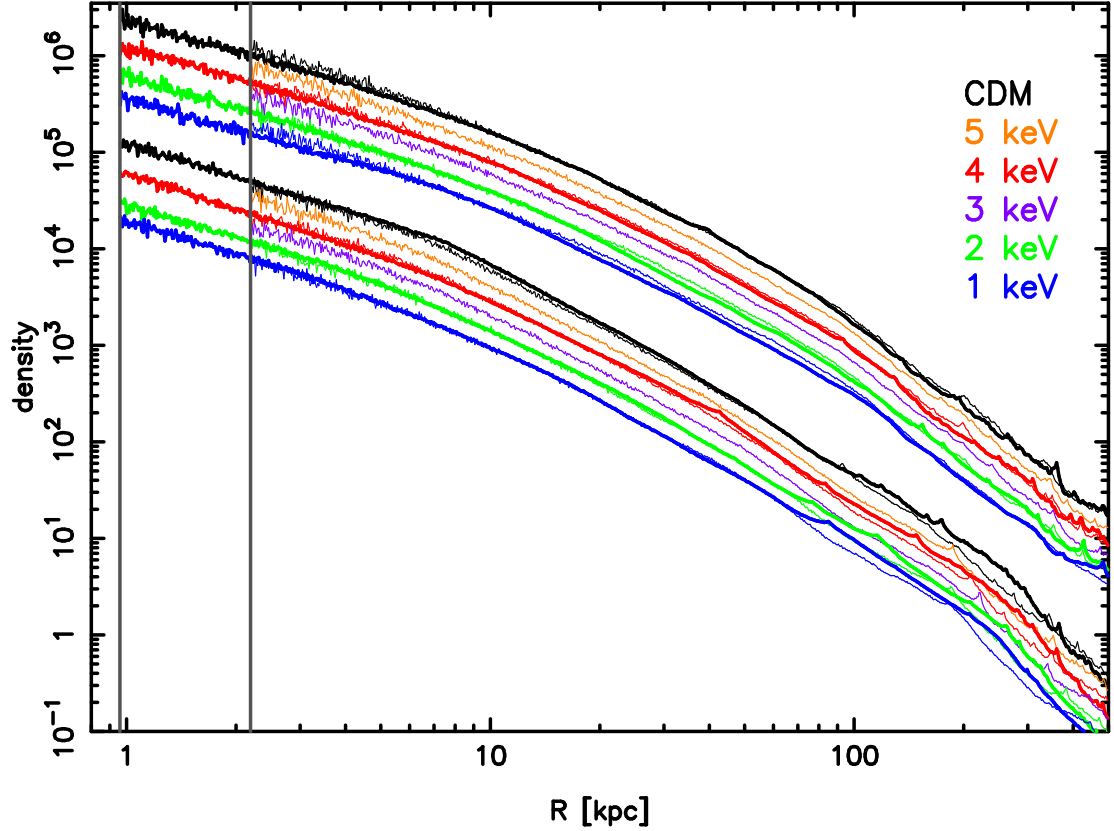
Figure 3.4: Density profile of Milky Way halos in the *set A* and *set B* CDM and WDM simulations. Thick lines are the high resolution simulations. *Set B* simulations are at top, the *set A* and the WDM cosmologies in each set have been offset downward for clarity. The profiles are plotted starting from the convergence radius of Power et al. (2003) for both resolutions (vertical lines).

3.2.1 Identification of Satellites

The AHF halo finding software (Knollmann and Knebe 2009) was used to find the gravitationally bound dark matter halos in my N-body simulations. Unbound particles were iteratively removed and gravitationally bound halos with ten or more particles were selected.

AHF calculates properties of the halos it finds such as the total mass and the maximum circular velocity. For this study the maximum circular velocity is a better characteristic of a subhalo than the mass because quantifying the outer boundary of a subhalo embedded in a larger halo is somewhat arbitrary and can introduce systematic errors. The maximum circular velocity however typically occurs at a radius well inside the subhalo outskirts.

3.3 Results

3.3.1 Satellite Distribution Functions

I first compare my CDM simulations to other CDM simulations in the literature. Figure 3.5 shows the cumulative mass functions, $N(> M_{sub})$, for subhalos within R_{50} for the *set A* and *B* MWs. Poisson statistic error bars have been added to the high resolution simulations and fit by $N \propto M^{-\beta}$. The values of β (0.9 and 0.95) agree with other published work that find values of $0.7 - 1.0$ (Moore et al. 1999a; Ghigna et al. 2000; Helmi et al. 2002; Gao et al. 2004; De Lucia et al. 2004; van den Bosch et al. 2005; Diemand et al. 2007; Giocoli et al. 2008; Springel et al.

2008). At both high and low resolution the simulated mass functions turn away from the fit at masses below about 200 times the mass resolution of the simulation in agreement with the Via Lactea simulation (Diemand et al. 2007). Also plotted are the mass functions for the *set C* simulations. The subhalo abundances of the *set A* and *B* halos are within the halo to halo scatter and are consistent with the *set C* simulations.

The cumulative maximum circular velocity functions for subhalos within R_{100} are plotted in Figure 3.6. The maximum velocities of the subhalos have been normalized by the maximum circular velocity of their host MW. The shaded region shows the minimum and maximum (lighter) and $\pm 1\sigma$ (darker) from the mean of the 68 halos with masses $1.5 - 3 \times 10^{12} M_\odot$ in the simulation of Ishiyama et al. (2009). I use the fit to the density profile of the Via Lactea II halo (Diemand et al. 2008) to estimate its R_{100} (298 kpc) and from the published subhalo catalog I calculate and plot the Via Lactea II velocity function as the dashed line. The solid straight line is the fitting formula from the Bolshoi simulation (Klypin et al. 2011),

$$N(> x) \;\; = \;\; 1.7 \times 10^{-3} v_{max,host}^{1/2} x^{-3}, \tag{3.9}$$

$$x \;\; \equiv \;\; v_{max}/v_{max,host}, \tag{3.10}$$

applied to the high resolution halos which provides an excellent fit (the difference between the fit for the *set A* and *B* $v_{max,host}$ is less than the thickness of the line). Via Lactea II used the same cosmological parameters as the simulations conducted here and their subhalo abundance is in good agreement. My simulations are consistent with the Ishiyama et al. simulation but are systematically on the low end of
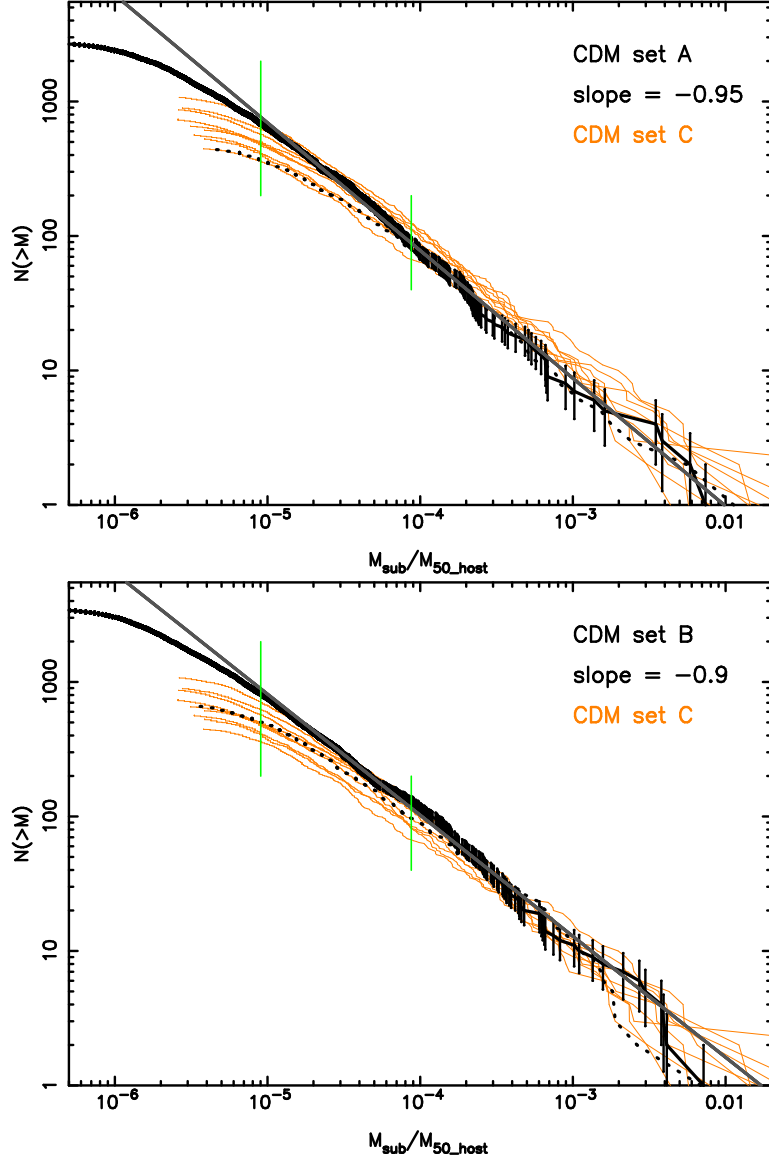
Figure 3.5: Cumulative mass functions for subhalos within R_{50} for the CDM *set A* (top) and *set B* (bottom) simulations. Subhalo masses have been normalized by the M_{50} mass of the host. Poisson error bars have been added to the high resolution simulations and fit with a straight line. Both high and low resolution (dotted lines) turn away from the straight fit below about 200 times the mass resolutions of the simulations (short vertical lines). Mass functions for the *set C* halos have also been added (thin lines) and show the A and B abundances are within the halo to halo scatter.

their distribution. This is likely due to the different cosmology used in the Ishiyama et al. simulation (discussed below).

Figure 3.7 also plots the cumulative velocity functions but includes all subhalos within R_{50} and the subhalo velocities have been normalized by the circular velocity at R_{50} of their host MW. The Ishiyama et al. halos are again plotted as in Figure 3.6 as well as Via Lactea II. The solid straight line is the result from the Aquarius simulations (Springel et al. 2008). Again there is good agreement between my simulations and Via Lactea II but the simulations of Ishiyama et al. and Aquarius are offset. To first order, the abundance of halos of any size depends on the power spectrum of density perturbations which depends on the normalization, σ_8, and the tilt of the power spectrum, n_s. Larger values of either parameter increases the power on small scales and leads to a larger number of satellites for a given mass and v_{max} of the host. The values ($\sigma_8 = 0.9$, $n_s = 1$) were used in the Aquarius simulations and (0.8, 1) were used by Ishiyama et al. Both are significantly greater than the values adopted here (0.74, 0.951), and this is the likely cause of the abundance offset.

I adopted a WMAP3 cosmology to facilitate comparison to the Via Lactea II simulation. The WMAP3 values of n_s, σ_8, and Ω_m are 1.0, 2.9, and 2.5 standard deviations below the WMAP7 values (Jarosik et al. 2010). The Bolshoi simulation used parameters in agreement with WMAP7 and constraints from other cosmology projects. A comparison of the subhalo abundances of 4960 Bolshoi halos with circular velocities and masses comparable to the Via Lactea II halo indicated Bolshoi has more subhalos by about 10%. Although Via Lactea II is just one halo and may not be representative of the average for a WMAP3 cosmology, this agrees with
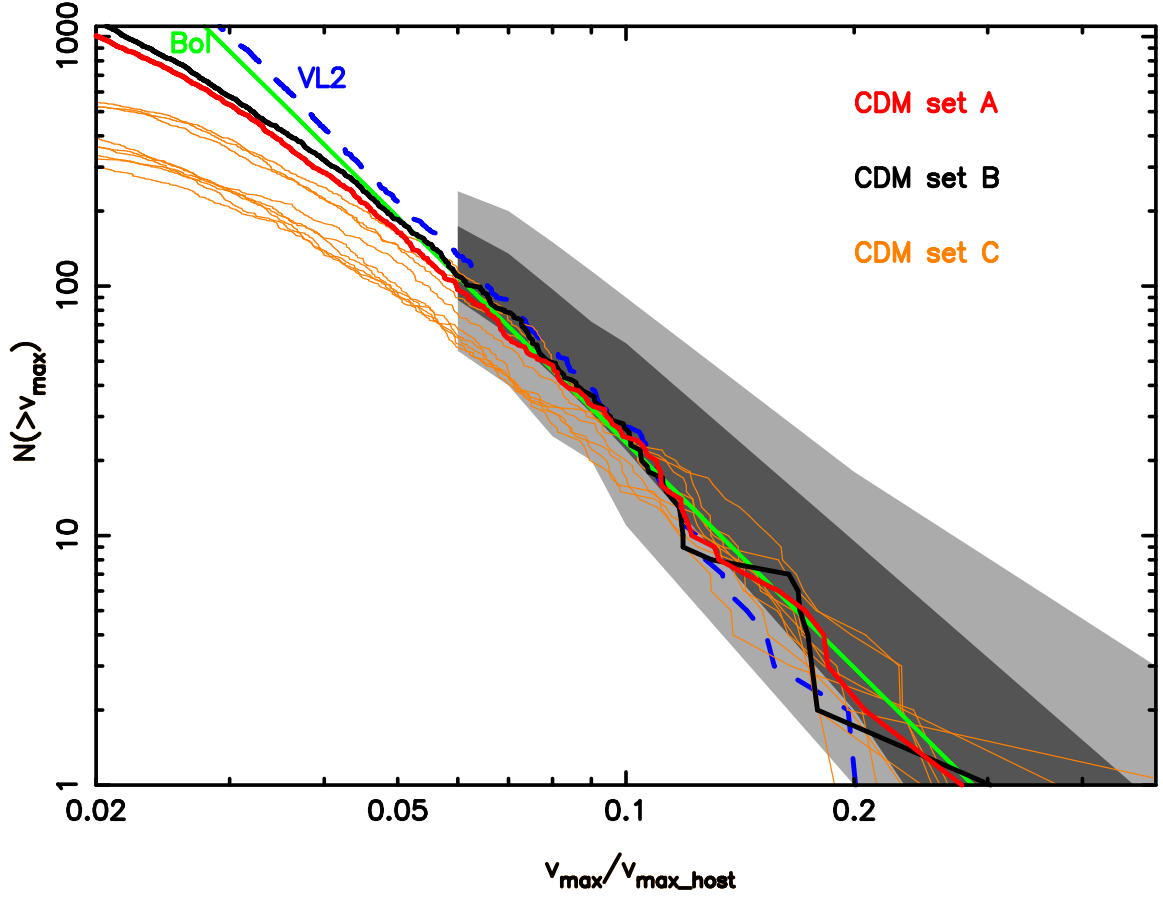
Figure 3.6: Cumulative velocity functions for subhalos within R_{100} in the low resolution *set C* (thin lines) and high resolution *set A* and *set B* (thick lines) MW halos. Subhalo circular velocities have been normalized to the maximum circular velocity of the host halo. The dashed line is the subhalo velocity function of Via Lactea II, the straight solid line is the fitting formula from the Bolshoi simulation applied to the A and B halos. The shaded regions show the minimum and maximum and $\pm 1\sigma$ from the mean of the 68 MW-sized halos of Ishiyama et al. (2009).
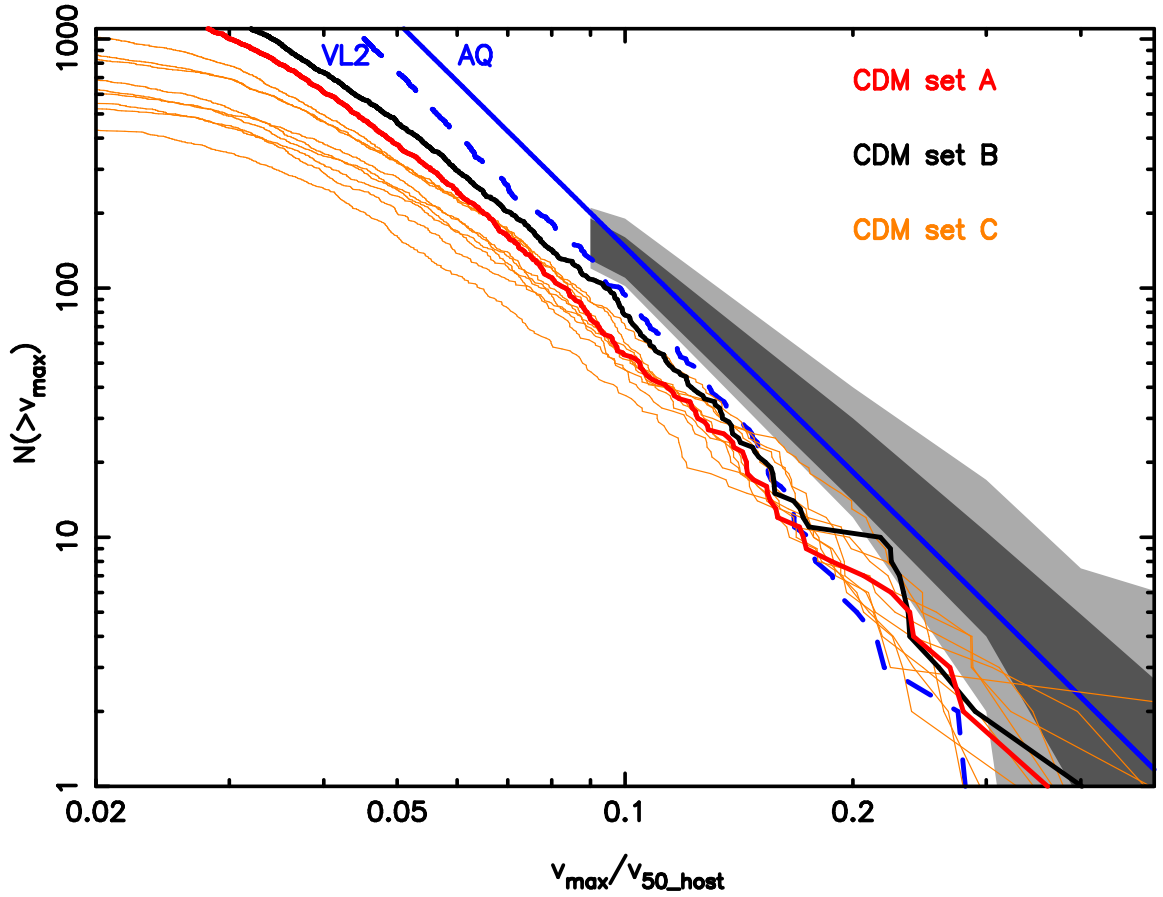
Figure 3.7: Cumulative velocity functions for subhalos within R_{50} in the low resolution *set C* (thin lines) and high resolution *set A* and *set B* (thick lines) simulations. Subhalo circular velocities have been normalized to the circular velocity of the host halo at a radius enclosing an overdensity of $\Delta = 50$. The dashed line is the velocity function for Via Lactea II and the straight solid line is the average abundance from the Aquarius simulations (Springel et al. 2008). The shaded region is the minimum/maximum range and $\pm 1\sigma$ about the mean for halos from the simulations of Ishiyama et al. (2009).

expectations from the 10% smaller value of σ_8 used by Via Lactea II. I used the same value of σ_8 as Via Lactea II but the Bolshoi fitting formula applied to my high resolution simulations in Figure 3.6 provides an excellent fit with no indication of an offset. This could be because, as shown in the Appendix, the BBKS power spectrum used in my high resolution simulations has about 10% more power at sub-Galactic scales. Below I argue that an intrinsic scatter in subhalo abundance of 30% (1σ) is reasonable to adopt and conclude this can account for variations in the adopted cosmology without the need for a separate correction.

From my simulations and those of Ishiyama et al. in Figures 3.6 and 3.7 it is clear that the subhalo abundances of halos of similar sizes have a scatter. For a given cosmology the scatter in abundance includes an intrinsic scatter and a statistical scatter from the number of subhalos. The Aquarius simulation suite included 6 MW-sized halos simulated at very high resolution. For subhalos within R_{50}, at high values of the abundances where the statistical scatter is small, the 1σ intrinsic scatter was determined to be 10%. In Figure 3.7 the scatter in the Ishiyama et al. abundances decreases for increasing N and appears to be converging to the 10% found in Aquarius. However the variation in the Ishiyama et al. abundances in Figure 3.6 is clearly converging to a larger value. As argued in Ishiyama et al. (2009), the smaller scatter in Figure 3.7 can be explained by the inclusion of subhalos at distances up to R_{50} which are outside the virial radius and, hence, their evolution has not been affected by the structure of the host halo. Using v_{50} to normalize the subhalo velocities can also reduce scatter since, unlike v_{max}, it is less dependent on the central concentration. I will be interested in the number of subhalos in the inner

regions of the host MW which are expected to be sensitive to the host concentration so I adopt the higher value for the intrinsic variation in the number of subhalo from Figure 3.6 which is estimated to be about 30% (1σ) after subtracting the Poissonian statistical scatter expected from the number of subhalos.

In Figure 3.8 the cumulative circular velocity functions for subhalos within R_{100} for the high resolution *set A* and *set B* CDM and WDM simulations are plotted. The *set A* abundances have been increased 7% to normalize the CDM abundances to those of the *set B* simulation and illustrate that the relative suppression of subhalo abundances for each WDM simulation compared to CDM is the same across both simulation sets. The straight line is the Bolshoi fitting function applied to the *set B* CDM halo. The vertical lines in Figure 3.8 show where $v_{max} = 6$ and 8 km/s. Below 8 km/s the high resolution CDM simulations begin to fall away from the Bolshoi line due to the resolution limits of the simulations. For $v_{max} > 8$ km/s my simulations are reasonably complete within R_{100} of each Milky Way although numerical destruction of a small fraction of satellites in the inner Milky Way would not be apparent in Figure 3.8, especially for the CDM and 4 keV cosmologies. Before comparing the simulations to observations the convergence distance of the simulations needs to be determined.

3.3.2 Convergence Study

Satellites orbiting in the halo of a larger galaxy are destroyed by tidal stripping and heating through encounters with other satellites. Satellites in simulations are
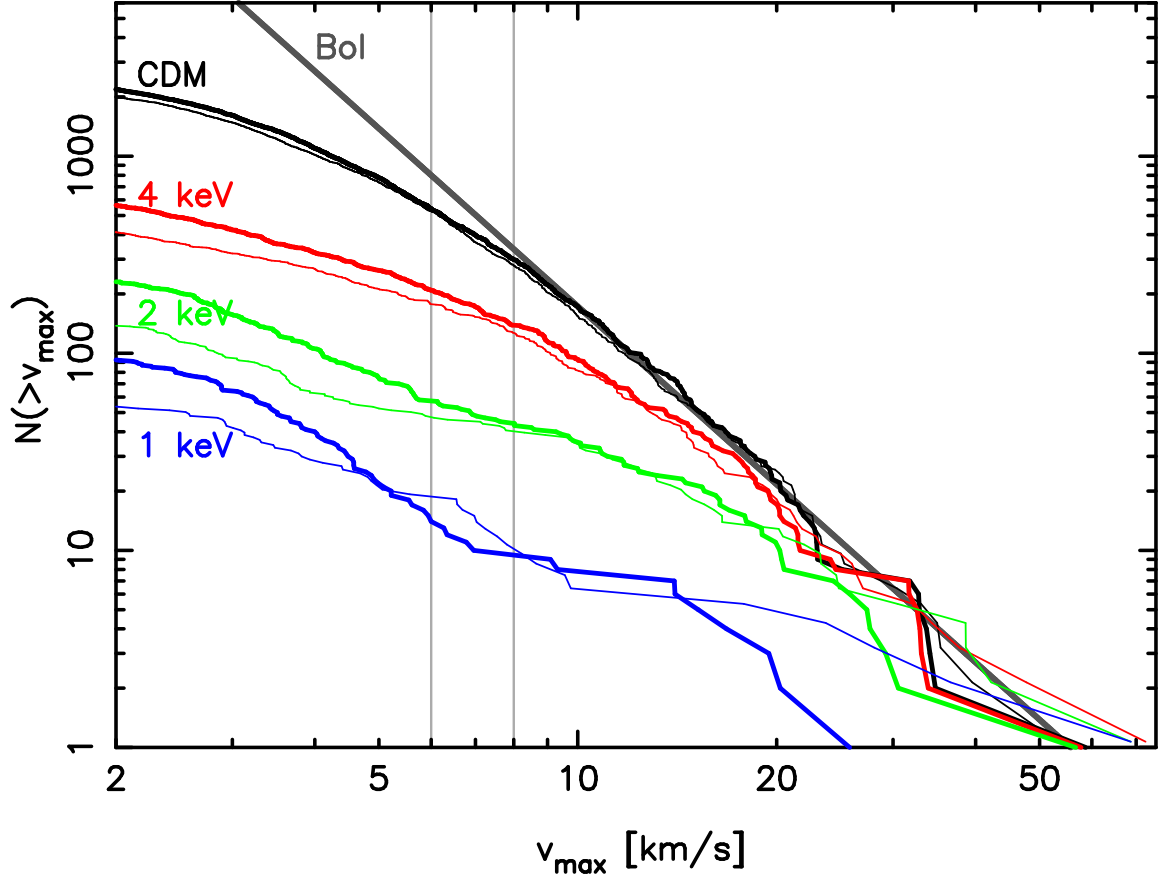
Figure 3.8: Cumulative velocity functions for satellites in the high resolution *set A* and *set B* CDM and WDM simulations. The *set A* abundances (thin lines) have been increased by 7% to normalize the CDM abundances to those of the *set B* and show that the relative suppression of halos in WDM cosmologies compared to CDM is similar across both simulations. The straight gray line is the Bolshoi fitting formula applied to the *set B* halo.

also destroyed artificially by numerical effects that become dominant for poorly resolved halos in the inner halo region. There will therefore be a radius inside of which the simulations will not converge to a realistic representation of the actual Milky Way.

To determine the convergence of the simulations and have an idea of the variance of the results, simulations at lower and higher resolution of two different realizations of a Milky Way-sized galaxy were performed. Convergence studies were conducted following the argument elucidated below, in combination with results of published high resolution simulations found in the literature. Using the work of Moore et al. (1999a); Klypin et al. (1999); De Lucia et al. (2004); Ishiyama et al. (2009), it is assumed that the shape of the cumulative satellite velocity function for host halos of different masses is nearly constant and the total number of satellites scales linearly with the host mass. If the simulations are convergent, the cumulative circular velocity function for satellites, $N(R)$, within a given Galactocentric radius, R, should be proportional to the enclosed mass, $M(R)$, and a function of R that represents the fraction of satellites that survive destruction from physical effects:

$$N(R) \equiv f(R)M(R), \tag{3.11}$$

where $f(R) \propto R^\alpha$. The normalization of $f(R)$ can be set using values of $N(R)$ and $M(R)$ at a distance R_0:

$$N(R) \left(\frac{R_0}{R}\right)^\alpha \left(\frac{M_0}{M(R)}\right) = N_0 = const. \tag{3.12}$$

The velocity functions normalized in this way will be constant with radius where the simulations are convergent. Where numerical effects destroy satellites the velocity

functions will normalize to a lower value. The parameter α is expected to be constant because there is no characteristic scale for the destruction rate in dark matter only simulations. Hence, α can be determined at large radii where convergence is certain.

Figure 3.9 shows the normalized velocity functions for the simulations. The normalization constants M_0, R_0 have been chosen at 200 kpc and the value of α (0.55) was adjusted by hand until a good fit was achieved for the *set B* velocity functions above 200 kpc in the high resolution CDM cosmology at circular velocities > 6 km/s (vertical lines). This α also provides a good fit for the WDM cosmologies and for the *set A* simulations, although the 1 and 2 keV velocity functions have a wider scatter due to the smaller numbers of satellites in these simulations. The $m_{WDM} = 4$ keV simulation is convergent for $v_{max} > 6$ km/s to distances > 100 kpc. At 75 kpc the effects of numerical resolution are apparent. The same value of α has been used in the normalization of the low resolution sets and appears to provide a good fit for the velocity functions $> 200 - 250$ kpc. The effects of numerical resolution on the destruction of satellites are apparent at larger distances in these simulations: < 200 kpc for CDM and < 150 kpc for WDM.

The 1 and 2 keV WDM velocity functions in Figures 3.8 and 3.9 show a flattening when going from high to low velocities until about 6 km/s, below which the number of subhalos increases greatly. This is a generic feature of WDM simulations (Bode et al. 2001; Barkana et al. 2001) and is usually explained as top-down fragmentation of matter filaments. Given that WDM simulations are known to form nonphysical halos along filaments (Melott 2007; Wang and White 2007), it is likely the low velocity upturn in the velocity function of subhalos is actually caused by
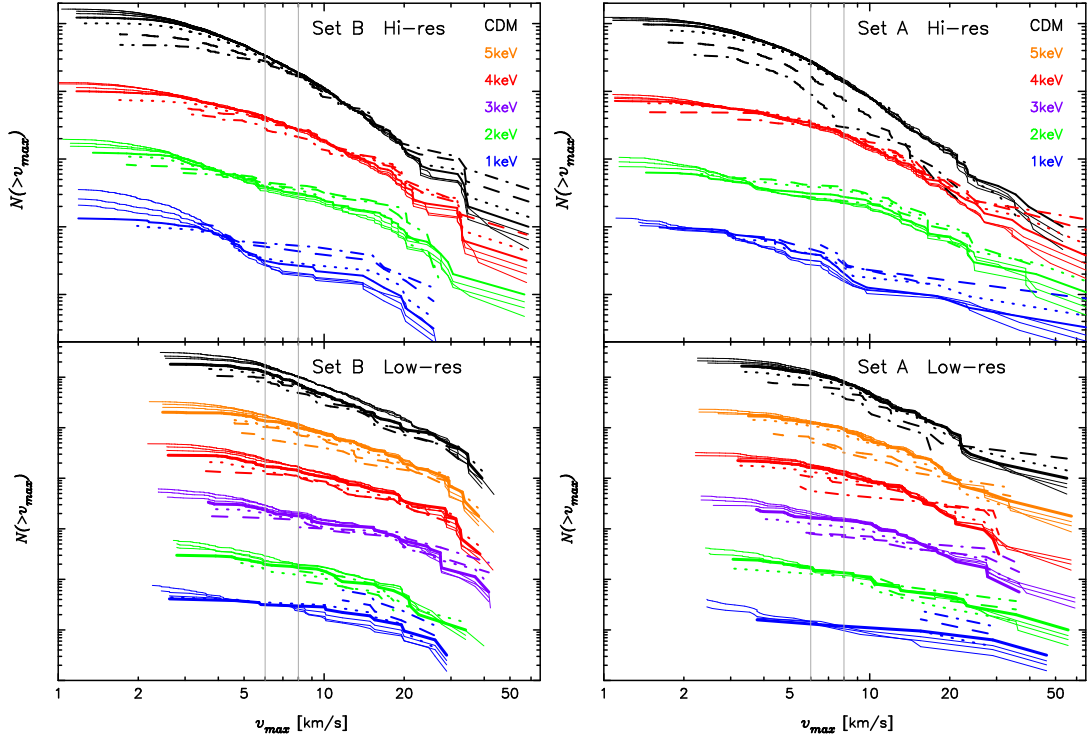
Figure 3.9: *(left)* Velocity functions for *set B* high *(top)* and low *(bottom)* resolution simulations normalized with Eq. (3.12). Solid lines are $R = 400$, 300, 250, and 200 kpc (thick), dotted line is $R = 150$ kpc, dashed line is $R = 100$ kpc, dot-dashed line is $R = 75$ kpc. The WDM cosmologies have been shifted down vertically for clarity. The value $\alpha = 0.55$ was set by the high resolution simulation and provides good normalization for the low resolution as well but the effects of incompleteness become apparent at much larger radii ($150 - 200$ kpc compared to $75 - 100$ kpc for high resolution). *(right)* Same as the left panel, but for the *set A* high *(top)* and low *(bottom)* resolution simulations. The value $\alpha = 0.55$ also provides good normalization for this set of halos.

these numerical artifacts accreting onto the MW. Since these nonphysical halos form with separations typical of the mean particle distances in the initial conditions, the number of halos should increase with the mass resolution of the simulation. The low resolution simulations do not show clear evidence of upturns in the velocity functions, simulations with resolution higher than the high resolution sets would be required to confirm this effect. Regardless, only satellites with velocities greater than 6 km/s in the high resolution simulations will be considered when deriving constraints on the dark matter particle mass.

3.3.3 Comparison to Observations

Before the Sloan Digital Sky Survey there were only 12 classically known satellite galaxies to the Milky Way. Sixteen new satellites have been discovered in the SDSS. All known Milky Way satellites are listed in Table 3.2 where the given satellite distances are used as their Galactocentric distances. Before comparing the observed satellites to the simulations it is important to recognize the limitations of the SDSS that affect the observed satellite abundances. The primary limitation is the sky coverage of the survey, 28.3% for Data Release 7 (11663 deg^2). Second, being a magnitude limited survey, the SDSS has a luminosity bias. The detection efficiency of dwarfs in the SDSS is a function of dwarf size, luminosity, distance, and Galactic latitude as shown by Walsh et al. (2009). An approximate expression is given in Tollerud et al. (2008) (using the work of Koposov et al. (2008)) for the distance which galaxies of luminosity $> L$ are completely detected: $d \approx 66$ kpc

$(L/1000~L_\odot)^{1/2}$. Galaxies with $L > 10^4$ $L_\odot$ should be approximately complete to 200 kpc, with $L > 2300$ $L_\odot$ to 100 kpc. The distance range $100 - 200$ kpc is thus suited for comparisons because the simulations are convergent and the observations are nearly, but not quite, complete. For the subsequent analysis only satellites with distances < 200 kpc are used.

I account for the partial sky coverage of the SDSS by correcting the simulated satellite abundances to the survey area with a series of random trials, described in more detail later in this section. My observed data set consists of the SDSS discovered dwarfs combined with the classic Milky Way satellites within the SDSS footprint; Ursa Minor, Draco, Sextans, and Leo I and II. A conservative luminosity correction for the SDSS dwarfs is considered using the formulas in Walsh et al. (2009). This adds only two satellites at distances $150 - 200$ kpc and does not affect the conclusions, therefore I do not consider luminosity corrections when comparing the observations and simulations. It is important to note the formulas in Walsh et al. (2009) assume the size-luminosity distribution of known dwarfs is representative of all satellites. There may be a population of dwarfs with surface brightnesses below the detection limit of the SDSS (Ricotti and Gnedin 2005b; Ricotti et al. 2008b; Ricotti 2010; Bovill and Ricotti 2009b).

Table 3.2: Summary of known Milky Way satellites.

Name	$dist$ [kpc]	σ_{star} [km/s]	M_V	References
Classical (pre-SDSS)				
Sagittar	24 ± 2	11.4 ± 0.7	-13.4	a
LMC	49 ± 2	...	-18.4	a
SMC	58 ± 2	...	-17.0	a
Ursa Minor	66 ± 3	9.3 ± 1.8	-8.9	a
Draco	79 ± 4	9.5 ± 1.6	-8.8	a
Sculptor	79 ± 4	6.6 ± 0.7	-11.1	a
Sextans	86 ± 4	6.6 ± 0.7	-9.5	a
Carina	94 ± 5	6.8 ± 1.6	-9.3	a
Fornax	138 ± 8	10.5 ± 1.5	-13.2	a
Leo II	205 ± 12	6.7 ± 1.1	-9.6	a
Leo I	270 ± 30	8.8 ± 0.9	-11.9	a
Phoenix	405 ± 15	...	-10.1	a
SDSS discovered				
Segue I	23 ± 2	4.3 ± 1.2	-1.5	b
Ursa Major II	30 ± 5	6.7 ± 1.4	-3.8	c, d
Segue II	~ 35	3.4 ± 2.0	-2.5	e
Willman I	38 ± 7	$4.3^{+2.3}_{-1.3}$	-2.5	f, c
Coma Berenics	44 ± 4	4.6 ± 0.8	-3.7	h, d
Bootes II	60 ± 10	...	-3.1	i
Bootes I	62 ± 3	$6.5^{+2.0}_{-1.4}$	-5.8	c
Pisces I	80 ± 14	...	...	j, k
Ursa Major I	106^{+9}_{-8}	7.6 ± 1.0	-5.6	d
Hercules	140^{+13}_{-12}	5.1 ± 0.9	-6.0	h, d
Canes Venatici II	150^{+15}_{-14}	4.6 ± 1.0	-4.8	h, d
Leo IV	160^{+15}_{-14}	3.3 ± 1.7	-5.8	h, d
Leo V	175 ± 9	2.4 ± 1.8	-5.2	l, m
Pisces II	~ 180	...	-5.0	n
Canes Venatici I	220^{+25}_{-16}	7.6 ± 0.4	-7.9	o, d
Leo T	~ 420	7.5 ± 1.6	-7.1	p, d

References: (a) Mateo (1998), (b) Geha et al. (2009), (c) Martin et al. (2007), (d) Simon and Geha (2007), (e) Belokurov et al. (2009), (f) Willman et al. (2005), (g) Martin et al. (2007), (h) Belokurov et al. (2007), (i) Walsh et al. (2007), (j) Watkins et al. (2009), (k) Kollmeier et al. (2009), (l) de Jong et al. (2009), (m) Belokurov et al. (2008), (n) Belokurov et al. (2010), (o) Zucker et al. (2006), (p) Irwin et al. (2007)

Willman 1 is an exceptional case in that it may not be a dark matter dominated dwarf galaxy but a globular cluster undergoing tidal disruption. Its stellar velocity dispersion implies a large mass to light ratio like other dwarf spheroidals and it has a size and luminosity intermediate between MW dwarfs and globular clusters (Willman et al. 2005), but unresolved binaries and tidal heating may contaminate the velocity dispersion and lead to an overestimated mass. Although it has a large metallicity spread unlike the stellar population of a globular cluster (Martin et al. 2007), follow-up spectroscopy (Siegel et al. 2008) suggests there may be contamination by foreground stars and when these are excluded the metallicity spread can be consistent with a metal-poor globular cluster. When deriving constraints on the dark matter particle mass I will consider both including and excluding Willman 1 as a Milky Way satellite.

When comparing observations and simulations I apply cuts to the simulated subhalos and consider only those with velocities above 6 and 8 km/s. As discussed in the previous section this is to avoid potential contamination from numerical effects in the WDM simulations. That these velocity cuts are a reasonable estimate of the minimum v_{max} of the dark matter halos the observed galaxies are presumably embedded in can be shown as follows. Ricotti and Gnedin (2005b) found in simulations that the maximum circular velocities of satellites are at least twice the velocity dispersion of the stellar component. Assuming the stellar velocity dispersions of the observed dwarfs are $\sqrt{3}$ times the line-of-sight velocity dispersions (σ_{star} in Table 3.2), then all dwarfs with measured velocity dispersions have maximum circular velocities greater than 8 km/s. Assuming dwarfs without measured velocity

dispersions are similar to the other known dwarfs it is conservative to conclude all dwarfs reside in dark matter halos with v_{max} greater than 8 km/s. An alternative approach is the work of Wolf et al. (2010) relating the circular velocity at half light radius to the velocity dispersion: $v_c(r_{1/2}) = \sqrt{3}\sigma_{star}$. All the observed dwarfs except Leo V have circular velocities at half light radius about 6 km/s or greater. Since the maximum circular velocity must be greater than or equal to the half light circular velocity, it is also reasonable to consider that all observed dwarfs reside in halos with $v_{max} > 6$ km/s. It should be stressed that these cuts reflect the need to reduce the numerical effects of the nonphysical halos in WDM simulations that dominate the high resolution simulations at subhalo velocities below 6 km/s rather than an assumption on the relationship between luminous satellites and dark matter halos.

To correct the simulations to the partial sky coverage of the SDSS I first calculate the coordinates of all simulated satellites in a spherical coordinate system centered on the Milky Way halo. I run a series of 10,000 trials with a field of view (FOV) center randomly chosen on the sky and calculate the number of subhalos within a solid angle corresponding to the total sky coverage of the SDSS (11663 deg^2). I apply circular velocity and distance cuts to the subhalos and calculate the median number of subhalos in the FOV and the 1σ and 2σ ranges from the trials. Figures 3.10 and 3.11 show probability distributions of the number of subhalos in the sky footprints in each cosmology of the *set A* and *set B* simulations for subhalos with $v_{max} > 6$ km/s and distances $100 - 200$ kpc. The missing satellites problem is dramatically illustrated by the CDM simulations which have $\sim 40 - 80$ satellites in this distance range yet only 7 are observed in the SDSS. Satellite abundances are

reduced in the WDM simulations with the 2 keV cosmologies in 2σ agreement with the observations.

I further compare my simulations to the observations in Figure 3.12 where I plot the number of satellites within 200 kpc in bins of 50 kpc for the observed data set and both sets of simulation data with $v_{max} > 6$ km/s. The observed number of satellites are plotted with wide black bars and upward arrows indicating these are only lower limits due to the surface brightness limits of the SDSS; it is possible there are more dwarfs yet to be discovered. Willman 1 has not been included as a MW satellite in this figure. The median number of satellites in each simulation set are plotted as short lines enclosed in shaded dark and light rectangles that give the 1σ and 2σ ranges, respectively. The 6 km/s cut to the simulation data assures the high resolution simulations are convergent to at least $r = 100$ kpc. Focusing on the $100 - 200$ kpc bins it is clear the 1 keV simulations have far too few satellites to match the observations. The 2 keV *set B* simulation is consistent with the observations in all bins but *set A* is only consistent in the $100 - 150$ kpc bin. The 4 keV simulations can be consistent with the observations although they may require galaxy formation to be suppressed in some of the dark matter halos. Strong conclusions cannot be drawn from this plot because it is not clear how variance in the abundances and numerical destruction in the inner bins for the simulated satellites may affect the results.

The number of satellites in the simulations can be corrected for the effects of numerical destruction using the convergence equation, Eq. (3.12). The mass and number of satellites inside R_{50} were used for the normalization and the number

57
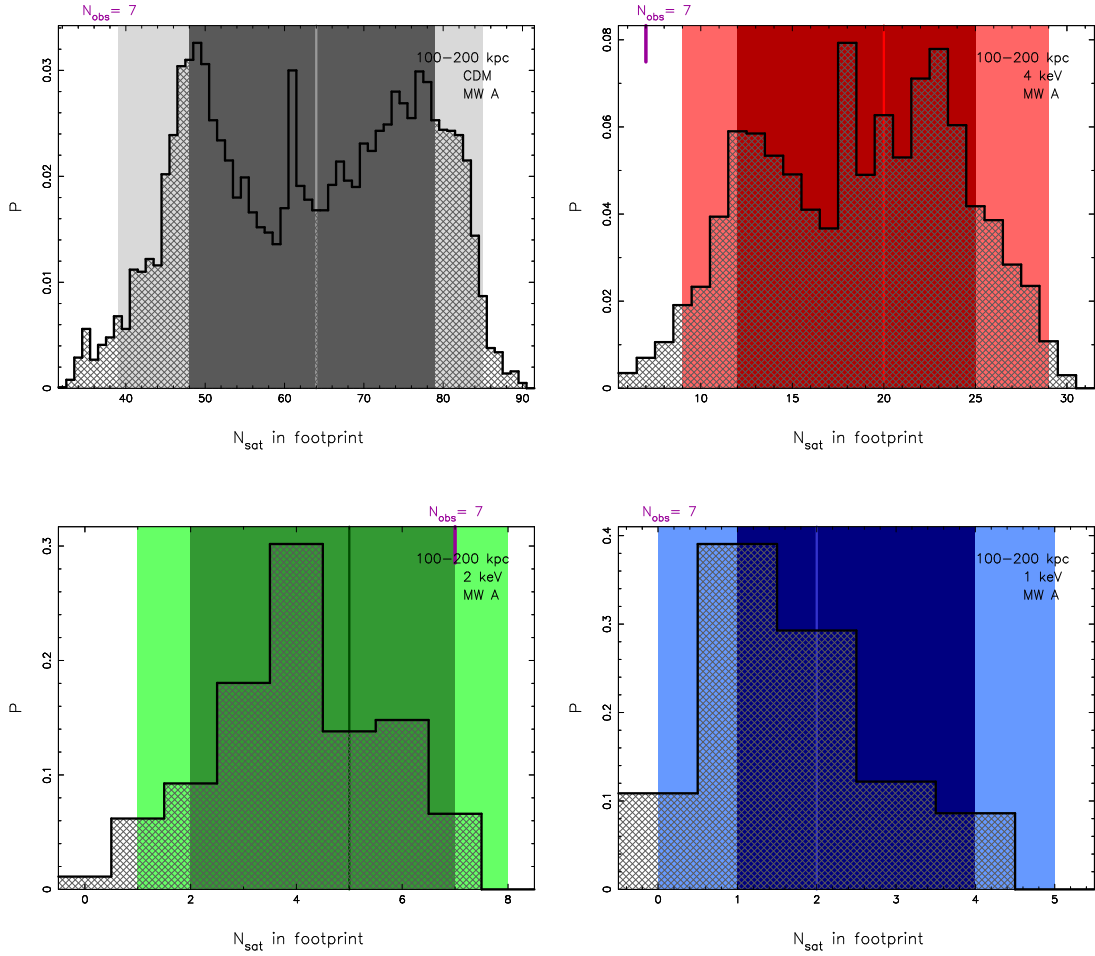
Figure 3.10: Number of subhalos in the *set A* simulations within a field of view (FOV) equivalent to the sky coverage of the SDSS. 10,000 trials were run for each cosmology with the FOV center chosen randomly. The probability distributions for the number of subhalos are plotted by the hatched histograms. The long vertical lines shows the median of the distributions while dark and light shaded bans show the 1σ and 2σ ranges, respectively. The simulated satellites have been cut by $v_{max} > 6$ km/s and by distance from $100 - 200$ kpc. The number of satellites observed in the SDSS in this distance range is given at the top of each plot and plotted with a short vertical line where appropriate.
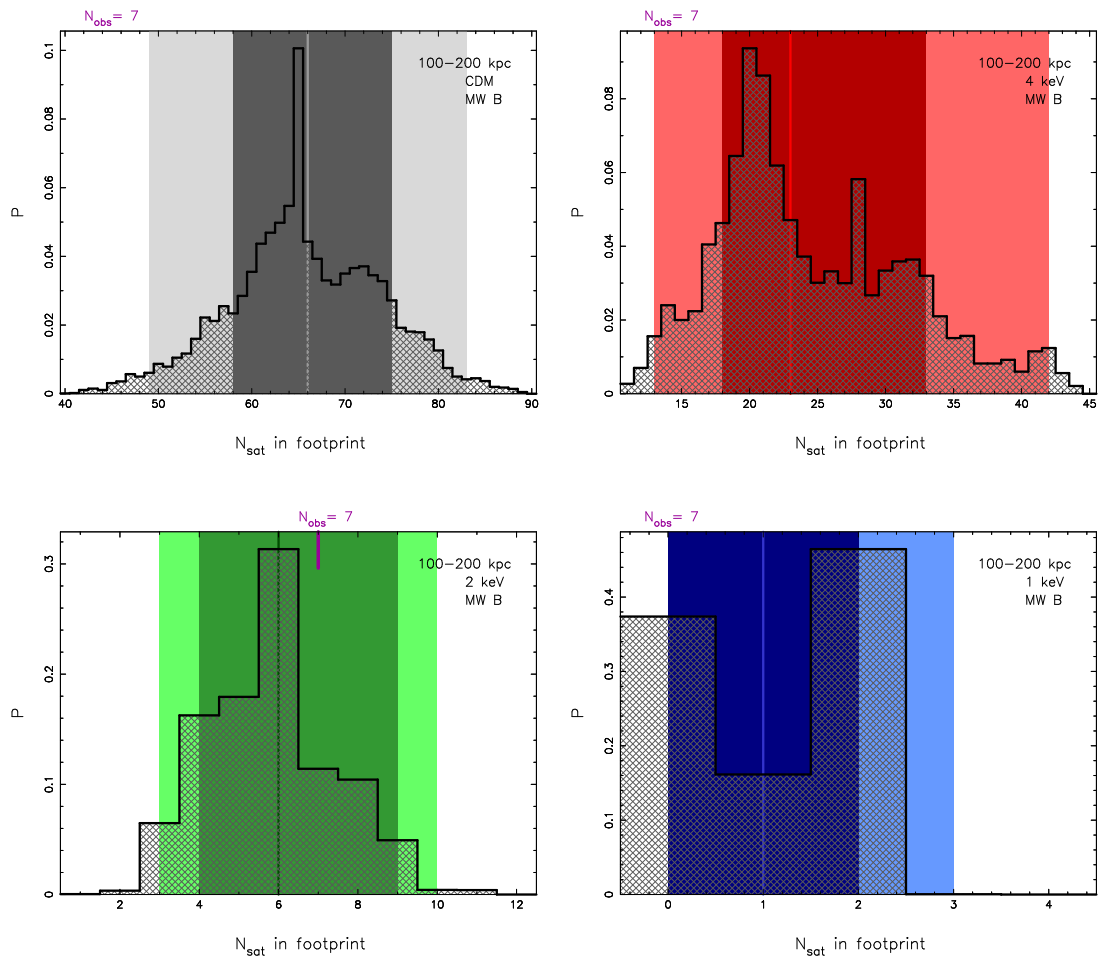
Figure 3.11: Same as Figure 3.10 but for the *set B* simulations.
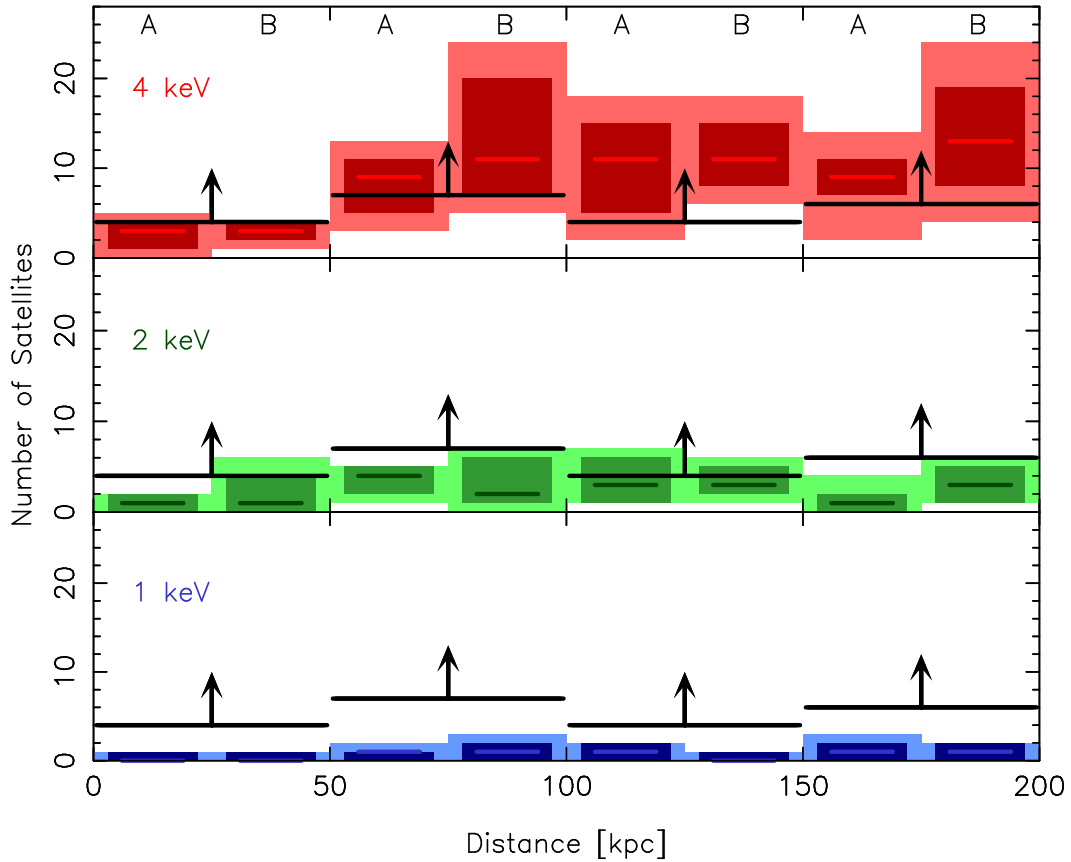
Figure 3.12: The number of satellites in 50 kpc distance bins from the Milky Way center. The satellites in simulations have been cut by $v_{max} > 6$ km/s. The median number of satellites within the equivalent sky footprint of the SDSS and 1σ and 2σ ranges are plotted as the colored rectangles in each bin for both the *set A* and *set B* simulations. The wide black bars with arrows are the observed satellites within the footprint of the SDSS but do not include Willman 1. The observations are incomplete at distances greater than about $50 - 100$ kpc (depending on the luminosity and surface brightness of the dwarfs), while simulations have not converged for less than about 100 kpc. The 1 keV cosmologies are inconsistent with the observed satellite abundances.

of satellites in 50 kpc bins for the simulations were calculated. The $0 - 50$ kpc bin is most important for constraining the dark matter particle mass because the observations are most complete in this bin.

Plotted in Figure 3.13 are the differences in the number of observed and simulated satellites within 50 kpc of the MW center for the *set B* simulations as a function of the dark matter particle mass with interpolation between the simulated data. The variance in simulated subhalo abundances are calculated for a 30% intrinsic rms scatter plus a Poissonian variance in the number of subhalos and corrected to the partial sky coverage of the SDSS assuming an isotropic distribution on the sky. The dark and light shaded regions in the plot show the 1σ and 2σ ranges, respectively. The number of satellites in simulation must be at least equal to the number of observed satellites, therefore where this quantity equals zero defines a lower limit on the dark matter particle mass. The arrowed lines indicate the lower limits at 1σ and 2σ for this case of the *set B* simulations with a 6 km/s cut to the subhalos and excluding Willman 1 from the observed set.

The same analysis was repeated using a $v_{max} > 8$ km/s cut to the simulation data. The effects when Willman 1 was included in the observed data set were also considered for both the 6 km/s and 8 km/s analysis. The results are presented in Table 3.3. The *set B* halo is slightly more abundant in subhalos but both the *set A* and *B* simulations give the same results to within about 10%. Rather than take the average of the two simulations, the more conservative of the two constraints is adopted.

In the most conservative case, where Willman 1 is not a dark matter dominated
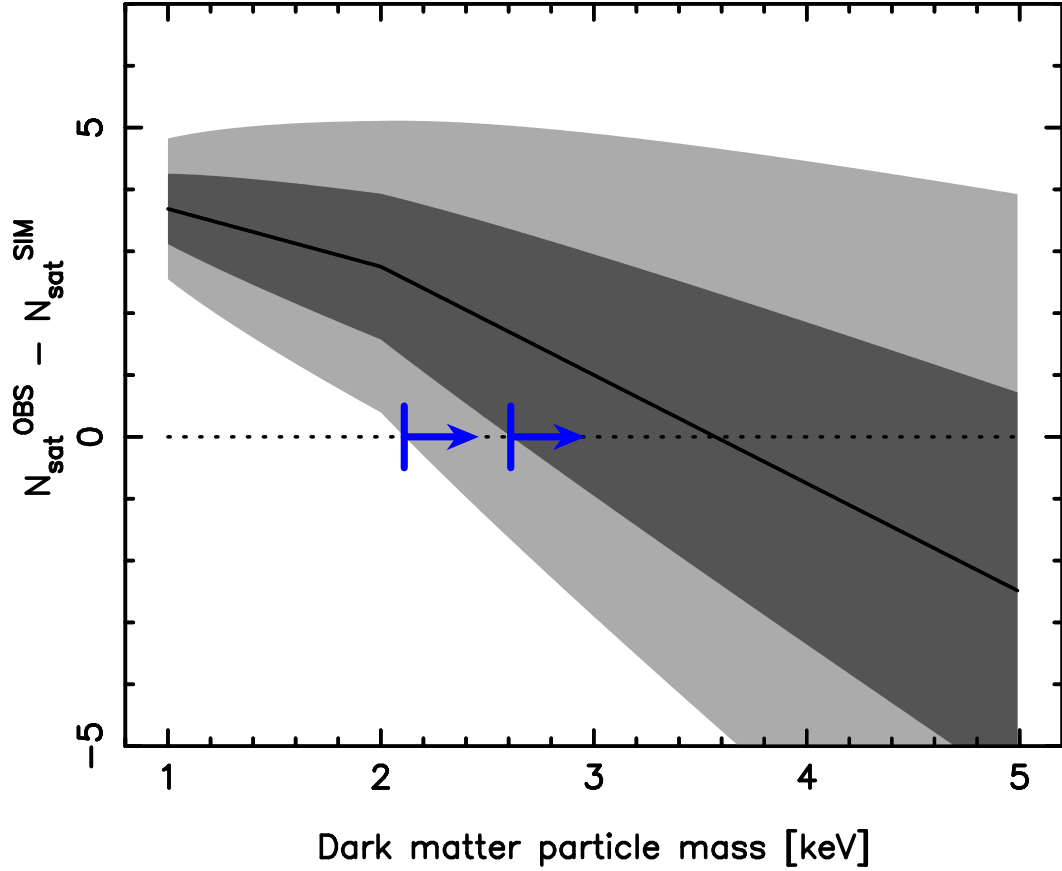
Figure 3.13: The number of satellites within 50 kpc observed in the SDSS sky footprint, excluding Willman 1, minus the number of satellites in simulation with 1σ and 2σ limits (dark and light shaded regions). The number of satellites from 0-50 kpc was calculated from the convergence equation in the *set B* high resolution simulation for $v_{max} > 6$ km/s and corrected to the partial sky coverage of the observations assuming an isotropic distribution on the sky. Where the difference in the number of observed and simulated satellites equals zero sets a lower limit on the dark matter particle mass and is given by the arrows.

Table 3.3: Dark matter particle mass constraints (in keV) from the high resolution *set A* and *B* MW halos. Constraints for simulated subhalo v_{max} cuts of 8 and 6 km/s and including or excluding Willman 1 from the observed data set are given.

	$v_{max} > 8$ km/s				$v_{max} > 6$ km/s			
Will 1?	Included		Excluded		Included		Excluded	
MW	A	B	A	B	A	B	A	B
2σ	> 3.2	> 2.9	> 2.7	> 2.5	> 2.7	> 2.4	> 2.3	> 2.1
1σ	> 4.4	> 4.0	> 3.6	> 3.3	> 3.4	> 3.0	> 2.9	> 2.6

dwarf galaxy and all observed satellites correspond to dark matter halos with $v_{max} > 6$ km/s, a formal limit of $m_{WDM} > 2.1$ keV can be adopted with 95% confidence.

3.4 Discussion

I found that a model with $m_{WDM} \sim 4$ keV produces the best fit to observations at < 50 kpc, i.e. this model has a number of dark matter satellites equal to the number of observed luminous satellites. However, due to the large uncertainties in the number of observed satellites due to partial sky coverage and on the number of simulated satellites due to Poisson and intrinsic scatter, that partially reflects observational uncertainties on the mass and v_{max} of the Milky Way, I find much weaker lower limits on m_{WDM} than 4 keV. In the future however, the lower limit on m_{WDM} will improve as observations of MW satellites become more complete. The scatter of the simulation can also be reduced using constrained simulations of the Local Group (also including the effect of baryons) in combination with more accurate determination of the mass, rotation curve, and concentration of the Milky Way.

Considering the various uncertainties in the number of observed and simulated satellites, I found a conservative lower limit of $m_{WDM} > 2.1$ keV (2σ) on the dark matter particle mass. I also found the 1 keV WDM simulations have too few satellites to match the Milky Way observations. This agrees with the semianalytic modeling and Milky Way satellite luminosity functions in WDM cosmologies work of Maccio' and Fontanot (2009); however, I only apply a cut to the simulated halos to avoid numerical effects and do not make assumptions on how the dark matter halos are populated by luminous galaxies. Lovell et al. (2013) performed a study similar to mine, simulating one of the Aquarius Milky Ways in several WDM cosmologies, and favor a similar but slightly warmer limit of 1.6 keV. Horiuchi et al. (2013) have examined the abundances of dwarf spheroidal galaxies around M31. The advantage in this approach is our external viewpoint gives a volume-complete census of dwarfs around M31 without needing a sky coverage correction as for the MW, although the census in only complete to higher luminosities. These authors derived a similar limit of $m_{WDM} > 1.8$ keV. Schultz et al. (2014) studied using high redshift galaxy counts as a means to constrain WDM and conclude masses < 1.3 keV are inconsistent with galaxy counts in the Hubble Ultra Deep Field at $> 2.2\sigma$. They also find these models are inconsistent with optical depths to the CMB due to Thomson scattering observed by the *Planck* observatory, but with weaker confidence.

My result can also be compared to limits on the particle mass from the Lyman-α forest in high redshift quasars. Lyman-α absorption by neutral hydrogen along the line of sight to distant quasars over redshifts 2–6 probes the matter power spectrum in the mildly nonlinear regime on scales 1–80 Mpc/h. Viel et al. (Viel

et al. 2005, 2006, 2008) have numerically modeled the Lyman-α forest flux power spectra for varied cosmological parameters and compared to observed quasar forests to obtain lower limits on the dark matter particle mass. Their 2006 work (Viel et al. 2006) used low resolution spectra for 3035 quasars ($2.2 < z < 4.2$) from the SDSS (McDonald et al. 2006) and found a 2σ lower limit of 2 keV for a thermal WDM particle. This limit agrees with my results that a 2.1 keV particle is the lower limit that can reproduce the observed number of Milky Way satellites and approximately agrees with the Lyman-α work of Seljak et al. (2006) who find a 2σ limit > 2.5 keV for a thermal particle. Viel et al. (2008) use high resolution spectra for 55 quasars ($2.0 < z < 6.4$) from the Keck HIRES spectrograph in addition to the SDSS quasars. With the new data they report a lower limit of 4 keV (2σ). A caveat arises in Viel et al. (2009), who show the flux power spectrum from the SDSS data prefer larger values of the intergalactic medium (IGM) temperature at mean density than expected from photoionization. The flux power spectrum temperature is also higher than that derived from an analysis of the flux probability distribution function of 18 high resolution spectra from the Very Large Telescope and also higher than constraints from the widths of thermally broadened absorption lines (Ricotti et al. 2000; Schaye et al. 2000). This could be explained by an unaccounted for systematic error in the SDSS flux power spectrum data which may also affect the derived dark matter particle mass limits. The most recent 2σ lower limit from Ly-α is 3.3 keV (Viel et al. 2013).

Using the scaling relation for sterile neutrinos I find a lower limit $m_s >$ 11.8 keV with 95% confidence for a DW produced sterile neutrino particle. Scaling

to the other production mechanisms gives $m_s > 7.9$ keV for the SF mechanism and $m_s > 2.6$ keV for Higgs decay sterile neutrinos; however, it must be noted this is not based on transfer function calculations for the SF and Higgs mechanisms but assumes a simple scaling for the average momentum for the different production mechanisms (Kusenko 2009). The image fluxes in gravitationally lensed quasars have been shown to require sterile neutrino masses greater than a few keV (Miranda and Macciò 2007). The Lyman-α forest observations discussed above in the context of a thermal particle also set limits on the sterile neutrino mass. The 2006 work of Viel et al. sets $m_s > 11$ keV and is similar to the Seljak et al. (2006) limit $m_s > 14$ keV. The 2008 work of Viel et al. sets the highest limit of $m_s > 28$ keV but is subject to the caveats mentioned above. The limit for the most recent 2013 work is $m_s > 21$ keV (Viel et al. 2013).

Sterile neutrinos are expected to radiatively decay to a lighter mass neutrino and a X-ray photon with energy $E_\gamma = m_s/2$. X-ray observations of the diffuse X-ray background (Boyarsky et al. 2006b) and dark matter halos in clusters (Abazajian and Koushiappas 2006; Boyarsky et al. 2006a; Riemer-Sorensen et al. 2007; Boyarsky et al. 2008), M31 (Watson et al. 2006, 2012), dwarf spheroidal galaxies (Boyarsky et al. 2007; Riemer-Sørensen and Hansen 2009; Boyarsky et al. 2009; Loewenstein et al. 2009), and the halo of the Milky Way (Riemer-Sørensen et al. 2006; Abazajian et al. 2007; Boyarsky et al. 2007) have all been used to set constraints on the sterile neutrino mass. Observations of the diffuse X-ray background have set $m_s < 9.3$ keV (Boyarsky et al. 2006b), while the Virgo and Coma clusters have been used to set $m_s < 6.3$ keV (Abazajian and Koushiappas 2006) which also agrees

with limits from the Bullet cluster, 1E 0657-56, $m_s < 6.3$ keV (Boyarsky et al. 2008) and is close to results from the Milky Way halo $m_s < 5.7$ keV (Abazajian et al. 2007). Tighter constraints have been determined from the dwarf spheroidal Ursa Minor $m_s < 2.5$ keV (Loewenstein et al. 2009) and from M31 observations $m_s < 2.2$ keV (Watson et al. 2012).

These upper limits are well below the lower limits derived in this work and from Lyman-α observations and seem to rule out the DW and SF production mechanisms. However, all of these mass limits, including the constraints set in this work, are model dependent and make certain assumptions. In general X-ray constraints depend on the sterile neutrino mass, the mixing angle with active neutrinos θ, and the cosmic matter density of sterile neutrinos Ω_s. There are also assumptions about the initial conditions, that there were no sterile neutrinos in the early Universe at temperatures > 1 GeV, there was no entropy dilution after creation, and no coupling to other particles. There are also uncertainties with the calculation of production rates because these occur at temperatures where the plasma is neither well described by hadronic nor quark models (Asaka et al. 2006; Boyarsky et al. 2006b). Depending on the assumptions made and the adopted production model the relationship between m_s, θ, and Ω_s changes so that robust constraints cannot be placed on any one model parameter. However, Horiuchi et al. (2013) show the combined limits in parameter space rule out that all of the dark matter is DW produced sterile neutrinos although a mix of resonant and non-resonant production mechanisms is allowed. This possibility corresponds to a mixed dark matter cosmology with the non-resonant produced neutrinos being the warm component and the resonant the

cold component. There have also been reports of a detection of a dark matter X-ray emission line in the spectrum of galaxy clusters consistent with $m_s = 7.1 \pm 0.7$ keV (Bulbul et al. 2014; Boyarsky et al. 2014). This detection is provisional but if confirmed the limits derived in this work imply the sterile neutrinos are not produced by the DW mechanism or do not constitute the entirety of the dark matter. Abazajian (2014) calculated the transfer function for sterile neutrinos produced by the SF mechanism consistent with the X-ray line and showed it matches that of a thermal particle of mass 2.02 keV. As I have shown, this would be consistent with MW satellite abundances and solve the missing satellites problem.

3.5   Summary

I conducted N-body simulations of the formation of MW-sized dark matter halos in CDM and WDM cosmologies. Such simulations are complicated by the formation of artifical small mass halos due to the discreteness of the initial conditions but with sufficient resolution they are only important at small scales and can be avoided with an appropriate circular velocity cut.

I studied the number of satellite halos as a function of distance from the MW. The 4 keV and 2 keV WDM simulations can adequately reproduce the observed number of satellites at distances up to hundreds of kiloparsecs while the 1 keV simulation is severely deficient. The high resolution simulations followed the formation of two MW-sized halos. Numerical simulations of MW-sized halos show significant variance in the number of satellites, an effect that can be easily quantified using

published studies and was incorporated in my results. I calculated the number of satellites in the inner 50 kpc, corrected for the effects of numerical destruction, and accounted for the variance by conservatively adopting a 30% (1σ) intrinsic scatter in the number of satellites in addition to a scatter from Poisson statistics. I corrected the number of satellites in simulation to the survey area of the SDSS and derived a very conservative lower limit on the dark matter particle mass of > 2.1 keV (95% C.L.). This agrees with the earlier Lyman-α forest modeling work of Viel et al. (2006) that $m_{WDM} > 2$ keV but is below their latest limit of $m_{WDM} > 3.3$ keV (Viel et al. 2013). However, the two methods are independent and almost certainly are subject to different systematic errors, if any exist.

My lower limit of 2.1 keV for a thermal dark matter particle scales to lower limits of 11.8, 7.9, 2.6 keV (95% C.L.) for DW, SF, and Higgs decay produced sterile neutrinos. Sterile neutrinos, if they exist, are expected to decay into X-rays and active neutrinos. Observations of the unresolved cosmic X-ray background and X-ray observations of dark matter halos on scales from dwarf galaxies to clusters set upper limits below my lower limit and the limits of Lyman-α forest modeling. These limits are derived under many assumptions and, in general, the constraints apply to a parameter space of m_s, θ, and Ω_s.

My constraint is a conservative lower limit since I only correct the satellite abundances in simulation to the number of SDSS dwarfs by accounting for the partial sky coverage of the survey. An analysis that takes into account the surface brightness limits of the observational data may allow tighter constraints; however, the analysis would be somewhat model dependent. I have also not included the

effects on subhalos of baryonic structures in the inner MW halo such as a disk. The presence of a disk could lead to greater subhalo destruction due to increased dynamical friction and tidal heating. By increasing the subhalo destruction rate in the inner halo, disks would increase the lower bounds on the dark matter particle mass. The assumption of no disk is a conservative one and an analysis that includes a disk may allow tighter constraints.

I have demonstrated how N-body simulations of the MW and its satellites can set limits on the dark matter particle mass comparable to, and independent of, complementary methods such as modeling the Lyman-α forest. These limits are helped greatly by the discovery of many new MW satellites in the SDSS. There may still be a population of low luminosity, low surface brightness dwarf galaxies undetectable by the SDSS (Ricotti and Gnedin 2005b; Ricotti et al. 2008b; Ricotti 2010; Bovill and Ricotti 2009b). Future surveys with instruments like the Large Synoptic Survey Telescope have the potential to discover many more MW satellites and further improve constraints on the mass of the dark matter particle. Better constraints will result from the smaller uncertainty in the number of observed satellites achieved by improving the sky coverage and reducing luminosity corrections. In addition, the existence of a yet unknown population of even fainter satellites is not unlikely.

Chapter 4:   Dependence of Satellite Densities on Cosmology

4.1   Overview

The satellite galaxies of the Milky Way, being the closest extragalactic objects and indeed within the virial radius of the Milky Way's extended halo of dark matter, are uniquely suited for testing theories of galaxy formation and evolution and the nature of dark matter. The MW satellites known before the SDSS numbered too few to account for predictions from N-body simulations in ΛCDM cosmologies that were otherwise successful in describing the abundances of galaxies in clusters and the large scale features of the matter distribution (Klypin et al. 1999; Moore et al. 1999a). The discovery of a population of fainter satellites in the SDSS and more sophisticated simulations that account for supernova feedback and the heating of the IGM during reionization have alleviated this problem by predicting a strong suppression of galaxy formation in low mass halos (Bullock et al. 2000; Ricotti et al. 2002b,a, 2008a).

Recent work focusing on the brightest MW satellites has highlighted dynamical discrepancies with high-resolution CDM simulations. Boylan-Kolchin et al. (2011, 2012a) compared the most luminous satellites to subhalos in the Aquarius simulation suite of six Milky Way-sized halos. Abundance matching models set a

one-to-one correspondence between luminosity and dynamical mass and place the brightest satellites in the largest subhalos. However, the observed stellar velocities cannot be reconciled with the velocity profiles of the largest dark matter subhalos in simulation. The most massive satellites, either at the present epoch, the epoch of reionization, or over the complete infall history, are too dense to be dynamically consistent with the Milky Way satellites. Observations of the stellar velocity dispersions in the bright satellites are consistent with dark matter halos with maximum circular velocities < 25 km s^{-1} while the Aquarius Milky Ways have about 10 subhalos each with $v_{max} > 25$ km s^{-1} that are also not Magellanic Cloud analogs. Several solutions to this problem have been proposed. Galaxy formation may be stochastic on dwarf spheroidal scales and the bright satellites do not reside in the largest subhalos (Boylan-Kolchin et al. 2011; Katz and Ricotti 2012). This requires abandoning the monotonic relation between galaxy luminosity and halo mass that is well-established for brighter galaxies.

Interestingly, models in which some of the ultra-faint dwarfs are fossils of the first galaxies (Ricotti and Gnedin 2005a; Bovill and Ricotti 2009a) show some tension with observations only at the bright end of the satellite luminosity function (Bovill and Ricotti 2011a,b). Simulations that produce a large population of ultra-faint dwarfs also produce an overabundance of bright dwarf satellites especially in the outer parts of the Milky Way. However, this tension is eased by the expected stripping of the extended primordial stellar population around bright satellites.

The number of satellites of all size are known to be proportional to the mass of the host halo (Klypin et al. 1999). Wang et al. (2012) argue the low velocities

of the MW satellites may be an indication the MW is less massive than typically thought. They show there is only a 5% probability for a galaxy of mass $2 \times 10^{12} M_{\odot}$ to have 3 satellites or less with maximum circular velocities > 30 km s^{-1} but 40% for a galaxy of mass $10^{12} M_{\odot}$. A low mass for the Milky Way of $8 \times 10^{11} M_{\odot}$ is also favored in the work of Vera-Ciro et al. (2013). Direct measures of the MW mass typically focus on stellar tracers of the inner halo or radial velocity measurements of the MW satellites and give a range of virial mass $0.8 - 2.5 \times 10^{12} M_{\odot}$, the reader is referred to the references in Boylan-Kolchin et al. (2012b) where observations of the spatial motion of Leo I are used to constrain the mass of the Milky Way to $> 10^{12} M_{\odot}$ at 95% confidence.

Sawala et al. (2012) show the simulations can be reconciled with the observations by including baryonic physics in the simulations. Inclusion of baryonic physics removes gas from halos through supernova expulsion of the interstellar medium, prevention of gas accretion through reionization heating of the IGM, and ram pressure stripping from satellites. Removal of baryons from the dark matter halos also reduces the potential well resulting in less accretion of both gas and dark matter. They show dark matter only simulations overpredict the subhalo abundance by 30% at a mass scale of $10^{10} M_{\odot}$ with an increasing number of subhalos with no gas or stars below this scale.

The influence of baryons was also studied by di Cintio et al. (2011). They found that while satellites with low baryon fractions have lower concentrations than their dark matter only counterparts, satellites with high baryon fractions have higher central densities due to adiabatic contraction. Satellites with high baryon fractions

also tend to have the largest maximum circular velocities. However, their recent work (Di Cintio et al. 2013) finds the subhalo density profiles are better described by Einasto profiles than Navarro, Frenk, and White profiles (Navarro et al. 1997) and that this reconciles the observations with simulated satellites of similar luminosities. Vera-Ciro et al. (2013) also find agreement with Einasto profiles. However, while the initial work of Boylan-Kolchin et al. (2011) assumes NFW profiles their later work (Boylan-Kolchin et al. 2012a) uses the subhalo circular velocity profiles directly with no assumed form.

Another possibility is a change in the nature of the dark matter from standard CDM assumptions of collisionless particles with low intrinsic thermal velocities. Vogelsberger, Zavala, and Loeb (2012) simulated one of the Aquarius Milky Way halos in self-interacting dark matter models. The ability of the dark matter particles to self-scatter leads to the formation of subhalos with constant density cores. The lower density decreases the inner circular velocity profiles bringing the simulations into agreement with the observations.

A truncation in the dark matter power spectrum was investigated as a solution to the paucity of satellites by reducing the abundance of halos at subgalactic scales. One method for producing a truncated power spectrum is if the dark matter particles decoupled with relativistic velocities early in the radiation dominated era and thereby able to stream out of overdense regions before becoming nonrelativistic at a time before the horizon had reached Galactic scales. The scale of the power spectrum truncation in WDM is related to the mass of the dark matter particle with lighter particles decoupling earlier and able to stream longer.

Dwarf-scale halos in WDM cosmologies form later and have lower concentrations than halos in CDM, offering a potential solution to the dynamical discrepancies. Lovell et al. (2012) simulated one of the Aquarius halos in a 1 keV thermal relic WDM cosmology and showed the subhalos have central densities and velocity profiles in agreement with the bright MW satellites. In Lovell et al. (2013) their work was extended to particle masses 1.4-2.3 keV. Recently, one Milky Way-like halo was simulated in WDM at 2, 3, and 4 keV (Schneider et al. 2013). In this work I investigate the subhalo dynamics in four Milky Way-sized halos in $1, 2, 3$, and 4 keV cosmologies.

Another area potentially affecting the subhalo densities are the adopted cosmological parameters. The Via Lactea II simulation (Diemand et al. 2007, 2008), which adopted parameters from the 3rd year release of the *Wilkinson Microwave Anisotropy Probe*, was found to give similar results as the six Aquarius halos adopting WMAP1 parameters. However, reason to suspect the adopted cosmology is important comes from Macciò et al. (2008) who explored the dependence of halo concentration on the adopted cosmological model for field galaxies. They fit NFW density profiles to the halos in their simulations:

$$\rho(r) = \frac{\rho_s}{(r/r_s)(1 + r/r_s)^2},$$ (4.1)

and determined the concentrations, $c_{200} = R_{200}/r_s$, where R_{200} is the radius enclosing a density 200 times the critical density, ρ_{crit}. They found the average concentration of dwarf-scale field halos varies by a factor of 1.55 between WMAP1 and WMAP3. In this work I also examine the dependence of the CDM subhalo populations on the

adopted cosmological parameters.

4.2 Simulations

All simulations were conducted with the N-body cosmological simulation code GADGET2 (Springel 2005) with gravitational physics only and initial conditions generated with the GRAFIC2 software package (Bertschinger 2001). I use the high resolution simulations presented in Chapter 3 and Polisensky and Ricotti (2011) where two Milky Way-sized halos were simulated in a cubic box with comoving side length of 90 Mpc, mass resolution of $9.2 \times 10^4 M_\odot$, and a 275 pc gravitational softening length. I refer to these halos as the *set A* and *set B* simulations. I also ran a high resolution simulation of halo *C8* from Chapter 2 with a 138 pc softening length and refer to this as the *set C* simulations. Finally, an additional *set D* simulation was run of another Milky Way-sized halo in a 67 Mpc comoving box with a mass resolution $8.2 \times 10^4 M_\odot$ and gravitational softening length 196 pc.

Table 4.1 lists sets of cosmological parameters from measurements of the cosmic microwave background by WMAP and the *Planck* mission (Spergel et al. 2003, 2007; Komatsu et al. 2009; Larson et al. 2010; Jarosik et al. 2010; Komatsu et al. 2011; Hinshaw et al. 2012; Planck Collaboration et al. 2013). "Bolshoi" are the parameters from the Bolshoi simulation (Klypin et al. 2011) which were chosen to be within 1σ of WMAP5, WMAP7, and consistent with the results of supernovae, and X-ray cluster surveys. These parameters are within 1σ of WMAP9 except the value of n_s which is within 1.7σ. They are also within 1.2σ of Planck1 with the

exceptions of Ω_m and Ω_Λ which are 2.2σ below Planck1. The WMAP1 parameters are $2.4-4.1\sigma$ away from Planck1 while σ_8 and n_s are 3.4σ and 2.2σ above WMAP9, respectively. In contrast, the value of σ_8 in WMAP3 is 3.5σ below WMAP9 and Planck1.

Figure 4.1 shows the linear power spectra for the parameters listed in Table 4.1 normalized by the Bolshoi power spectrum. On the scale of the dwarfs ($k \sim 10$ Mpc^{-1}) the power varies greatly across cosmologies with WMAP1 and WMAP3 representing the extremes of high and low power. The Bolshoi parameters, however, represent a conservative estimate of the power on dwarf scales while being consistent with the latest CMB measurements from WMAP and *Planck*.

To investigate the dependence of satellite densities on cosmology I ran CDM simulations for each of the four sets adopting WMAP1, WMAP3, and Bolshoi parameters with the CDM transfer function from Eisenstein and Hu (1998). The box size and softening lengths were scaled in each simulation to keep the mass resolution constant. A series of low resolution tests of the *set B* halo were also run, these are described in the next section.

For my investigation of warm dark matter I used the warm dark matter transfer function given by Bode, Ostriker, and Turok (2001) valid for particles in thermal equilibrium at the time of their decoupling, such as the gravitino. I adopted Bolshoi parameters and ran simulations for particle masses of 1, 2, 3, and 4 keV for each halo. Figure 4.2 and Figure 4.3 present portraits of the Milky Way halos in the CDM and WDM simulations.

Version 1.0 of the AMIGA's Halo Finder (AHF) software (Knollmann and
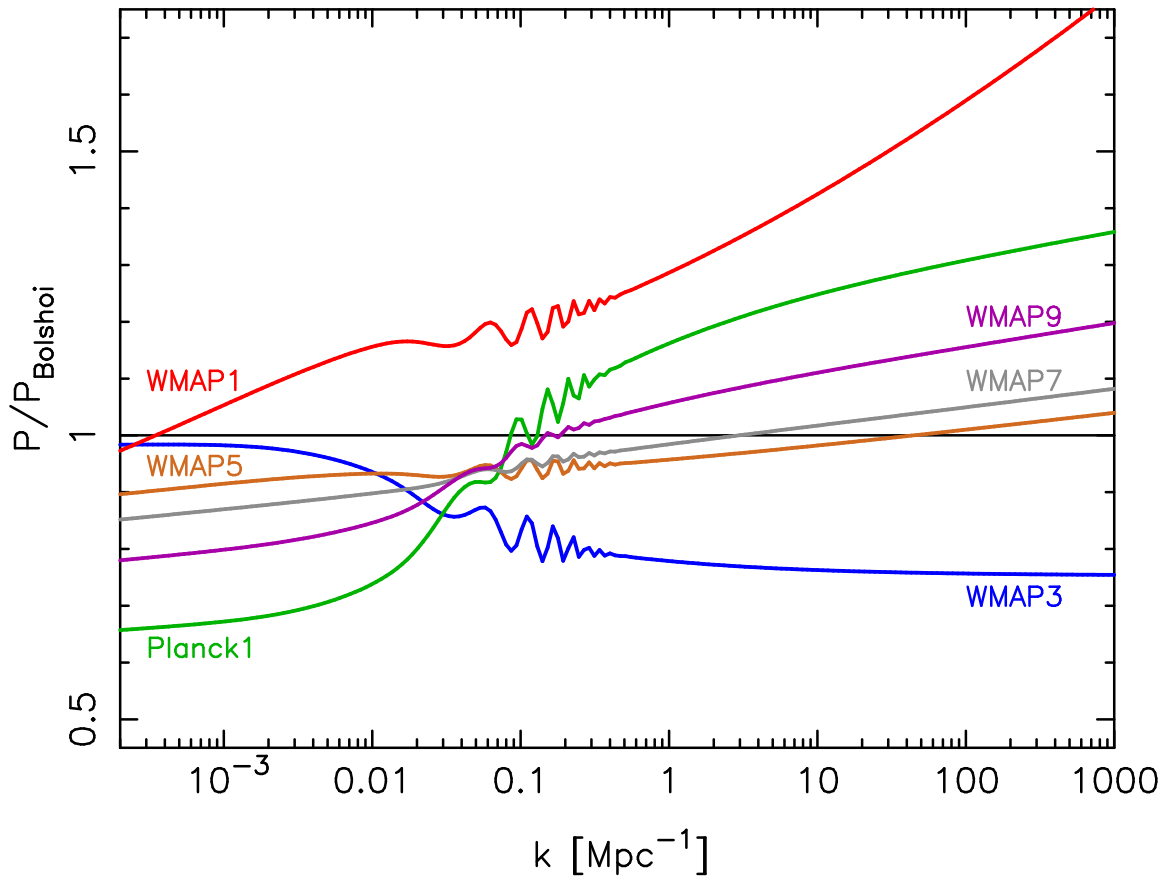
Figure 4.1: Power spectra for CDM cosmologies normalized by the Bolshoi power spectrum.
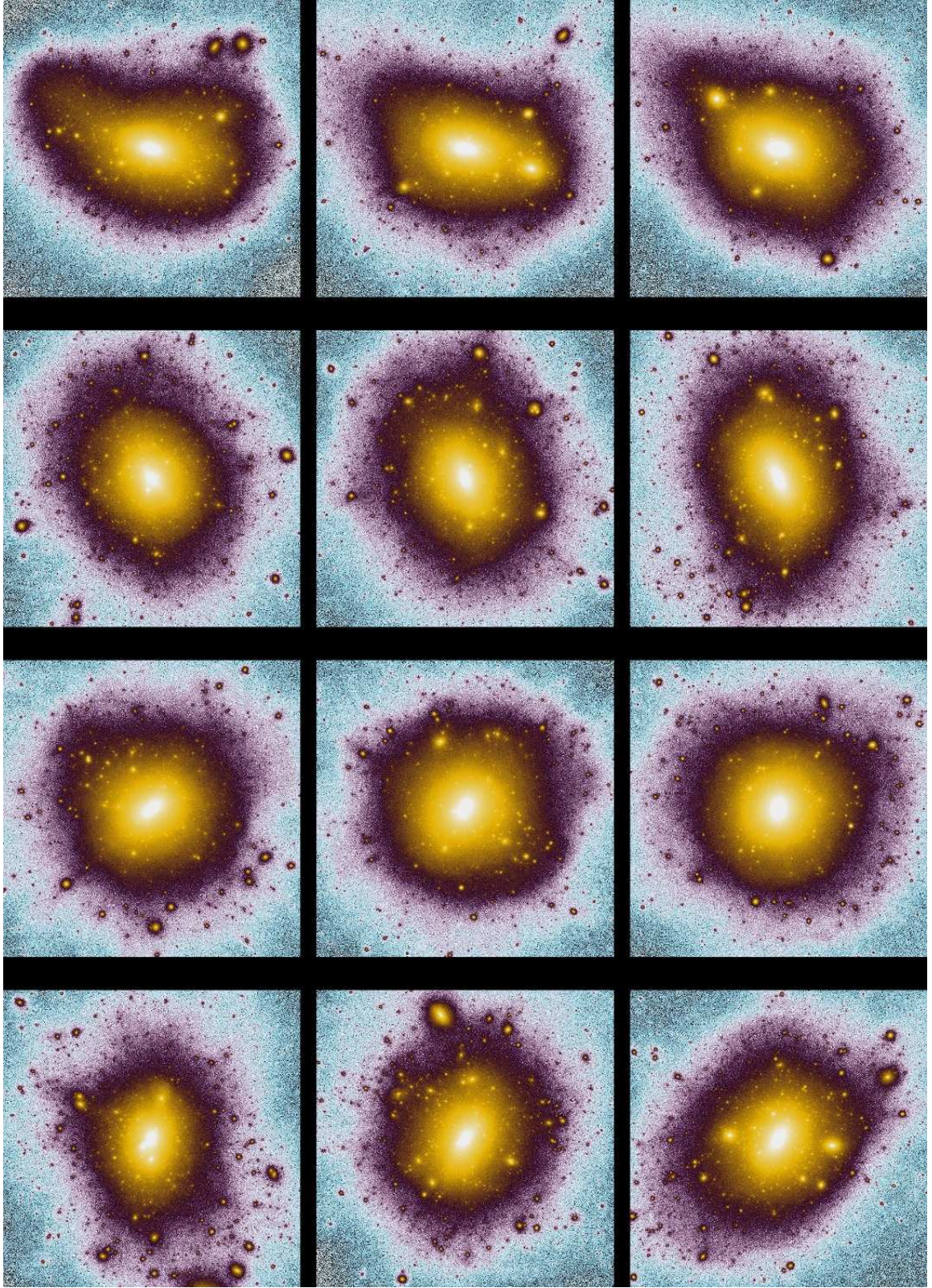
Figure 4.2: Milky Way halos in CMD simulations. From left to right: WMAP3, Bolshoi, WMAP1. From top to bottom: MW A–D.
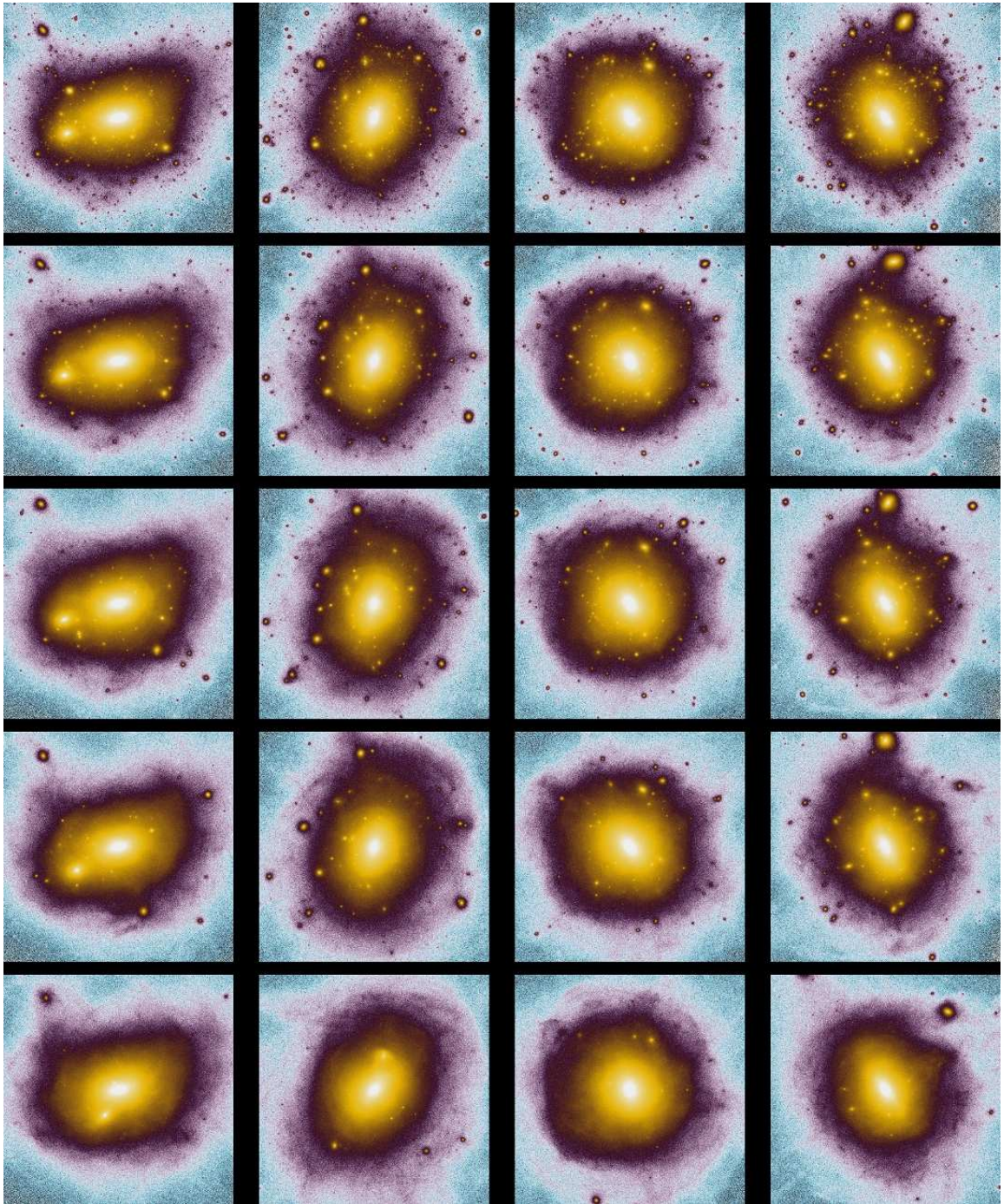
Figure 4.3: Milky Way halos in CMD and WDM simulations adopting Bolshoi parameters. From left to right: MW A–D. From top to bottom: CDM–1 keV.

Table 4.1: Cosmological parameters.

Name	Ω_m	Ω_Λ	Ω_b	h	σ_8	n_s
WMAP1	0.25	0.75	0.045	0.73	0.90	1.0
WMAP3	0.238	0.762	0.040	0.73	0.74	0.951
WMAP5	0.258	0.742	0.0441	0.72	0.796	0.963
WMAP7	0.267	0.733	0.0449	0.71	0.801	0.963
WMAP9	0.282	0.718	0.0461	0.70	0.817	0.964
Planck1	0.317	0.683	0.0486	0.67	0.834	0.962
Bolshoi	0.27	0.73	0.0469	0.70	0.82	0.95

Knebe 2009) was used to identify the Milky Way halos and their gravitationally bound subhalos after iteratively removing unbound particles. Table 4.2 summarizes the properties calculated by AHF for the simulated Milky Ways at $z = 0$. I write R_{100} to mean the radius enclosing an overdensity 100 times ρ_{crit}. The mass and number of particles inside R_{100} are M_{100} and N_{100}, respectively; $v_{max} = \max(v_{circ})$ is the maximum circular velocity of the halo occurring at a radius R_{max}, and $v_{circ}^2 = GM(< r)/r$. Also given is the NFW c_{200} concentration for each halo determined from:

$$\left(\frac{v_{max}}{v_{200}}\right)^2 = 0.2162 \ c_{200}/f(c_{200}), \tag{4.2}$$

where $f(c) = \ln(1 + c) - c/(1 + c)$.

The SUBFIND program (Springel et al. 2001) was also run on the *set B* WMAP3 data and excellent agreement was found with the results from AHF.

Table 4.2: Properties of simulations and Milky Way halos at $z = 0$.

Cosmology		m_{res} [$M_\odot$]	M_{100} [$10^{12} M_\odot$]	R_{100} [kpc]	v_{max} [km s^{-1}]	R_{max} [kpc]	N_{100}	c_{200}
Set A								
CDM	WMAP1	9.17×10^4	2.1119	324.233	214.78	39.849	$23,028,026$	9.68
CDM	Bolshoi	9.17×10^4	1.9803	326.357	198.97	55.243	$21,560,499$	8.38
CDM	WMAP3	9.17×10^4	1.8410	309.740	192.28	41.027	$20,074,556$	7.77
4 keV	Bolshoi	9.17×10^4	1.9644	325.486	198.11	50.414	$21,387,017$	8.25
3 keV	Bolshoi	9.17×10^4	1.9724	325.929	197.05	54.900	$21,474,003$	7.99
2 keV	Bolshoi	9.17×10^4	2.0061	327.771	197.54	39.871	$21,874,542$	7.96
1 keV	Bolshoi	9.17×10^4	2.0197	328.514	199.24	58.943	$22,022,816$	8.04
Set B								
CDM	WMAP1	9.17×10^4	2.0873	322.973	210.02	67.068	$22,760,127$	9.01
CDM	Bolshoi	9.17×10^4	1.9271	323.414	194.90	82.086	$21,012,806$	7.81
CDM	WMAP3	9.17×10^4	1.7540	304.781	194.62	79.767	$19,125,479$	8.29
4 keV	Bolshoi	9.17×10^4	1.9193	322.971	194.19	74.900	$20,928,496$	7.69
3 keV	Bolshoi	9.17×10^4	1.9224	323.157	193.65	77.500	$20,962,535$	7.64
2 keV	Bolshoi	9.17×10^4	1.9242	323.257	194.53	79.500	$20,981,724$	7.90
1 keV	Bolshoi	9.17×10^4	1.8804	320.771	195.23	84.286	$20,503,730$	8.06
Set C								
CDM	WMAP1	9.17×10^4	2.4195	339.274	231.42	44.932	$26,240,319$	11.13
CDM	Bolshoi	9.17×10^4	2.3259	344.343	215.81	58.943	$25,211,233$	9.05
CDM	WMAP3	9.17×10^4	1.9887	317.808	203.42	56.164	$21,645,271$	8.72
4 keV	Bolshoi	9.17×10^4	2.3195	344.029	215.03	56.900	$25,152,203$	8.95
3 keV	Bolshoi	9.17×10^4	2.3194	344.014	215.25	57.100	$25,153,016$	9.01
2 keV	Bolshoi	9.17×10^4	2.3113	343.614	214.40	61.529	$25,070,237$	8.88
1 keV	Bolshoi	9.17×10^4	2.2607	341.086	210.94	64.857	$24,563,114$	8.61
Set D								
CDM	WMAP1	8.21×10^4	1.8164	308.342	190.95	67.027	$22,135,114$	7.29
CDM	Bolshoi	8.21×10^4	1.5944	303.614	176.26	69.057	$19,429,510$	6.80
CDM	WMAP3	8.21×10^4	1.2575	272.781	164.27	50.164	$15,323,846$	6.56
4 keV	Bolshoi	8.21×10^4	1.5930	303.526	176.62	75.414	$19,412,993$	6.77
3 keV	Bolshoi	8.21×10^4	1.5875	303.171	176.38	74.143	$19,345,715$	6.78
2 keV	Bolshoi	8.21×10^4	1.5548	301.086	175.73	75.729	$18,947,343$	6.81
1 keV	Bolshoi	8.21×10^4	1.4998	297.486	171.97	79.514	$18,276,956$	6.39
Set B Low Resolution Tests								
CDM	WMAP1	7.34×10^5	2.3249	334.795	221.67	68.795	$3,168,819$	9.56
CDM sm	WMAP1	5.92×10^5	1.8899	312.452	208.53	73.630	$3,192,628$	9.92
CDM sm hi z_i	WMAP1	5.92×10^5	1.9162	313.890	212.12	66.233	$3,237,093$	10.63
CDM	Planck1	7.34×10^5	2.3463	355.582	215.70	71.209	$3,198,000$	10.02
CDM	WMAP9	7.34×10^5	2.1919	337.600	210.15	78.429	$2,987,609$	9.29
CDM	Bolshoi	7.34×10^5	2.0793	331.714	205.26	77.943	$2,834,081$	8.91
CDM	WMAP3	7.34×10^5	1.7650	305.411	191.01	98.288	$2,405,721$	7.45
CDM hi z_i	WMAP3	7.34×10^5	1.9375	315.055	198.24	82.740	$2,640,759$	7.92

Snapshots of the particle information were saved every 0.05 change in the universal scale factor, $a = (1 + z)^{-1}$, for simulations adopting Bolshoi and WMAP1 parameters. Figure 4.4 shows the mass growth of each MW halo and the VL2 halo as a function of a. The masses are normalized to the halo mass at $a = 1$. The MergerTree tool in AHF was used to construct merger trees for all identified halos. This allows determination of v_{infall} for each subhalo, the maximum value of v_{max} over a halo's formation and accretion history: $v_{infall} = \max(v_{max}(z))$. I follow the work of Boylan-Kolchin et al. (2011) and consider subhalos within 300 kpc of the Milky Way centers. I similarly identify subhalos with $v_{max} > 40$ km s^{-1} and $v_{infall} > 60$ km s^{-1} as hosts of Magellanic Cloud analogs.

I compare the simulated subhalos to the MW dwarf spheroidal satellites with luminosities $L_V > 10^5 L_\odot$. Walker et al. (2009) and Wolf et al. (2010) show line-of-sight velocity measurements provide good constraints on the dynamical masses of dispersion-supported galaxies like the MW dwarf spheroidals. The Magellanic Clouds are excluded from the observation sample as they are irregular type galaxies. The Sagitarius dwarf is also excluded because it is undergoing disruption and far from equilibrium. The observed sample consists of nine galaxies: Canes Venatici I, Carina, Draco, Fornax, Leo I, Leo II, Sculptor, Sextans, and Ursa Minor.
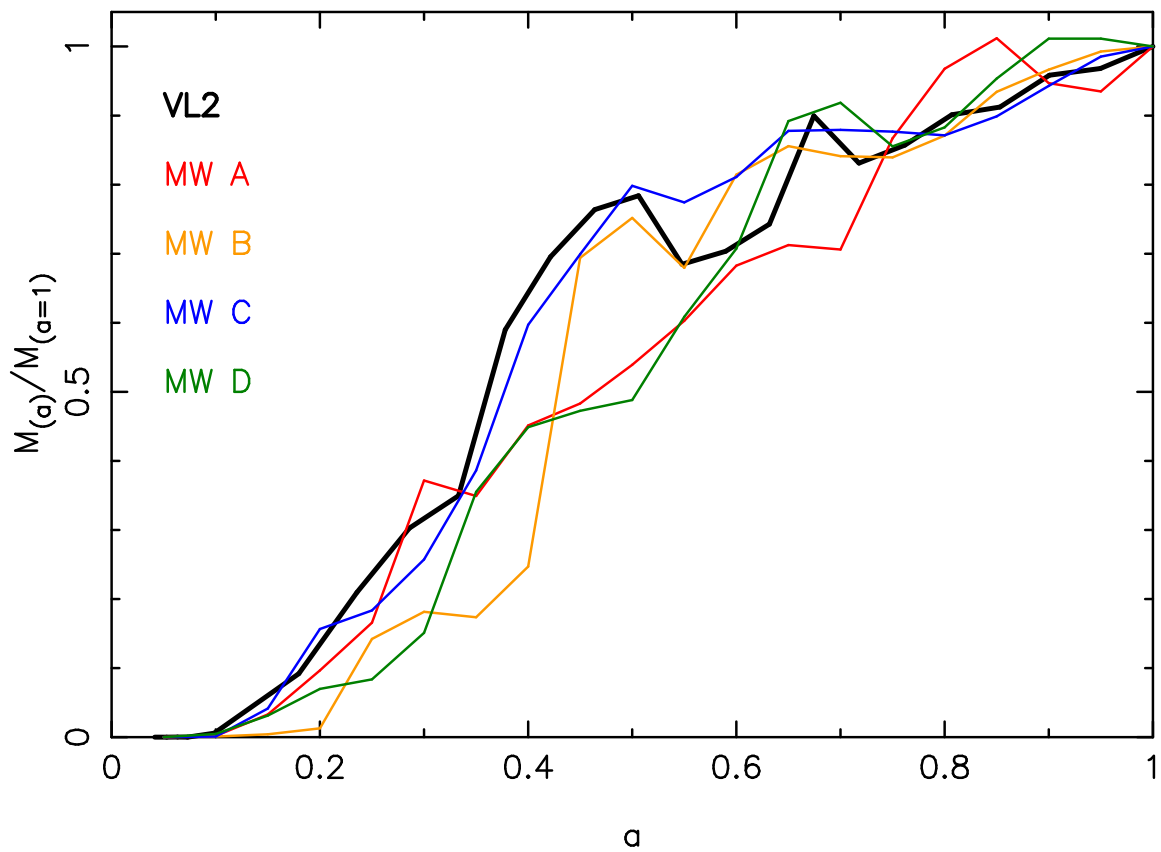
Figure 4.4: Mass growth histories of simulated Milky Way halos as a function of scale factor, a.
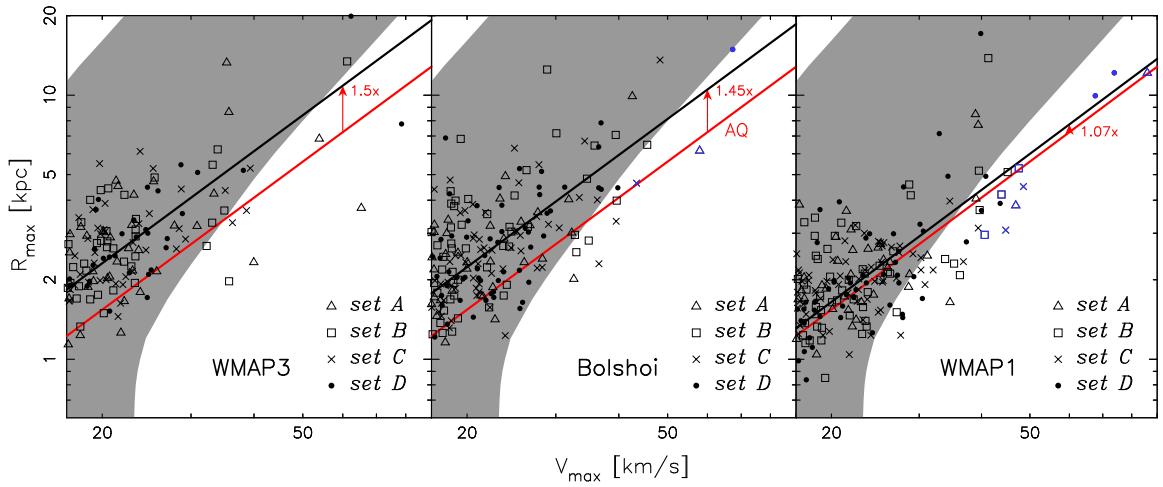
Figure 4.5: Plots of v_{max} and R_{max} for subhalos in the high resolution CDM simulations for each set of cosmological parameters. The shaded area shows the 2σ constraints for the bright Milky Way dwarfs from Boylan-Kolchin et al. (2011) assuming NFW profiles. The sloped red line shows the mean of the Aquarius subhalos. Magellanic Cloud analogs in the Bolshoi and WMAP1 simulations are plotted in blue.

4.3 Results

4.3.1 Cold Dark Matter

Figure 4.5 is a plot of v_{max} and R_{max} for subhalos in the high resolution CDM simulations. Boylan-Kolchin et al. (2011) investigated what values of v_{max} and R_{max} of NFW halos (Navarro et al. 1997) are consistent with the half-light dynamical mass constraints of the bright MW dwarf spheroidals from Wolf et al. (2010). Their 2σ confidence region is plotted as the shaded regions in Figure 4.5.

It is easy to see there are many subhalos that lie in the range consistent with the MW dwarfs, but there are some with $v_{max} > 20$ km s^{-1} that do not. These are the subhalos highlighted by Boylan-Kolchin et al. (2011) that are massive but have central densities too high to host any of the MW dwarfs. However the WMAP3 and Bolshoi simulations have only 1-3 subhalos per parent halo outside the shaded zone of Milky Way satellites compared to 4-8 subhalos for the WMAP1 simulations. This is due to R_{max} being shifted to higher values from WMAP1 for the same values of v_{max}.

Springel et al. (2008) show that the logarithms of v_{max} and R_{max} for the Aquarius subhalos have a linear relationship. I estimate the equation of their fitting line:

$$\log R_{max} = 1.41 \log(v_{max}/14.72 \text{ km s}^{-1}), \tag{4.3}$$

and plot this as the red line. I assumed a constant slope and performed least-squares fits to my subhalos in each cosmology and plot these as the black lines. The red

arrowed lines show the shift in R_{max} for each of the simulation sets compared to Aquarius. My simulations adopting WMAP1 parameters are in good agreement with the Aquarius simulations, differing by only a factor of 1.07, but in Bolshoi and WMAP3 my subhalos are offset to higher values of R_{max} by factors of 1.45 and 1.50, respectively.

I compared the fit for each simulation set separately to the corresponding fit in the WMAP1 cosmology. I found the average scale in R_{max} from WMAP1 to Bolshoi is a factor of 1.35 and a factor of 1.40 for WMAP3, with a 1σ scatter of ± 0.10 for each.

To determine if factors other than the cosmology may be affecting the subhalo densities I ran a series of tests on the *set B* halo with the mass resolution decreased a factor of 8 but the softening length kept the same as the high resolution simulations. I ran a test adopting WMAP3 parameters starting from the same initial redshift as the high resolution simulation ($z_i = 48$) and another test starting from a high redshift ($z_i = 115$), comparable to the starting redshift of Aquarius ($z_i = 127$). I also ran tests adopting the WMAP1 parameters. The Milky Way halo mass was about 30% greater in this simulation so I ran tests with the box size and mass resolution decreased to give a halo mass similar to the WMAP3 tests. I ran small box tests starting from the same low and high redshifts.

I examined applying velocity cuts of $v_{max} > 14 - 20$ km s^{-1} to the subhalos. At smaller velocities the R_{max} values for some subhalos were inside the convergence radius satisfying the criterion of Power et al. (2003) and therefore affected by the resolution of the simulations. In Figure 4.6 I normalize the values of R_{max} for all
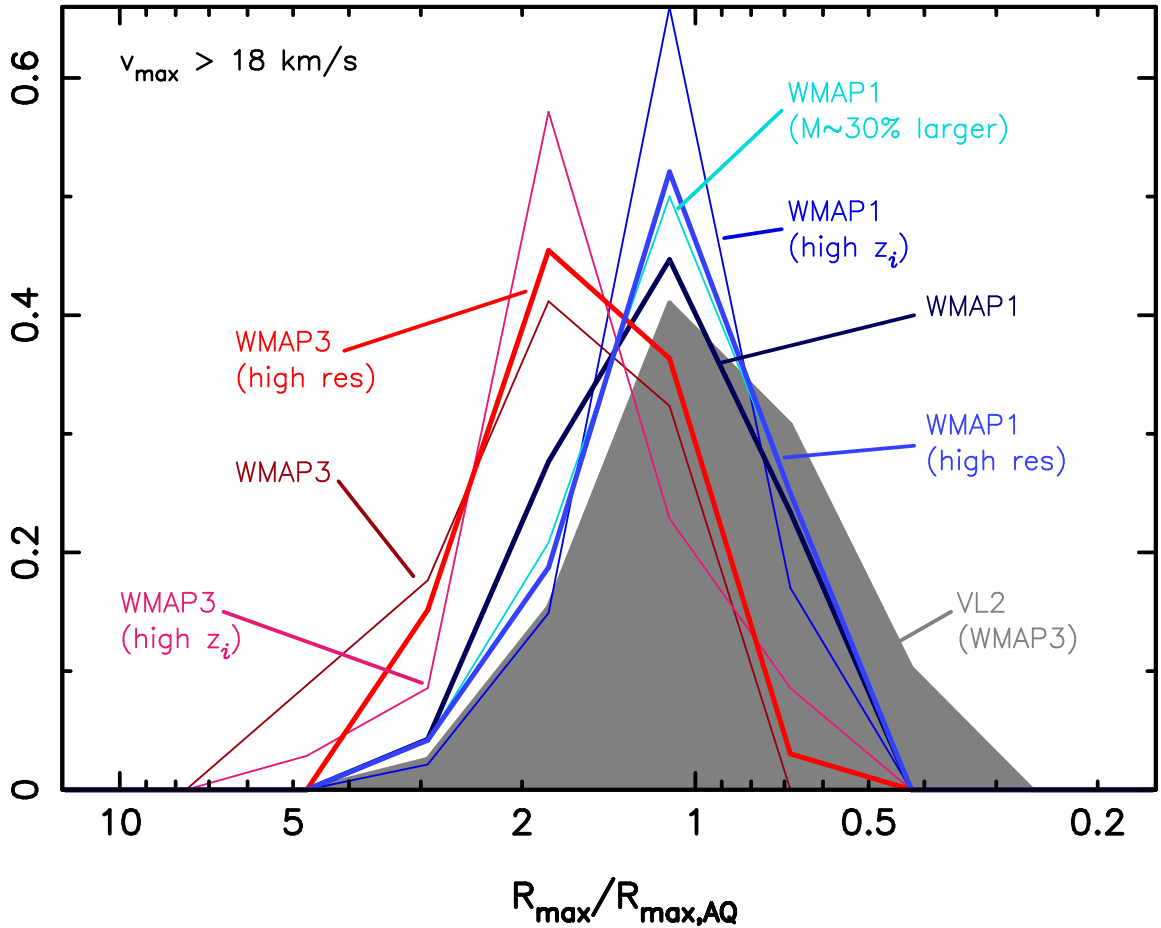
Figure 4.6: Distribution functions of R_{max} normalized to the Aquarius values for CDM subhalos with $v_{max} > 18$ km s^{-1} in the WMAP1 and WMAP3 simulations of the *set B* halo. Simulations adopting WMAP3 parameters are plotted in red while WMAP1 simulations are plotted in blue. The offset between simulations is consistent with a cosmology dependence and not on mass resolution, starting redshift, or mass of the host Milky Way halo. Solid gray area is the distribution for Via Lactea-II subhalos.

subhalos with $v_{max} > 18$ km s^{-1} to the Aquarius value of R_{max} from Equation 4.3 and present binned distributions for these subhalos and those of the Via Lactea-II (VL2) simulation ($z_i = 104$). I find consistent distributions between the low and high resolution simulations showing the mass resolution and softening length are sufficient to sample subhalos with $v_{max} > 18$ km s^{-1}. I also find weak to no dependence on the starting redshift as the simulations started from $z_i = 115$ have distributions consistent with the corresponding simulations started from $z_i = 48$. However, I do see a strong dependence on the cosmology as the WMAP3 simulations are offset to higher R_{max} compared to WMAP1. The offset is only weakly dependent on the mass of the Milky Way host as the WMAP1 simulations in the large and small boxes have nearly identical distributions.

Additional low resolution tests were run of the *set B* halo adopting WMAP9, Bolshoi, and Planck1 parameters. These simulations also show offsets from WMAP1 but less than the WMAP3 tests (final column in Table 4.3), as expected for the greater small scale power in these cosmologies. These tests show the subhalo concentrations are largely determined by their formation time. As the small scale power increases formation occurs earlier and the subhalos are more concentrated at $z = 0$. This is supported by examining the high redshift data for these simulations. Table 4.3 gives the number of halos with masses $> 2 \times 10^8 M_\odot$ and the average mass of the 12 largest halos in the high resolution volume at $z = 9$ in the test simulations of the *set B* halo with mass resolution $7.34 \times 10^5 M_\odot$. In the high resolution volume at $z = 9$ there are more than six times as many halos with masses $> 2 \times 10^8 M_\odot$ in the WMAP1 simulation than in WMAP3. Furthermore, the 12 most massive halos

are an average of four times as massive in WMAP1 than WMAP3. This is evidence
dwarf-scale halos are collapsing earlier and have more time to grow in a WMAP1
cosmology.

Table 4.3: Comparison of the low resolution CDM tests of the *set B* halo with a
common mass resolution. See text for an explanation of quantities in the columns.

| Name | $N_{z=9}$ | $< M_{top12} >$ | $\frac{R_{max}}{R_{max,WMAP1}}$ |
	$> 2 \times 10^8 M_\odot$	$[10^9 M_\odot]$	
WMAP1	378	2.939	1.0
Planck1	239	1.982	1.06
WMAP9	193	1.612	1.16
Bolshoi	149	1.375	1.20
WMAP3	57	0.777	1.57

The distribution of VL2 subhalos is also plotted in Figure 4.6. The VL2
simulation used WMAP3 cosmology but its subhalos have concentrations consistent
with Aquarius. I hypothesize this is because the VL2 halo has a higher redshift
of formation than the mean for a WMAP3 cosmology. Figure 4.4 shows my halos
generally have accreted less of their final mass at $a < 0.5$ than the VL2 halo. For
example, at $a = 0.25$ the VL2 halo has 23% of its final mass while my halos have only
$5 - 18\%$ of their final masses. Further evidence comes from the halo concentration
which is known to correlate with formation epoch. I determined M_{200} and R_{200}
$(1.417 \times 10^{12} M_\odot$, 225.28 kpc) from the fit to the VL2 density profile (Diemand
et al. 2008) and calculate c_{200} from Eqn 4.2. The concentration of VL2 is 10.7, in
contrast with the $6.6 - 8.7$ concentrations of my WMAP3 halos. VL2 is a 2.4σ outlier
in the WMAP3 simulations of Macciò et al. (2008) where the average concentration
of relaxed $10^{12} M_\odot h^{-1}$ halos is 5.9.

4.3.1.1 Velocity profiles

A direct comparison of the subhalo circular velocity profiles to the half-light circular velocities of the observed dwarfs is desirable but is complicated by two effects. The circular velocity is a cumulative quantity and its profile is affected by the softening length to greater distances than the density profile (Zolotov et al. 2012) making reliable inward extrapolation difficult. Additionally, the hosts of the bright dwarfs are expected to be the largest subhalos over the complete infall history of the subhalo population or the largest at the epoch of reionization. Many of these subhalos will experience tidally stripped mass loss thereby reducing their R_{max} sufficiently to become affected by the softening length. The largest subhalos at present ($z = 0$) are generally subhalos just beginning to infall as indicated by their large spatial extent (Anderhalden et al. 2013). They are the least affected by stripping and therefore have the most reliable circular velocities. Excluding Magellanic Cloud analogs from the simulations, 5-6 of the 10 subhalos with greatest v_{max} at $z = 0$ are among the top 10 with greatest v_{infall} while 2-4 are among the top 10 with greatest v_{max} at $z = 9$. Thus while the largest subhalos at $z = 0$ are not expected to completely match the observed dwarf population they are useful for illustrating the effects of cosmology on the too big to fail problem.

Plotted in Figure 4.7 are the NFW circular velocity profiles with R_{max} and v_{max} values of the 10 largest subhalos in each CDM simulation adopting WMAP1 and Bolshoi cosmologies. The data points with error bars show the circular velocities at half light radii from Wolf et al. (2010) for the sample of bright Milky Way dwarfs.

While there is some halo-to-halo scatter the reduced densities and shift of the profiles to larger radii in the Bolshoi cosmology is dramatically clear.

4.3.2 Warm Dark Matter

The results in the previous section show the discrepancy between the largest subhalos in CDM simulations and observations of bright Milky Way dwarfs may largely be due to the adopted cosmological parameters of the Aquarius simulation and that adopting parameters in agreement with the most recent WMAP release would greatly alleviate this problem. However I also saw that even a WMAP3 simulation like VL2 can have massive satellites dynamically inconsistent with the bright dwarfs implying a dependence on the formation history of the Milky Way and its satellites. In this section I investigate the effects warm dark matter has on the massive subhalos.

Figure 4.8 is a plot of v_{max} and R_{max} for subhalos in each simulation set for each WDM cosmology. Again, it is clear there are many subhalos that lie in the area consistent with the MW dwarfs but there are some with $v_{max} > 20$ km s^{-1} that do not, however the number of outliers decreases as the particle mass decreases. An average of 2 subhalos per simulation are outside the allowed region decreasing to 1.5 per simulation in 3 keV, < 1 in 2 keV, and 0 in 1 keV. An average of 2 subhalo outliers per Bolshoi CDM simulation were found demonstrating the minimal effect a 4 keV cosmology has on the densities.

The effects of WDM are a reduction in the total number of subhalos as well
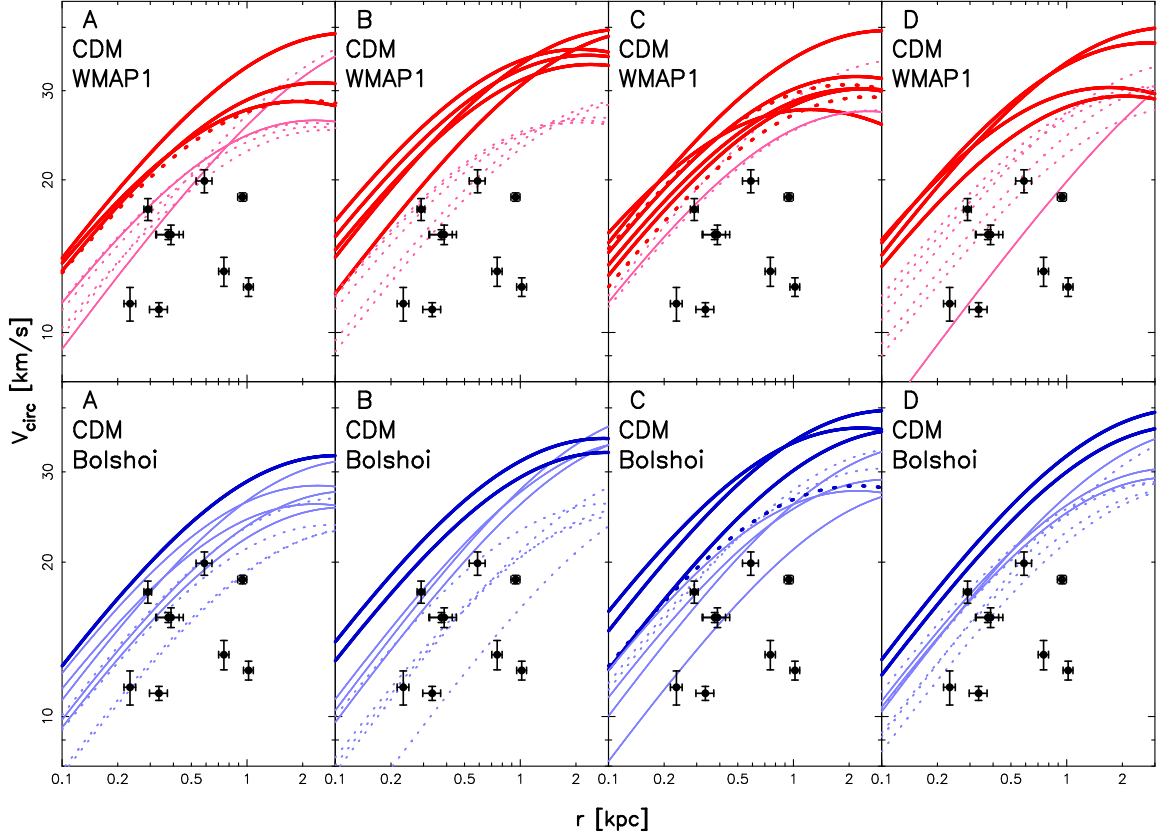
Figure 4.7: NFW circular velocity profiles for the 10 subhalos with largest v_{max} at $z = 0$ in each CDM simulation adopting WMAP1 cosmology (*top row*); and Bolshoi cosmology (*bottom row*) after filtering Magellanic Cloud analogs. Subhalos denser than any observed dwarf (points with error bars) are plotted in bold. Subhalos that are neither among the 10 with largest v_{infall} or 10 largest v_{max} at $z = 9$ are not expected to host a bright dwarf and are plotted with dotted lines. Note that NFW profiles for the 10 subhalos with largest v_{max} over their infall history select a few subhalos with lower values of v_{max} and R_{max} than shown here, further alleviating the discrepancy with observations.
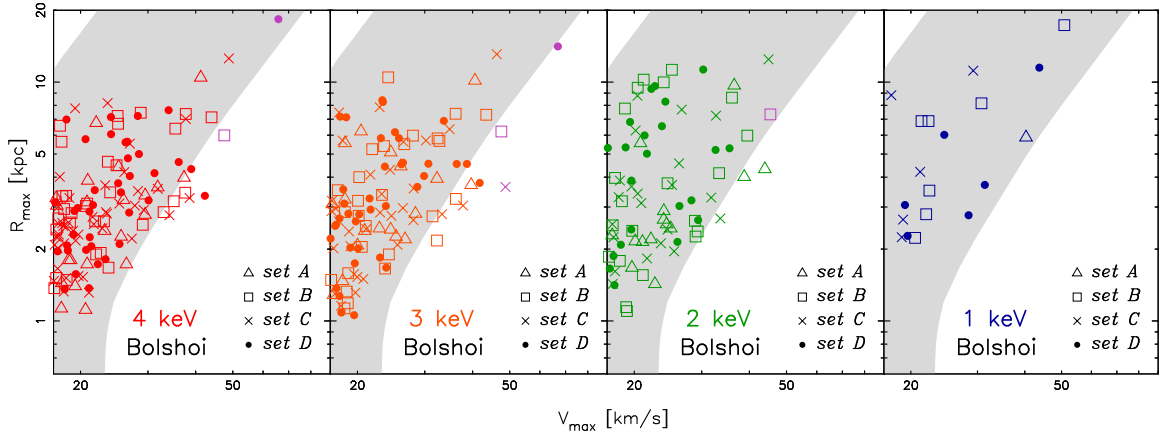
Figure 4.8: Plots of v_{max} and R_{max} for subhalos in the high resolution WDM simulations adopting Bolshoi cosmological parameters. The shaded area shows the 2σ constraints for the bright Milky Way dwarfs assuming NFW profiles. Magellanic Cloud analogs are colored purple.

as their circular velocities and an increase in their R_{max}. I estimate the increase in R_{max} by fitting equations of the form of Eqn 4.3 to the WDM subhalo data and comparing to the fits for the corresponding CDM simulation. I find, for constant values of v_{max}, R_{max} values are increased an average of 7% in 4 keV, 15% in 3 keV, 30% in 2 keV, and 46% in 1 keV; however, the small number of subhalos in 1 keV makes it difficult to achieve a reliable estimate for this cosmology.

The effects of WDM on the circular velocities can be estimated by comparing the velocities at several radii in the range $1-3$ kpc for subhalos in WDM compared to the corresponding CDM simulation. I find the subhalos in 1 keV WDM have velocities up to 60% less than their CDM counterparts. This reduction decreases to 20% in 2 keV, 15% in 3 keV, and only 10% in 4 keV.

4.3.2.1 Velocity profiles

Figure 4.9 shows the NFW circular velocity profiles of the 10 subhalos with the largest v_{max} at $z = 0$ in the WDM simulations after excluding Magellanic Cloud analogs.

The subhalo profiles are severely affected in the 1 keV cosmology with both the velocities and R_{max} values showing large changes. The 1 keV simulations struggle to match the observations in number and density with only *set D* managing to fit both.

Comparison to the CDM subhalos plotted in Figure 4.7 shows some scatter among individual subhalos. For example, a few subhalos in *set B* have increased density in WDM. In general, subhalo densities are significantly reduced in cosmologies warmer than 2 keV while at higher particle masses the effects are weak. This is in agreement with the single-halo simulations in Schneider et al. (2013) and Lovell et al. (2013).

4.4 Discussion

I found the concentrations and velocity profiles of subhalos in CDM simulations are dependent on the adopted cosmological parameters. I tested and found little to no dependence on the starting redshift, the mass resolution, the mass of the parent halo, and the halo finding software.

A cosmological dependence is also seen in other published work of Milky Way-sized galaxies. The simulations of Stoehr et al. (2002) used similar parameters
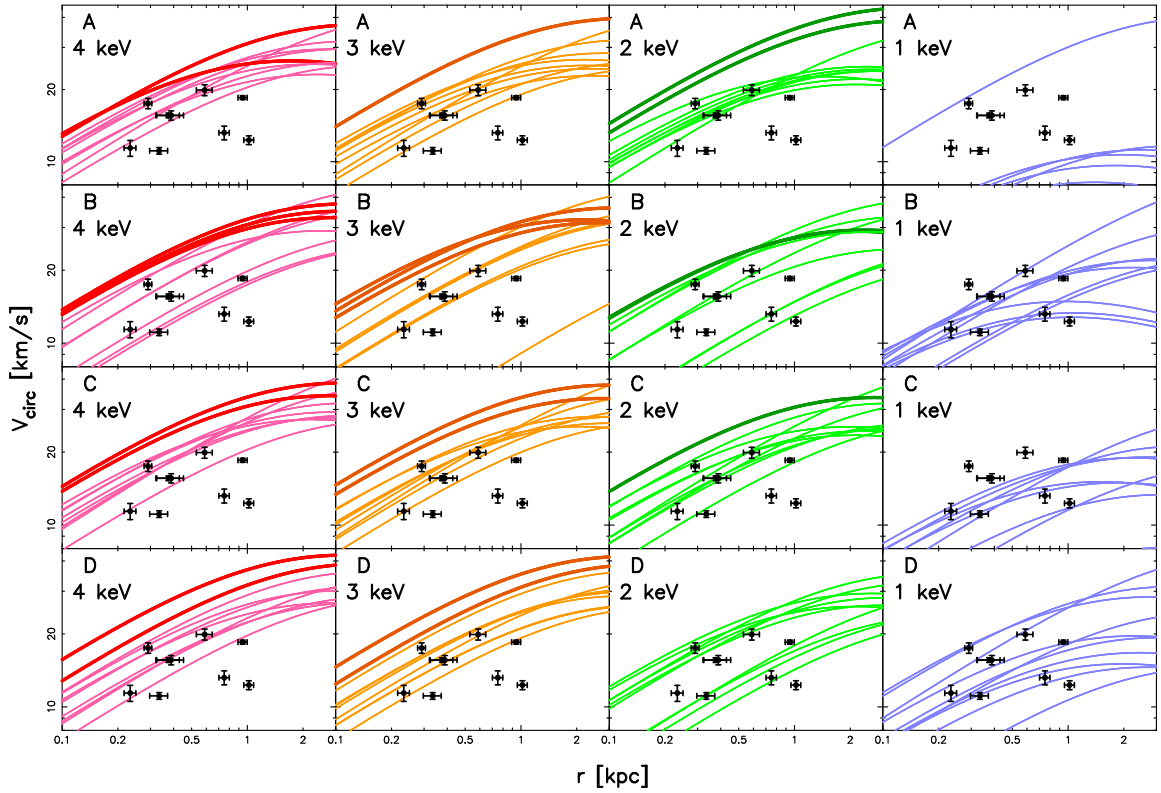
Figure 4.9: NFW circular velocity profiles for the 10 subhalos with largest v_{max} at $z = 0$ in each WDM simulation adopting Bolshoi cosmology. Subhalos denser than any observed dwarf (points with error bars) are plotted in bold.

to Aquarius, $(\Omega_m, \Omega_\Lambda, h, \sigma_8, n_s) = (0.3, 0.7, 0.7, 0.9, 1)$, and are well fit by Equation 4.3. di Cintio et al. (2011) saw an offset in their simulations using WMAP3 and WMAP5 parameters. A dependence of substructure central densities on the cosmological parameters is predicted in the work of Zentner and Bullock (2003) using the semianalytic model of Bullock et al. (2001a). The central densities are expected to reflect the mean density of the universe at the time of collapse. Adopting values for cosmological parameters that moves the formation of small mass halos to later epochs will result in less concentrated subhalos.

Here I show how the subhalo densities can be simply related to the power at their mass scale and therefore dependent on both σ_8 and n_s. The parameter σ_8 sets the power at a scale of 8 Mpc h^{-1} corresponding to a mass of about $2.5 \times 10^{14} M_\odot$. If the masses of the largest satellites are about $10^{10} M_\odot$, the wave number is $k_{sat} \sim 30 k_8$ where k_8 is the wave number corresponding to 8 Mpc h^{-1}. The change in σ between WMAP3 and WMAP1 values of n_s is given by:

$$\frac{k_{sat}}{k_8}^{(n_{s,WMAP3} - n_{s,WMAP1})/2} \sim 0.92. \tag{4.4}$$

The change due to σ_8 is:

$$\frac{\sigma_{8,WMAP3}}{\sigma_{8,WMAP1}} \sim 0.82. \tag{4.5}$$

The total change at the satellites scale is $0.92 \times 0.82 = 0.76$. This is also proportional to the change of the redshift of formation:

$$(1 + z_f)_{WMAP3} = 0.76(1 + z_f)_{WMAP1}. \tag{4.6}$$

The virial radius is proportional to R_{max} at virialization and the circular velocity at

the virial radius is proportional to v_{max} at virilization and:

$$R_{vir} \propto v_{vir}(1 + z_f)^{-1.5}. \tag{4.7}$$

Therefore the following scaling between cosmologies is obtained:

$$\frac{R_{max,WMAP3}}{R_{max,WMAP1}} = 0.76^{-1.5} = 1.51. \tag{4.8}$$

Repeating this for the scaling between Bolshoi and WMAP1 cosmologies yields a factor of 1.31. From my simulations I derived average scaling factors of 1.40 and 1.35 for WMAP3 and Bolshoi, respectively, with a scatter of 0.10. This is in good agreement with the rough calculation that assumes a mass of $10^{10} M_\odot$ for the large satellites and neglects tidal effects that may introduce a cosmology dependent change of the present values of R_{max} and v_{max} from the values at virialization. An approximate general scaling relation for R_{max} at a fixed v_{max} can be written:

$$R_{max} \propto (\sigma_8 5.5^{n_s})^{-1.5}. \tag{4.9}$$

This equation gives a scaling of 1.24 between Planck1 and WMAP1.

I also investigated how the subhalo densities are affected in a range of WDM cosmologies and quantified the reduction in circular velocity at kpc scales. In the previous chapter I showed that the abundance of Milky Way satellites, including the ultra-faint dwarfs discovered in the SDSS, allow a lower limit of 2.1 keV to be placed on the dark matter particle mass. The work of Lovell et al. (2013) favors a similar but slightly warmer limit of 1.6 keV. Several authors have used Lyman-α data to provide independent constraints on WDM with lower limits ranging from 1.7–4 keV (Boyarsky et al. 2009; Viel et al. 2006; Seljak et al. 2006; Viel et al. 2008, 2013).

Under these constraints I expect the circular velocities of the largest satellites in WDM to be affected by less than 20%, much less than the 60% changes seen in a 1 keV cosmology. I conclude that WDM cosmologies colder than ~ 2 keV have only a mild effect on the density of massive Milky Way satellites, that are instead most sensitive to the redshift of formation of the Milky Way and the power at small scales given by σ_8 and n_s. Interestingly, if the ~ 3.5 keV X-ray emission observed from galaxy clusters is caused by a sterile neutrino with properties similar to a ~ 2 keV thermal relic my work shows it will naturally account for the observed densities of the bright Milky Way dwarfs.

While my simulations adopting Bolshoi cosmology reduced the number of "too big to fail" subhalos in 3/4 of the Milky Way realizations from about four or five in WMAP1 to about one or two, none of my simulated Milky Ways are completely free of overdense subhalos. Furthermore, the case of the VL2 halo demonstrates that large variation in average subhalo density is possible even in WMAP3 cosmologies. Purcell and Zentner (2012) examined $10,000$ realizations of substructure for three host Milky Way masses from an analytic model. While their technique is only an approximation to direct simulation they find $\sim 10\%$ of their subhalo populations have no massive failures in a WMAP7 cosmology. The Milky Way may thus simply be mildly atypical. Interestingly, Hammer et al. (2007) show the Milky Way is deficient in stellar mass, disk angular momentum, and average iron abundance of stars in the Galactic halo at the 1σ level. Only $7\% \pm 1\%$ of spiral galaxies with comparable rotation speeds have similar properties. One way of explaining these discrepancies is to assume the Milky Way had a quiet accretion history without

major merger events for the past ~ 10 Gyr. Figure 4.4 shows VL2 and the *set B* and *set C* halos assemble $\sim 70\%$ of their mass by $z = 1.5$ and may better represent the Milky Way than the other halos, according to this model. Opposite to expectations these halos have the highest number of outliers. However, Purcell and Zentner (2012) found selecting hosts for quiet accretion histories did not significantly increase the probability of consistency.

My simulations assumed the dark matter was purely cold or purely warm, but a mixture of the two is possible. The transfer function of mixed dark matter is characterized by a step related to the particle mass and a plateau at smaller scales related to the fraction of the warm component. This could arise if the dark matter is composed of multiple particle species or a single species containing warm and cold primordial momentum distribution components caused by separate production stages, for example. Boyarsky et al. (2009) allowed for mixed cold and warm dark matter in their analysis of Lyman-α forest data. They find a particle mass of 1.1 keV is allowed if the WDM fraction is less than 0.4 (95% confidence). Masses below 1 keV are allowed provided the fraction of WDM is less than 0.35. Anderhalden et al. (2013) examined a subhalo population in several mixed dark matter cosmologies. They show a range of models that agree with Lyman-α constraints can be ruled out for failing to produce subhalos with sufficient density to match the observations, highlighting the usefulness and uniqueness of the Milky Way satellites as a probe of small-scale cosmology.

Chapter 5:   The Universal Density Profile That Wasn't

5.1   Overview

The seminal work of Navarro et al. (1996) found that the density structure of relaxed dark matter halos are well represented by what has become known as the NFW profile:

$$\rho(r) = \frac{\rho_s}{(r/r_s)(1 + r/r_s)^2},$$ (5.1)

where $\rho(r)$ is the density in a spherical shell at distance r from the halo center. By scaling the free parameters r_s and ρ_s, which define a characteristic length and density, the NFW profile can describe dark matter halos from dwarf galaxy to cluster scales. Furthermore, it was found the NFW profile was valid for halos regardless not only of mass but also the power spectrum of initial density fluctuations and values of cosmological parameters, establishing that density profiles are universal in form independent of the cosmological context (Navarro et al. 1997). Another universal property was found in the coarse-grained phase-space density profile, $Q \equiv \rho/\sigma^3$, where σ is the velocity dispersion of simulation particles. Taylor and Navarro (2001) discovered Q has a remarkably simple form of a power-law, $Q \propto r^\alpha$, with $\alpha \sim -1.9$.

It is useful to recast the free parameters of the NFW profile in terms of a halo

mass and concentration. For relaxed halos a radius can be defined in which the material has reached virial equilibrium:

$$M_{vir} = \frac{4\pi}{3}\Delta(z)\rho_c(z)R_{vir}^3, \tag{5.2}$$

where R_{vir} is the virial radius enclosing a density Δ times the critical density, ρ_c, at redshift z. In a matter dominated Einstein-de Sitter cosmology, $\Delta = 178$. With the virial radius defined the characteristic radius r_s can be recast as the concentration parameter, $c_{vir} \equiv R_{vir}/r_s$. Much effort has gone into understanding the relationship between c_{vir} and M_{vir} as well as the dependencies on the background cosmology and the evolution with redshift (Prada et al. 2012). This is necessary for predicting the properties of luminous galaxies that reside in the dark matter halos and for using galaxy observations as probes of the CDM paradigm. The concentration was found to correlate with mass such that smaller mass halos are more concentrated. This was understood as a consequence of the earlier formation epoch of small mass halos in the bottom-up structure formation of CDM. Since small halos collapse earlier their inner regions reflect the higher universal density of matter at earlier times. Changing the cosmological parameters or the power spectrum changes the halo formation epoch and affects the concentrations but does not affect the shape of the universal profile. This interpretation is consistent with simulations of hot and warm dark matter which found halos with masses below the truncation scale form later and have lower concentrations than CDM halos of similar size (Avila-Reese et al. 2001; Bode et al. 2001; Knebe et al. 2002).

Much effort has also gone into understanding the physical processes that pro-

duce the NFW profile. There are two basic approaches to analytically modeling the density profile: smooth accretion based on spherical infall (Gunn and Gott 1972; Gott 1975), and hierarchical merging following Press-Schechter formalism (Press and Schechter 1974; Peebles 1974; Lacey and Cole 1993; Manrique et al. 2003). Both approaches have been successful at producing the universal profiles. This has been explained as a result of the process of virialization. If virialization erases all information about the past merging history of the halo then it will not matter if the mass accretion is modeled as clumpy or smooth. However, a consensus has not emerged on the dominant processes occurring during virialization or if the virialization process erases all memory of the initial conditions.

The early stages of halo formation are marked by rapid accretion and mergers making it natural to consider violent relaxation as the dominant mechanism determining the dark matter profiles in the fluctuating gravitational potential (White 1996). Violent relaxation was originally proposed to explain the structure of elliptical galaxies (Lynden-Bell 1967) where estimates of star-star encounters would not establish equilibrium in a Hubble time. The relaxation time of a forming halo is related to the rate of change of the gravitational potential. Austin et al. (2005) and Barnes et al. (2006) argue the universal nature of $Q(r)$ results from violent relaxation.

The works of Wechsler et al. (2002); Zhao et al. (2003a,b, 2009) have shown there are two main eras of halo growth, a fast accretion phase and a slow phase. The fast growth phase in CDM is dominated by mergers of objects with similar mass in contrast to the slow growth phase characterized by quiescent accretion and

minor mergers. The inner halo is set at the end of the fast era with the slow growth phase having little impact on the inner structure and gravitational potential well, leading to an inside-out growth of halos. These studies find violent relaxation is only important in forming the inner profile with the outer profile determined by secondary infall during the slow growth phase.

The NFW profile is characterized by a logarithmic slope, $\gamma \equiv d\log\rho/d\log r$, that rolls from an asymptotic value $\gamma = -3$ at large radii to $\gamma = -1$ in the inner halo. The value of the inner slope has been a matter of controversy. The first concerned the value of the asymptotic slope (Moore et al. 1999b). As the number of particles in simulations have increased it has become evident the density profiles do not approach an asymptotic value in the center but continue to roll slowly with radius (Navarro et al. 2004; Diemand et al. 2004; Graham et al. 2006) and are better described by Einasto profiles (Einasto 1965). However, this has not changed the conclusion that all information about the formation history is lost in the virialization process.

The second controversy is a possible dependence of the inner profile on the halo mass. Many models have been constructed that explain the emergence of the universal profile as a consequence of repeated mergers (Syer and White 1998; Nusser and Sheth 1999; Subramanian et al. 2000; Dekel et al. 2003). Although they differ in the details, the relevant physical processes determining the halo properties are the tidal stripping of material from accreting subhalos, dynamical friction, and tidal compression transferring energy from the satellites to the halo particles and the decaying of satellite orbits to the halo center. These models predict a dependence of the inner density profile slope on the slope of the power spectrum at the scale of the

halo, $P(k) \propto k^n$. The steeper spectrum characteristic of dwarf-scales is predicted to produce softer cores than for galactic and cluster-scale halos. Independent of the merger models, Del Popolo (2010) questions the universality of both the density and the Q profile and concludes both should depend on mass. His spherical infall models with angular momentum show a steepening of the inner density profile with increasing halo mass, although to a lesser extent than the merger models.

The heart of the issue is, do halos in equilibrium retain any memory of the initial conditions and mass function of accreting satellites they are built from or is all information lost in the virialization process?

Ricotti (2003) ran CDM simulations of the same realization of the density field in boxes of varying side length to compare the profiles at different mass scales. He examined the average profiles when the box structures showed similar clustering and the most massive halos were composed of the same number of particles. He found a systematic dependence of the inner slope on halo mass with dwarf-scale halos having softer cores than galactic and cluster-scale halos in agreement with the predictions of Subramanian et al. (2000). These results were reinforced in Ricotti et al. (2007). Jing and Suto (2000) also saw a dependence of inner slope in their simulations of halos at galactic and cluster scales.

Another way of testing the importance of substructure is by introducing a truncation in the power spectrum as in hot and warm dark matter cosmologies where substructure is suppressed below the particle free-streaming scale and halos form by monolithic collapse. Many investigations using these cosmologies have been conducted (e.g. Wang and White 2009, Huss et al. 1999a, Moore et al. 1999a,

Colín et al. 2000, Busha et al. 2007, Bode et al. 2001). These works find halos that form below the truncation scale have lower concentrations consistent with the later formation epochs of these halos but the profiles are well described by the NFW form. This is in contrast to Colín et al. (2008) who find the profiles are systematically different in their WDM simulations of Galaxy-sized halos. They find profiles are steeper in the inner regions and the densities greater than the best fitting NFW profile. Williams et al. (2004) and Viñas et al. (2012) have independently modeled the density profiles of WDM halos and predict a flattening of the inner profile due to the truncated power spectrum.

In this work I employ N-body simulations of halo formation in CDM and WDM cosmologies to explore the effects of the power spectrum on halo structure and dynamics. I use the method of Ricotti (2003) of scaling the simulation volume to change the mass scale. However, I do not study a statistical sample of halos but focus on one halo with about a factor of 100 greater mass resolution than in Ricotti (2003). The goal is not to rigorously test any particular halo model but simply to look for evidence the halo retains some memory of the initial power spectrum. This evidence is expected to manifest itself as trends in the halo profiles as the mass and truncation scales change. I examine if my results are typical of a larger halo population and investigate the physical origin of my results.

5.2 Numerical Simulations

5.2.1 Cosmological Models

WDM particles are relativistic in the early universe and free-stream out of overdense regions before the adiabatic expansion of the universe reduces the particles to subrelativistic velocities. WDM thus damps density perturbations below a characteristic scale that depends on the particle mass and acts as a filter on the power spectrum of density perturbations. The power spectra for WDM cosmologies is related to that for CDM by

$$P_{WDM}(k) = P_{CDM}T^2_{WDM},\tag{5.3}$$

where T_{WDM} is the WDM transfer function. The transfer function given by Bode et al. (2001) is used for thermal relic dark matter particles that were coupled to the relativistic cosmic plasma at early times and achieved thermal equilibrium prior to the time of their decoupling. The formula of Eisenstein and Hu (1998) is adopted for the CDM power spectrum.

I define the WDM filtering mass as in Sommer-Larsen and Dolgov (2001),

$$M_f \equiv \frac{4\pi^4}{3}\Omega_m\rho_c k_f^{-3},\tag{5.4}$$

where ρ_c is the critical density and k_f is a characteristic free-streaming wave number defined where $T^2_{WDM} = 0.5$. For consistency with Sommer-Larsen and Dolgov (2001) I also define the free-streaming, or filtering length as $R_f \equiv 0.46k_f^{-1}$.

I adopted values for cosmological parameters from the Bolshoi simulation

(Klypin et al. 2011), $(\Omega_m, \Omega_\Lambda, \Omega_b, h, \sigma_8, n_s) = (0.27, 0.73, 0.0469, 0.7, 0.82, 0.95)$, which were chosen to be within 1σ of WMAP5, WMAP7, and consistent with the results of supernovae, and X-ray cluster surveys. These parameters are also within 1.7σ of WMAP9 and 2.2σ of Planck1. I use a variety of WDM models for thermal relics in the range $0.75 - 15$ keV. Figure 5.1 shows the WDM transfer functions for the cosmological parameters adopted in this work with the filtering masses indicated by the colored ticks across the top of the plot.

Since my focus is to examine the effects of the power spectrum on halo structure, the initial conditions include particle velocities due to the gravitational potential using the Zeldovich approximation but random thermal velocities appropriate for WDM have not been added to the simulation particles. For the WDM cosmologies adopted here the effects of thermal velocities are expected to be small; this is discussed further in Section 5.6.
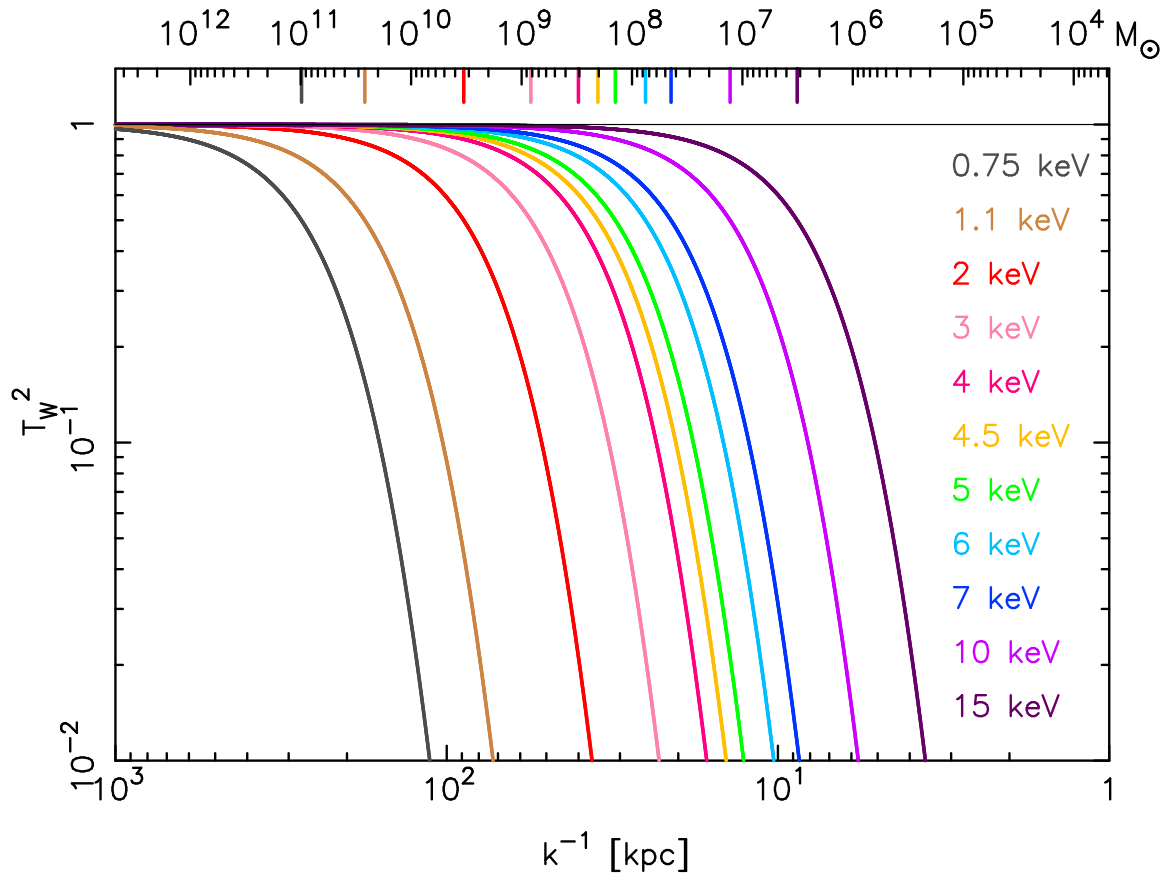
Figure 5.1: WDM transfer functions used in the simulations. The filtering masses, M_f, are marked along the top.

5.2.2   Software

The simulations were conducted with the N-body cosmological simulation code GADGET-2 (Springel 2005) with gravitational physics only and initial conditions generated with the GRAFIC2 software package (Bertschinger 2001). I produced a single realization of the density field but varied the power spectrum of fluctuations appropriate for CDM and WDM cosmologies.

The AMIGA's Halo Finder (AHF) software (Knollmann and Knebe 2009) was used to identify gravitationally bound halos and calculate their properties after iteratively removing unbound particles. The virial mass of a halo is defined in Equation 5.2. Since the simulations are confined to high redshifts ($z > 4$) the universe is matter dominated at all epochs and I adopt the virial condition for an Einstein-de Sitter cosmology, $\Delta(z) = 178$. The MergerTree tool in AHF was used to construct merger trees, identify halo progenitors at all times, and for identifying halos across cosmologies.

AHF calculates the convergence radius according to the criterion of Power et al. (2003) and is generally about 10 softening lengths, enclosing ~ 2000 particles at $r \sim 0.006 R_{vir}$. I tested this by running low resolution simulations and found the profiles are actually converged to about $5 - 6$ softening lengths, enclosing ~ 200 particles at $r \sim 0.003 R_{vir}$. The convergence radius given by AHF may be overly conservative for the simulations but this has no impact on the results. When examining the halo profiles I adopt the convention of plotting $r > 6\epsilon$ but I indicate in bold where the profiles satisfy the criterion of Power et al.

5.2.3 Simulations

I started at small scales by simulating a small cubic box with a comoving side length of 3.3 Mpc from $z = 79$ to $z = 8$ with 512^3 particles and mass resolution $\sim 10^4 M_\odot$. A halo of mass $\sim 2 \times 10^8 M_\odot$ that appeared to have an early formation epoch and relaxed to virial equilibrium at scale factor $a = 0.1$ was chosen for res-imulation using a zoom technique. I refer to this as "Halo A." A volume of higher mass resolution was generated in the initial conditions covering the initial volume of particles that end within three virial radii of Halo A. I ran high resolution simulations with the mass resolution increased a factor of 8^3 in CDM and multiple WDM cosmologies in the range $4 - 15$ keV. To test the convergence of the results I also ran low resolution simulations with the mass refinement reduced to a factor of 4^3 in CDM and 6 keV WDM. I further tested the dependence of the results on the initial conditions by running low resolution tests in CDM and 6 keV starting from $z = 120$.

I ran additional simulations at medium and large mass scales by increasing the box size to medium and large side lengths of 7.0 and 22.4 Mpc which increased the mass scale a factor of 10 and 320, respectively. CDM and WDM cosmologies ranging from $2 - 5$ keV were run for the medium mass scale while CDM and $0.75 - 2$ keV WDM were run for the large mass scale. To compare Halo A across mass scales I define "normalization times" as the epochs when the CDM halos have grown to encompass the same number of particles within the virial radius, $N \sim 10^7$, as the small mass scale at $a = 0.1$. This occurred at $a = 0.116$ and $a = 0.155$ in the medium and large mass scales, respectively. Figure 5.2 shows the growth of Halo

A at the three mass scales. Halo formation is delayed in the WDM cosmologies but once it begins it grows quickly until it catches up with the CDM halo, after which it evolves at a similar rate. The circles show the normalization times when the halo has entered the slow growth phase and is composed of the same number of particles in CDM at all mass scales. At the normalization times the halo masses are approximately $2 \times 10^8 M_\odot$, $2 \times 10^9 M_\odot$, and $6 \times 10^{10} M_\odot$ for the small, medium, and large mass scales, respectively.

To explore if the results for Halo A were typical of halos in general I ran additional sets of low resolution simulations with the refinement volume increased a factor of 30 over the Halo A simulations. In these simulations the refinement volume was cubic with a side length $1/4$ the box length, consisted of 512^3 particles, and was centered on Halo A. Simulations were run for CDM and 1.1 keV at the large mass scale and for CDM and 6 keV at the small scale. The 15 largest halos in the refinement volume were examined in detail. Six halos were chosen for individual resimulation at high resolution in an analogous way to Halo A, but only at large mass scale and only for CDM and 2 keV thermal relic cosmologies that correspond to the 7.1 keV sterile neutrino (Abazajian 2014) recently claimed to be indirectly detected via an X-ray line at 3.55 keV (Bulbul et al. 2014; Boyarsky et al. 2014).

Table 5.1 gives a summary of the simulations conducted in this work. Listed in the table are the WDM filtering mass and length, the simulation particle mass in low and high resolution, and the force softening length ϵ. All lengths are given in comoving units, in which the softening length was held constant. For the WDM cosmologies the box side length L_{box} is given in units of the filtering length. This
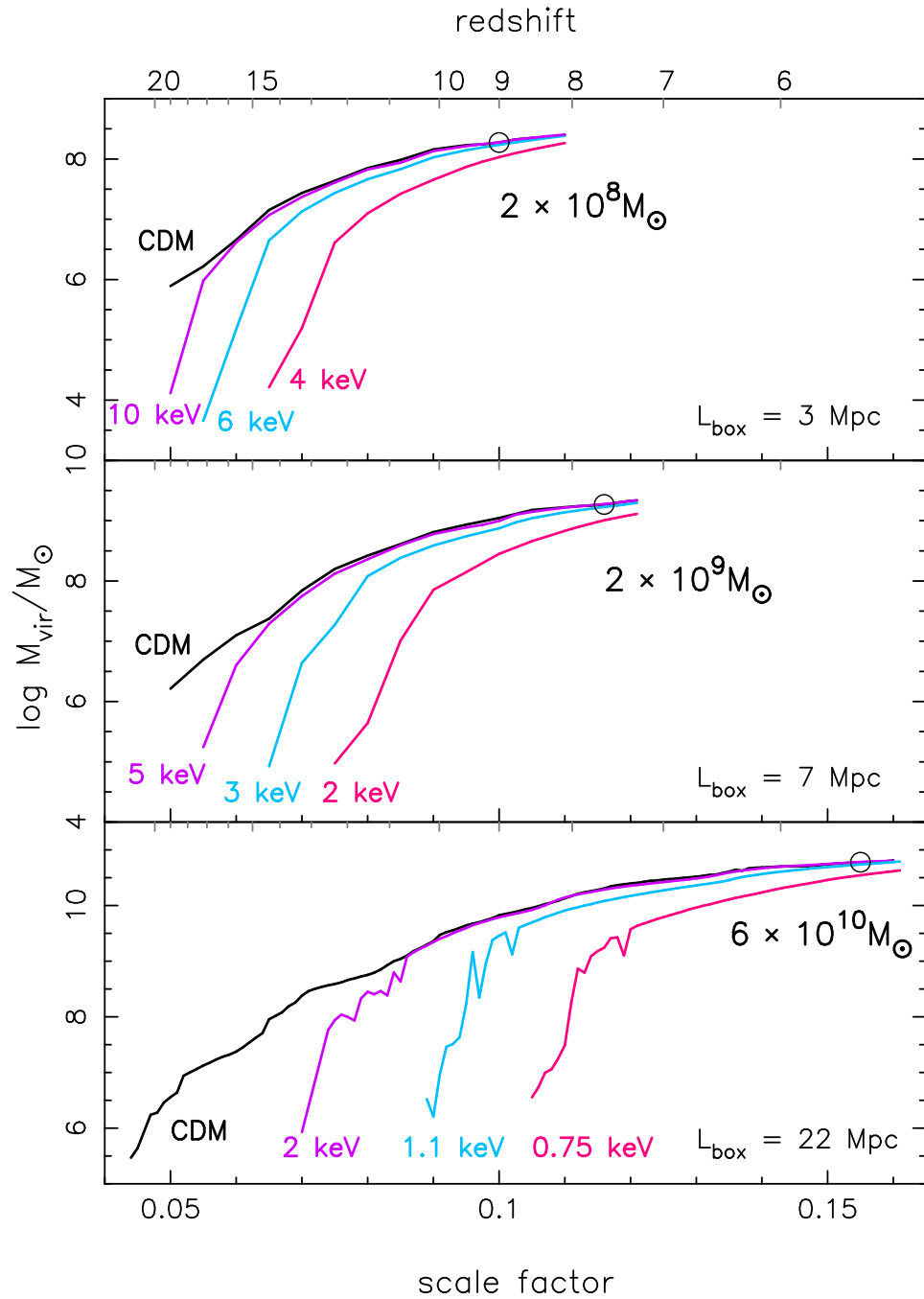
Figure 5.2: Mass growth of Halo A in the small, medium, and large box simulations (top to bottom) in CDM and select WDM cosmologies. The circles show the CDM halo at the normalization times when the halo has grown to $\sim 10^7$ particles at the three mass scales.

is a convenient way to show in which simulations the effects of the truncated power spectrum will be similar across mass scales. The 2 keV simulation in the large box is expected to be similar to the 5 keV medium box and 10 keV small box. Likewise, the 1.1 keV large box will be similar to the 3 keV medium box and 6 keV small box. The 0.75 keV large box will be similar to the 2 keV medium box and 4 keV small box. These simulations are color-coded in Figure 5.2. Another way of characterizing the similarity of these simulations is by the ratio of filtering mass to the virial mass of Halo A. For the similar cosmologies given above, the filtering masses are approximately 7%, 40%, and 170% of the halo virial masses at the normalization times.

Table 5.2 summarizes the properties of Halo A at the normalization times. An examination of Figure 5.2 shows Halo A has not suffered a recent major merger and is in the slow growth phase in all cosmologies at the normalization times. However, a more rigorous examination of the halo relaxation state is desirable. Differences from a universal profile are seen in unrelaxed halos and halos with large amounts of substructure (Jing 2000). Additionally, the inner slope of the density profile is sensitive to the location of the halo center. An artificial flattening of the profile could be produced by an ambiguously defined center due to a recently arrived subhalo at the core, for example. I performed a qualitative visual examination that the halo centers determined by AHF correspond to the density peak of particles and I examined quantitative measures of the relaxation. Neto et al. (2007); Macciò et al. (2007, 2008) have studied large samples of halos and identified several metrics for separating halos by relaxation: x_{off}, the offset between the halo center and center

Table 5.1: Properties of simulations.

Cosmo	M_f $[M_\odot]$	R_f [kpc]	L_{box}	$m_{low\ res}$ $[M_\odot]$	$m_{high\ res}$ $[M_\odot]$	ϵ [pc]
Large Box: 22 Mpc						
CDM	-	-	22394 kpc	48,080	6,010	55
2 keV	3.34×10^9	40.8	548 R_f	48,080	6,010	55
1.1 keV	2.63×10^{10}	81.2	276 R_f	48,080	6,010	55
0.75 keV	9.84×10^{10}	126.2	177 R_f	48,080	6,010	55
Medium Box: 7 Mpc						
CDM	-	-	7049 kpc	1,500	187	17
5 keV	1.41×10^8	14.2	495 R_f	1,500	187	17
4 keV	3.05×10^8	18.4	383 R_f	1,500	187	17
3 keV	8.24×10^8	25.6	275 R_f	1,500	187	17
2 keV	3.34×10^9	40.8	173 R_f	1,500	187	17
Small Box: 3 Mpc						
CDM	-	-	3270 kpc	150	18.7	8
15 keV	3.19×10^6	4.0	812 R_f	150	18.7	8
10 keV	1.29×10^7	6.4	510 R_f	150	18.7	8
7 keV	4.43×10^7	9.7	338 R_f	150	18.7	8
6 keV	7.54×10^7	11.5	283 R_f	150	18.7	8
5 keV	1.41×10^8	14.2	230 R_f	150	18.7	8
4.5 keV	2.03×10^8	16.1	203 R_f	150	18.7	8
4 keV	3.05×10^8	18.4	178 R_f	150	18.7	8

of mass of particles within R_{vir}; the virial ratio $2K/|U| - 1$; and the spin parameter λ' from Bullock et al. (2001b) that characterizes the halo angular momentum:

$$\lambda' = \frac{J}{\sqrt{2}M_{vir}v_{vir}R_{vir}}, \tag{5.5}$$

where J is the total angular momentum of all particles within R_{vir} and v_{vir} is the circular velocity at R_{vir}, $v^2 \equiv GM/R$. These metrics are listed in Table 5.2. The general conditions for a relaxed halo are: $x_{off} < 0.1R_{vir}$, $\lambda' < 0.1$, and $2K/|U| - 1 < 0.5$. Halo A satisfies these criteria in all simulations.

Table 5.2: Properties of Halo A at the normalization times in high resolution simulations.

Cosmo	a	M_{vir} $[10^8 M_\odot]$	λ' $[10^{-2}]$	x_{off} $[R_{vir}]$	$\frac{2K}{|U|} - 1$
(1)	(2)	(3)	(4)	(5)	(6)
Halo A - Small Box					
CDM	0.1	1.868	4.21	0.06	0.41
15 keV	0.1	1.888	4.24	0.05	0.42
10 keV	0.1	1.887	4.63	0.09	0.42
7 keV	0.1	1.811	4.88	0.08	0.40
6 keV	0.1	1.713	4.80	0.07	0.40
5 keV	0.1	1.507	4.30	0.06	0.39
4.5 keV	0.1	1.330	3.93	0.06	0.39
4 keV	0.1	1.074	3.16	0.06	0.41
Halo A - Medium Box					
CDM	0.116	18.533	4.09	0.06	0.39
5 keV	0.116	18.894	4.63	0.06	0.41
4 keV	0.116	18.533	4.77	0.07	0.41
3 keV	0.116	16.912	4.76	0.07	0.40
2 keV	0.116	10.126	3.10	0.05	0.40
Halo A - Large Box					
CDM	0.155	600.497	3.34	0.04	0.39
2 keV	0.155	604.681	4.07	0.08	0.40
1 keV	0.155	547.367	4.44	0.07	0.39
0.75 keV	0.155	351.273	3.48	0.04	0.38

5.3 Results I - Non-universality Of Profiles

I begin by examining the effects of the WDM power spectra on the density structure of Halo A in the three boxes and thus the three mass scales of the halo. I then examine the kinematics and conclude by checking the convergence. In Section 5.4 I examine a larger halo sample to check if the results of Halo A are typical for halos in general.

5.3.1 Density Structure

Figure 5.3 shows the spherically averaged density profiles of Halo A at $a = 0.1$ in all cosmologies of the small mass simulations, $M = 2 \times 10^8 M_\odot$. The profiles are plotted with solid lines where they satisfy the convergence criterion of Power et al. (2003) and the inner profiles are extended to six force softening lengths with dotted lines. At $r > 0.4R_{vir}$ the profiles are consistent across cosmologies. In the range $0.1 - 0.4R_{vir}$ the WDM densities are below that of CDM and at $r < 0.1R_{vir}$ the WDM simulations have greater density than CDM. The location where the WDM density begins to increase shows a correlation with filtering scale, moving to larger radii as the cosmology gets warmer and the filtering scale larger.

This feature is more pronounced in the cumulative mass profiles shown in Figure 5.4. The enclosed mass is equivalent in CDM and WDM at $> 0.5R_{vir}$ indicating it is the mass in shells at $0.1 - 0.4R_{vir}$ that has been displaced to smaller radii in the WDM simulations.

I next check for differences in the triaxiality of the halos. Figure 5.5 shows
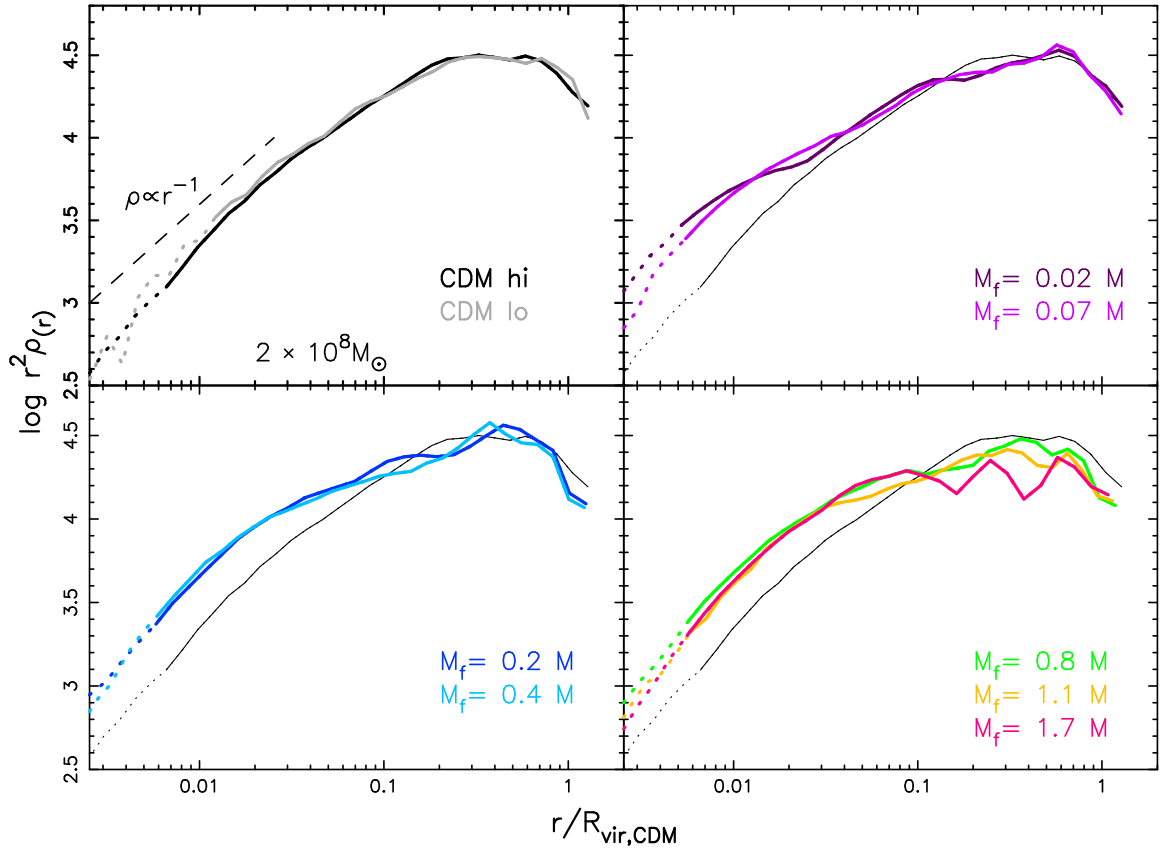
Figure 5.3: Density profiles of the small mass simulations of Halo A at the normalization time, $a = 0.1$. The densities have been multiplied by r^2 to reduce the dynamic range. The radial coordinates have been normalized to the virial radius in CDM and are plotted to 6ϵ. The WDM profiles have been grouped and are plotted against the CDM profile for clarity. All profiles are plotted with solid lines where they satisfy the convergence criterion of Power et al. (2003). The dashed line gives the asymptotic slope of the NFW profile at small radii. Clear deviations from a universal shape are seen in the WDM profiles.
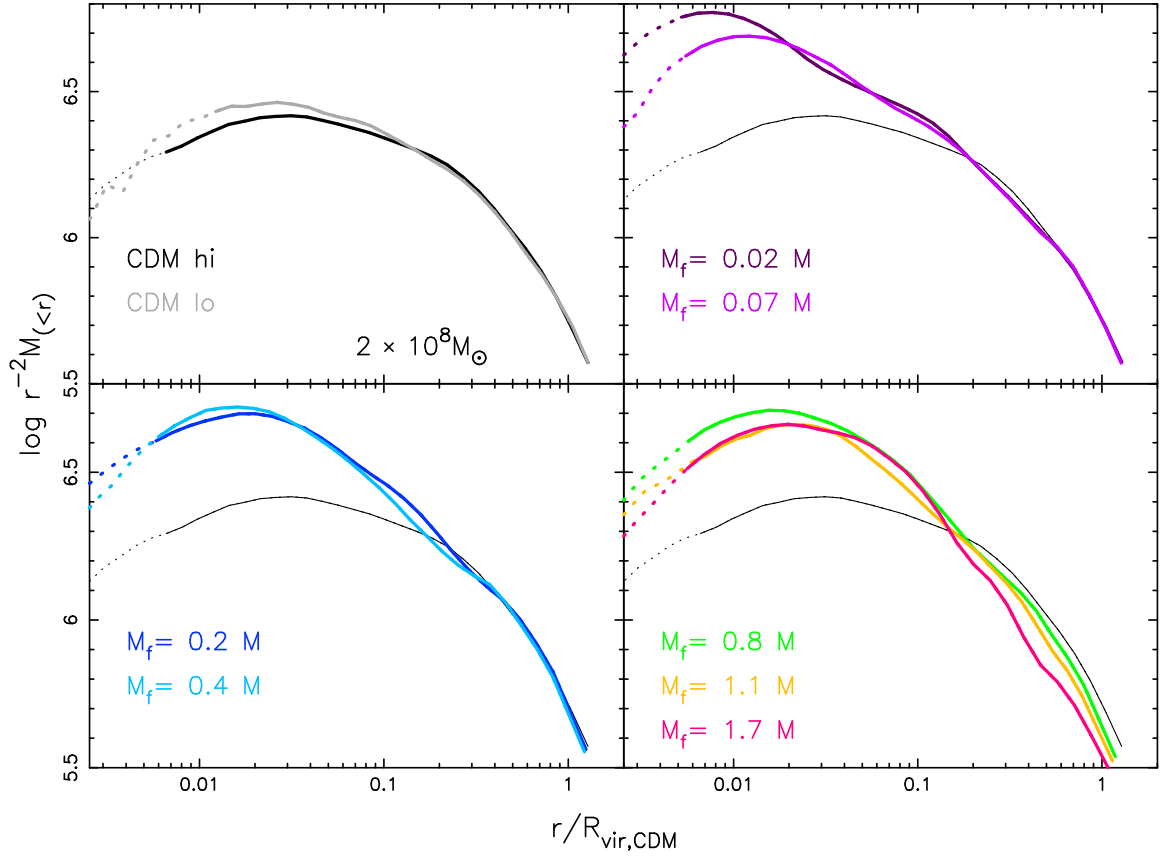
Figure 5.4: Cumulative mass profiles of the small mass simulations of Halo A. The mass profiles have been multiplied by r^{-2} to reduce the dynamic range. WDM simulations have been grouped and plotted against the CDM profile for clarity. Mass has been displaced from intermediate radii to the core in the WDM simulations.

radial profiles of the axial ratios of Halo A in the small box simulations. The axial ratios tend to become more spherical in the inner and outer regions at $r < 0.02R_{vir}$ and $r > 0.2R_{vir}$ and less spherical in the intermediate regions as the cosmology changes from cold to warm.

To compare the mass profiles of Halo A across the three mass scales I plot in Figure 5.6 the profiles of enclosed number of simulation particles and normalize the radial coordinates by the CDM virial radius for each mass scale. Interestingly, variations as a function of halo mass are seen at $r < 0.1R_{vir}$ in the CDM halos in contrast to the WDM simulations where the profiles are nearly identical across the explored range of halo masses. The enclosed mass in the CDM inner halo becomes greater as the halo mass increases but when small scale structures are erased, as in the WDM simulations, the profiles are insensitive to the halo mass. Angular momentum sets the shape of the inner profile in the models of Del Popolo (2009) where more massive halos are predicted to have less angular momentum resulting in steeper profiles. It can be seen from Table 5.2 that the spin of the CDM halo decreases as the mass scale increases, consistent with this idea.

The CDM halo spin parameter is 26% higher at the small mass scale compared to the large while the WDM halos vary by $\lesssim 10\%$ which may be why the WDM profiles are very similar. However, the WDM spin parameters are higher than the CDM halos at all scales yet they have steeper profiles than CDM so this is not the entire answer. The inner profiles are shallower in WDM in agreement with the models of Williams et al. (2004) and Viñas et al. (2012). It is important to emphasize that the differences between WDM and CDM density profiles diminish as the halo
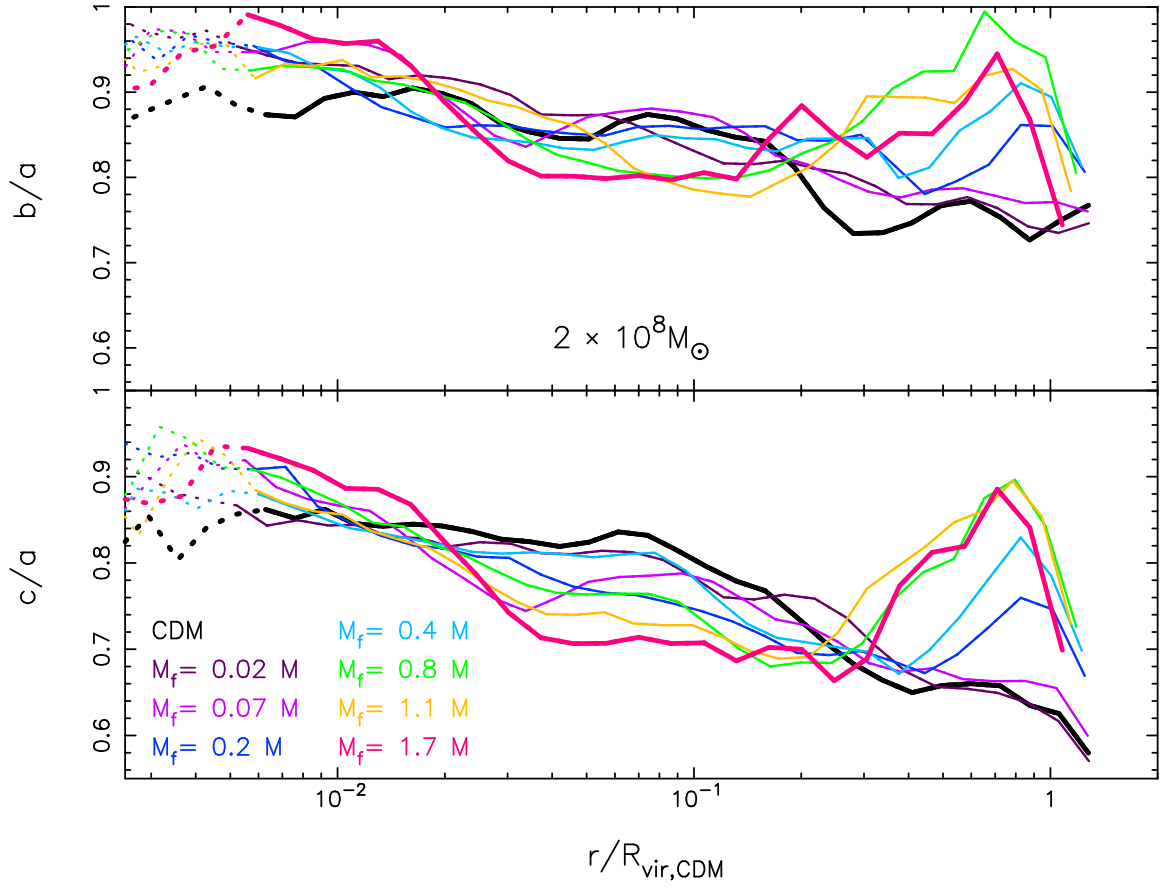
Figure 5.5: Axial ratio profiles of the small mass simulations of Halo A. The CDM and 4 keV ($M_f = 1.7M$) profiles are plotted in bold for clarity. The halo is more spherical in the inner and outer regions and less spherical in the intermediate regions in WDM.

mass increases due to the steepening of the CDM profile. This observation may explain why previous works have not clearly identified the prominent features and trends in the profile shapes found in this work.

In Figure 5.7 the logarithmic slope of the density profiles is compared across the mass scales. The large mass CDM halo profile is seen to be steeper than the medium and small mass halos for $r < 0.3R_{vir}$ and reaches the NFW value of -1 at a smaller radius (given by the short gray lines). However, the differences are less than predicted by the model of undigested subhalo cores of Subramanian et al. (2000) but in agreement with the predictions of Del Popolo (2010) whose models give an inner slope mass dependence due to angular momentum.

Unlike the CDM profiles the slopes in the WDM cosmologies are nearly identical across mass scales. The WDM profiles are steeper than CDM for $r < 0.1R_{vir}$ and achieve -1 at smaller radii, although this scale moves outward as the filtering scale gets larger. The inner profiles quickly become softer than CDM at $r \lesssim 0.01R_{vir}$ but none of the profiles in any cosmology show signs of approaching an asymptotic value.

5.3.2 Internal Kinematics

Figure 5.8 shows the profiles of σ^3 for the small mass simulations of Halo A, where σ is the local 3D velocity dispersion. Similar to the density profiles, the dispersions are greater in the inner WDM halos compared to CDM and show a correlation with the filtering scale, growing larger and extending to greater radii
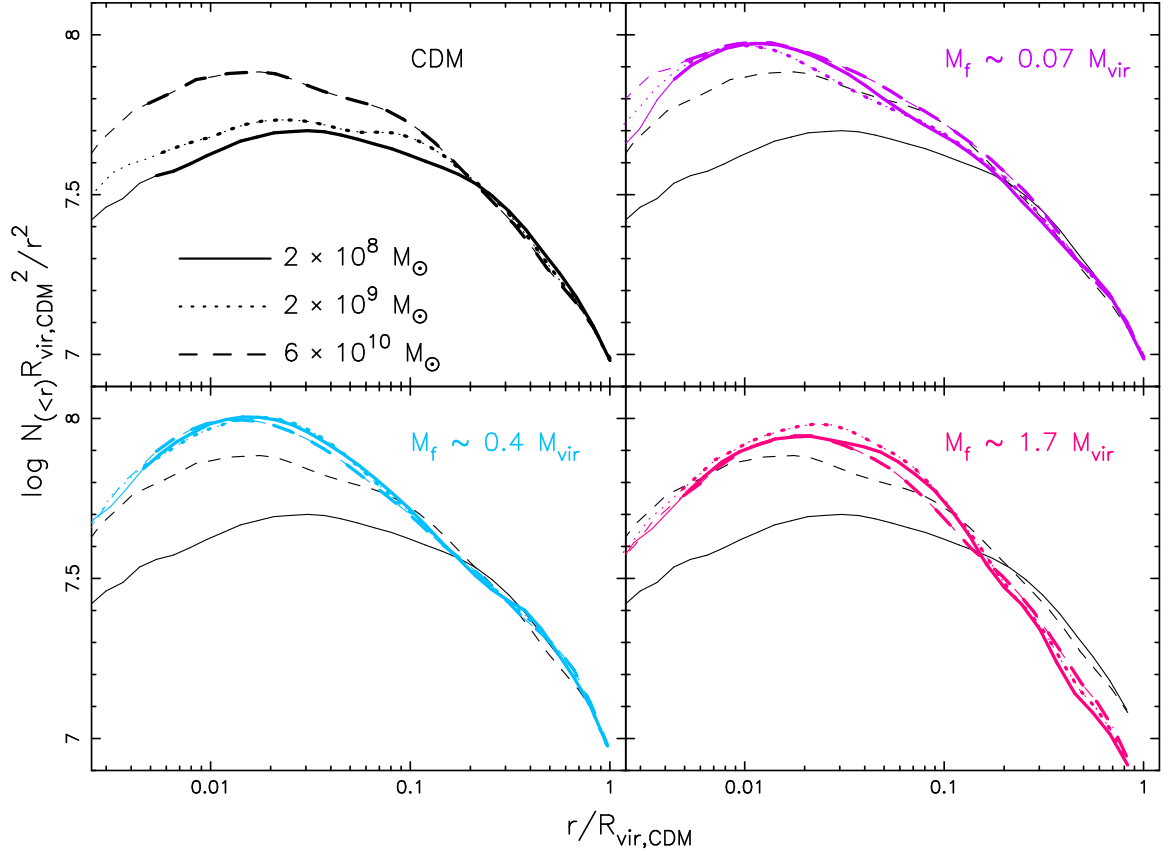
Figure 5.6: Comparison of the cumulative mass profiles of Halo A at the normalization times of the three mass scales when the halos have grown to $\sim 10^7$ particles. The small, medium, and large mass halos are plotted with the solid, dotted, and dashed lines, respectively. The profiles are given by the number of enclosed simulation particles and the radial coordinates have been normalized by the CDM virial radii. The WDM profiles are plotted against the small and large mass CDM profiles for comparison.
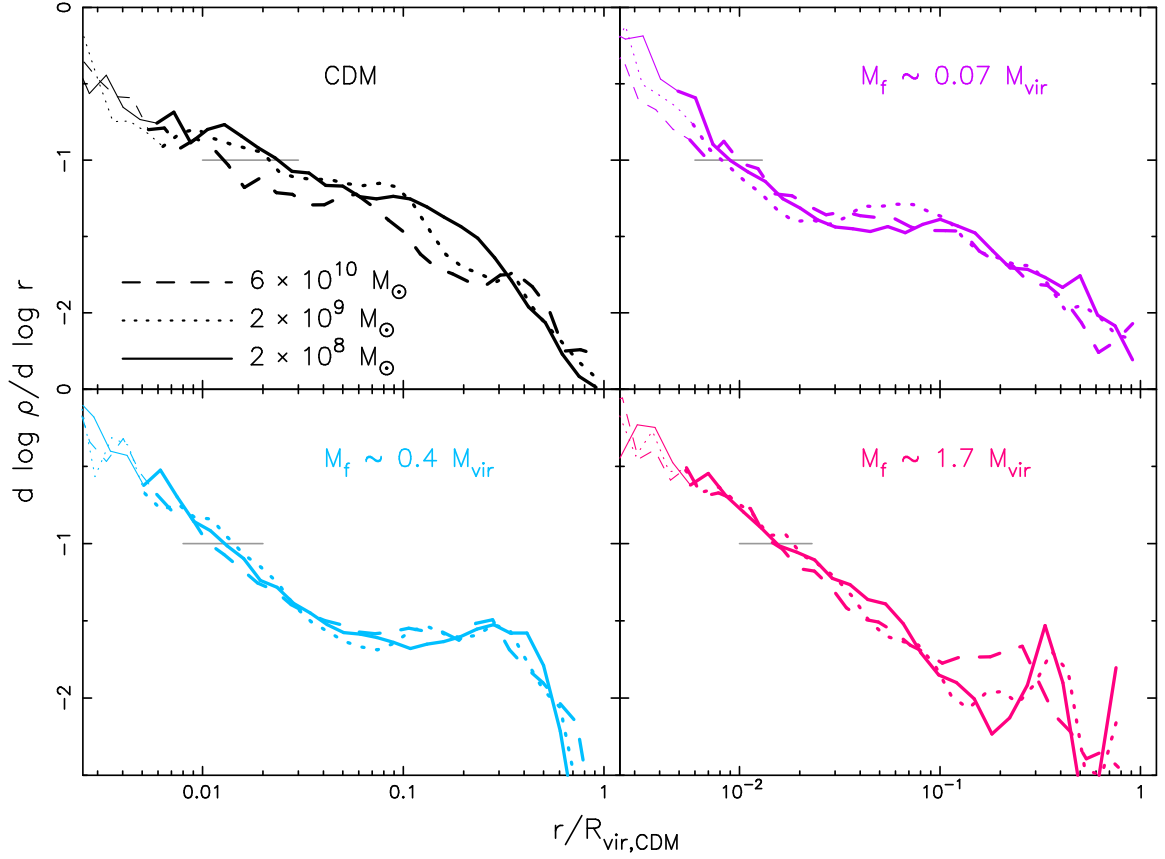
Figure 5.7: Comparison of the slope of the density profiles of Halo A across the three mass scales at the normalization times. The small, medium, and large mass simulations are plotted with the solid, dotted, and dashed lines, respectively. The radial coordinates have been normalized by the CDM halo virial radii. Short gray lines indicate where the log slope is -1 in all cosmologies. The CDM halo is steeper at the large mass scale than the small scale. The WDM halos are generally steeper than the CDM except at $r < 0.01 R_{vir}$.
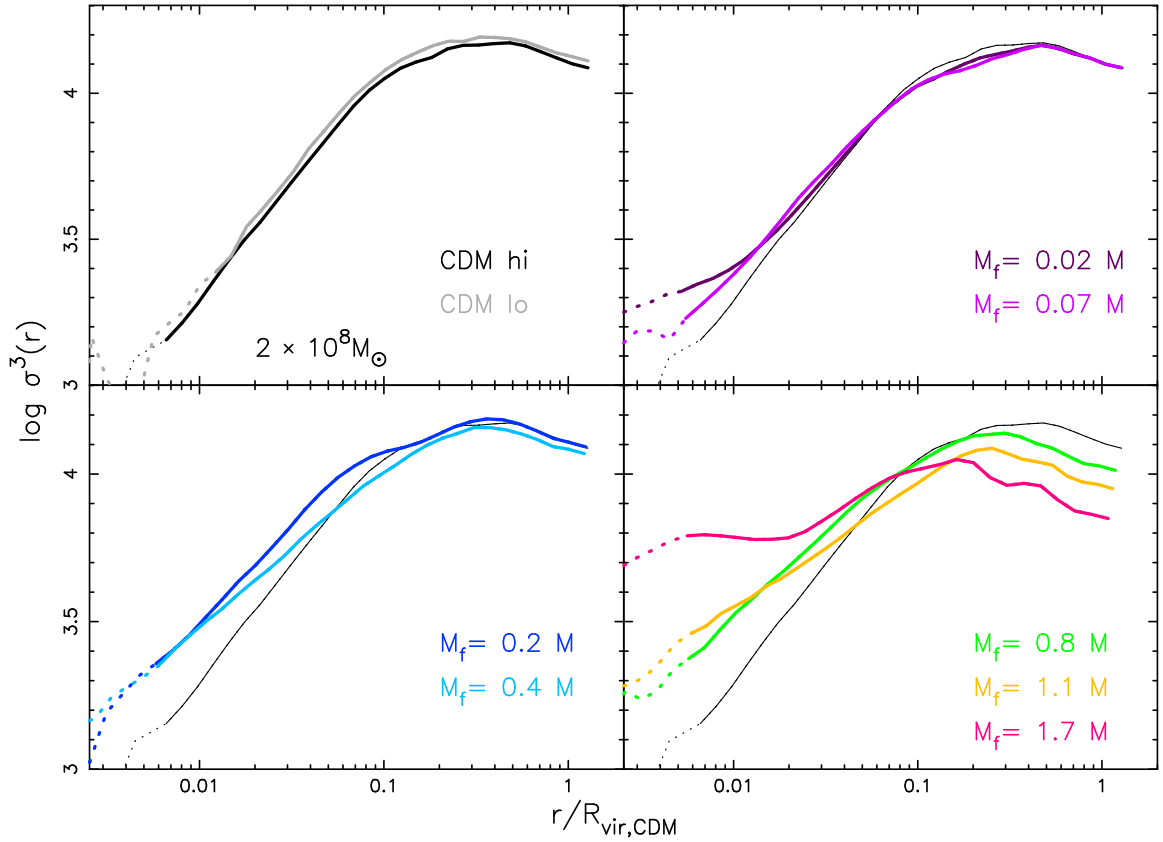
Figure 5.8: Velocity dispersion profiles of the small mass simulations of Halo A. WDM simulations have been grouped and plotted against the CDM profile for clarity.

as the cosmology becomes warmer and the filtering scale increases. This can be understood as a consequence of the increased mass in the WDM cores. As the mass in the core grows the dispersion must get larger to stay in virial equilibrium against the deeper potential well.

To examine the phase space density profiles of Halo A I adopt $\alpha = -1.875$ and fit the phase space density profiles of each CDM halo to the form, $Q_{fit} = Ar^{\alpha}$. Schmidt et al. (2008) have questioned if Q is a true universal profile and find

other choices for the velocity dispersion, such as different weights to the radial and tangential components, and different values of the parameter α can provide equally good fits. I am interested in the differences between the CDM and WDM haloes so the concern is merely adopting the same law for all cosmologies, not which law provides the best fit. An examination of alternative phase space density definitions did not change the results.

Simply for illustrative purposes, I show Q normalized to a power law fit Q_{fit}. I calculate the deviation, $\tilde{Q} = Q_{sim}/Q_{fit}$, using the CDM Q_{fit} for the WDM simulations. Figure 5.9 shows the deviations from power law for Halo A in all cosmologies for all three mass scales. A maximum is seen in the phase space density deviation in the inner regions of the WDM halos. Along the top axis of each plot are ticks marking the location of $0.037R_f$ in each WDM cosmology. This scaling was empirically determined but marks the location of the peak remarkably well indicating the deviations scale with the filtering scale.

Interestingly, a drop in the inner profile of the CDM halos is seen that becomes more pronounced as the halo mass decreases. This also agrees with the models of Del Popolo (2010) where he argued for a dependence of the Q profile on halo mass.

A useful metric of the particle orbits is the velocity anisotropy parameter given by:

$$\beta(r) = 1 - \frac{\sigma_\theta^2 + \sigma_\phi^2}{2\sigma_r^2},$$

(5.6)

where σ_θ^2 and σ_ϕ^2 are the angular velocity dispersions and σ_r^2 is the radial velocity dispersion. For purely radial orbits, $\beta = 1$, while isotropic particle motions give
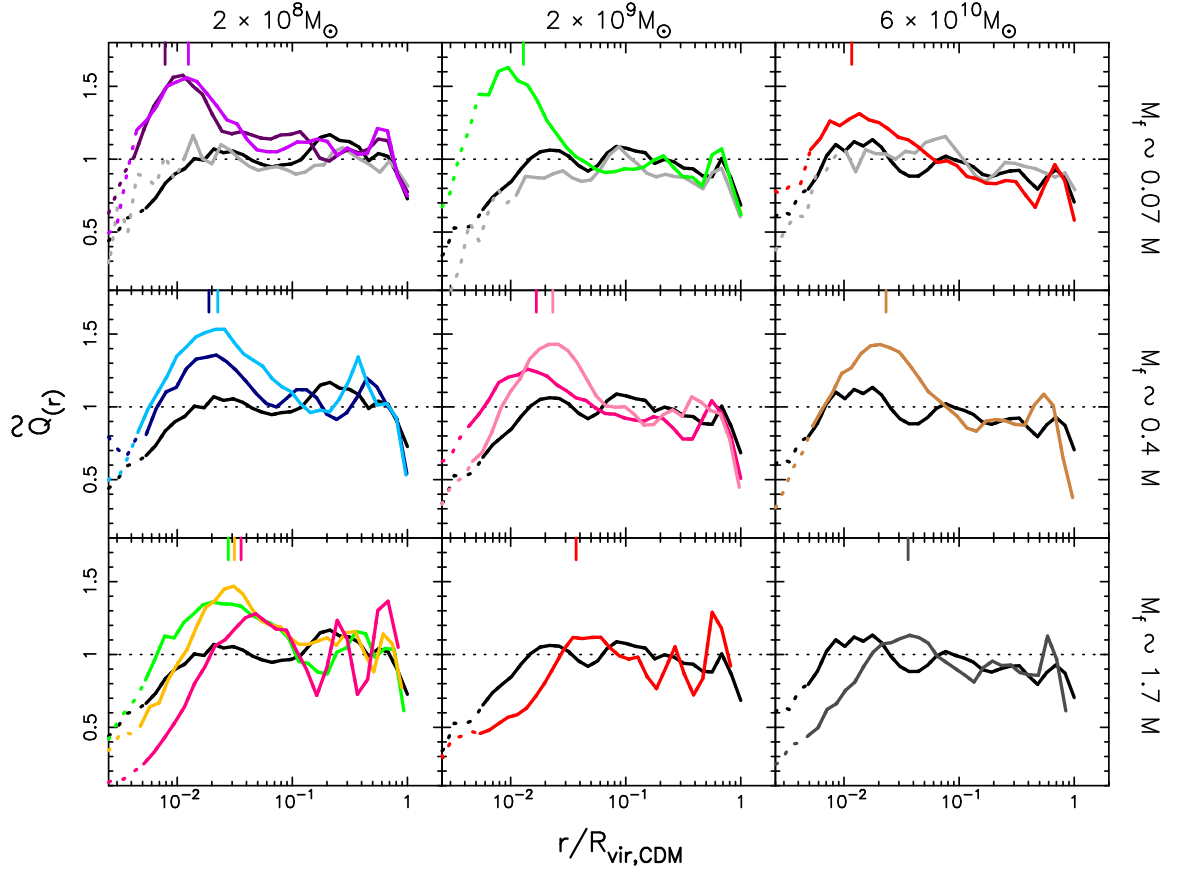
Figure 5.9: Deviations from power-law behavior in the phase space density profiles of the simulations of Halo A. The simulations are grouped by mass scale: small, medium, and large from left to right, and by relation of filtering mass to halo mass with the cosmology growing warmer from top to bottom. Deviations from power-law are seen in the inner WDM halos that reach a peak at $\sim 4\%$ of the filtering length (colored ticks along the top of each plot).

$\beta = 0$. At the halo outskirts $\beta \rightarrow 1$ where freshly accreted material is still falling inward while in the core of a relaxed halo $\beta \rightarrow 0$. In practice the anisotropy parameter is seldom exactly zero in the inner regions since simulated halos are generally not spherically symmetric.

Figure 5.10 shows the velocity anisotropy profiles of Halo A in all simulations. There is a radial bias in the CDM particle orbits at $r > 0.1R_{vir}$ while particles inside this scale are well isotropized. The WDM profiles are generally similar to CDM, although in the warmest cosmologies (bottom row) the halos have radial bias extending deeper into the inner halo than in the other cosmologies. This may not be due to an incomplete isotropization of the particle velocities but simply to the increased triaxiality seen at these radii (Figure 5.5). What is clear is the lack of any feature at the location of the peak deviations in the Q profile making it apparent the physical processes that created the increased mass in the WDM cores do not leave an imprint on the isotropy of particle velocities after virialization.

5.3.3   Convergence Tests

Figure 5.11 shows the profiles of Halo A in the high and low resolution simulations of Halo A and the test simulations initiated from a higher redshift. Excellent agreement is seen across resolutions in both CDM and WDM and from the simulations started from higher redshift. The convergence criterion of Power et al. (2003) appears to be not only valid but perhaps overly conservative in measuring the convergence radii of these simulations.
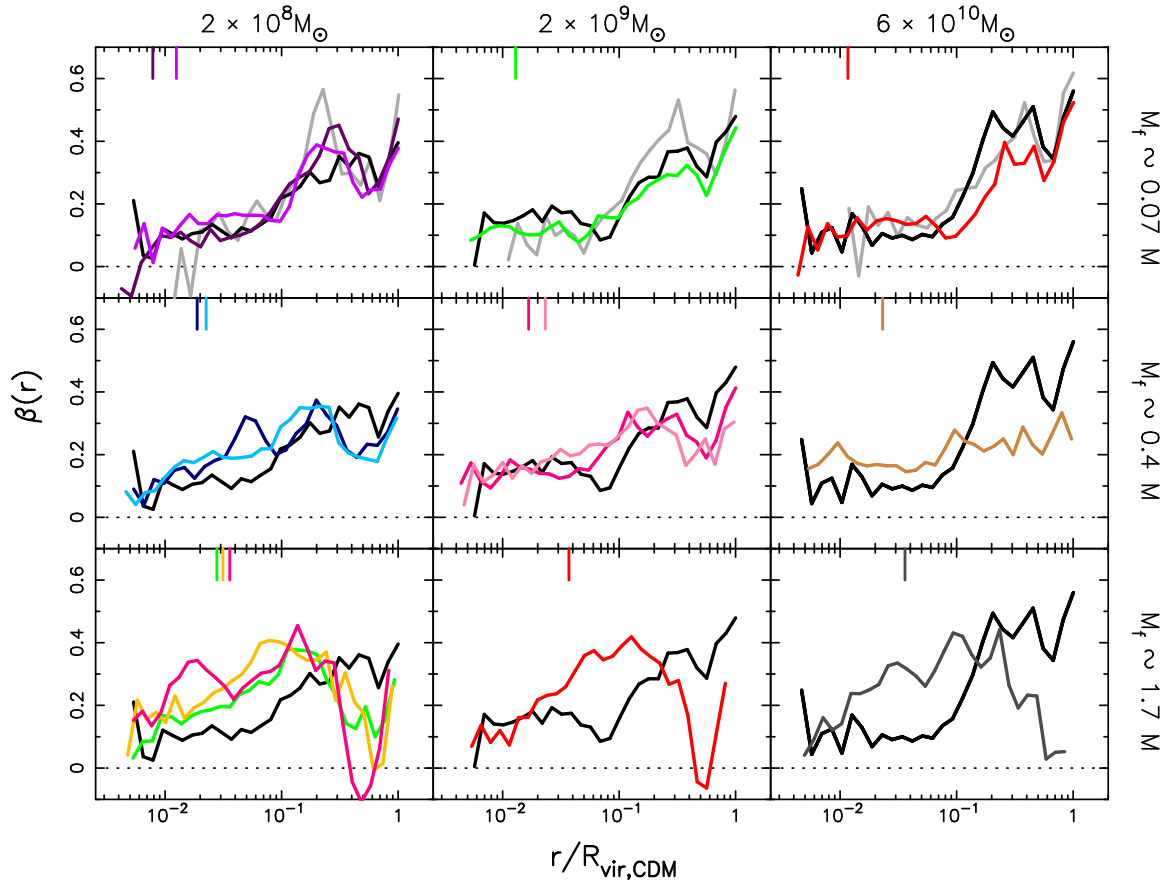
Figure 5.10: Velocity anisotropy profiles of the simulations of Halo A. The simulations are grouped by mass scale: small, medium, and large from left to right, and by relation of filtering mass to halo mass with the cosmology growing warmer from top to bottom. No features are seen at the peaks of the phase space density profile deviations marked by the colored ticks.

Simulations with truncated power spectra are known to produce numerically artificial small mass halos along the filaments of collapsed density perturbations (Wang and White 2007) whose size and separation are dependent on the mass resolution. Figure 5.11 also shows the results are not due to these spurious halos since a dependence on the mass resolution would be expected to reflect on the shape and location of the features in the WDM profiles.

5.4   Results II - Testing Cosmic Variance

In this section I examine the effects of truncated power spectra on a larger sample of halos. I examine halos in the simulations with increased refinement volume around Halo A sampled with low mass resolution. These simulations were run for the large and small mass scales with a similar ratio of the WDM filtering scale to halo scale in both volumes. I compare the same halos across cosmologies and also compare the same CDM halos at different mass scales.

The 15 largest halos are labeled A-O and their mass growth histories are plotted in Figure 5.12. The dashed gray lines indicate the WDM filtering mass in the large box. The largest halos after entering the slow growth phase (A-E and H) have masses greater than the filtering mass. These halos are also where the WDM mass catches up with the CDM mass while both halos are still in the fast growth phase, with both halos growing at similar rates thereafter. Halos F, N, and O are halos where formation begins later in WDM but the halo mass has just caught up to the CDM by the end of the simulations. In the other halos WDM halo formation
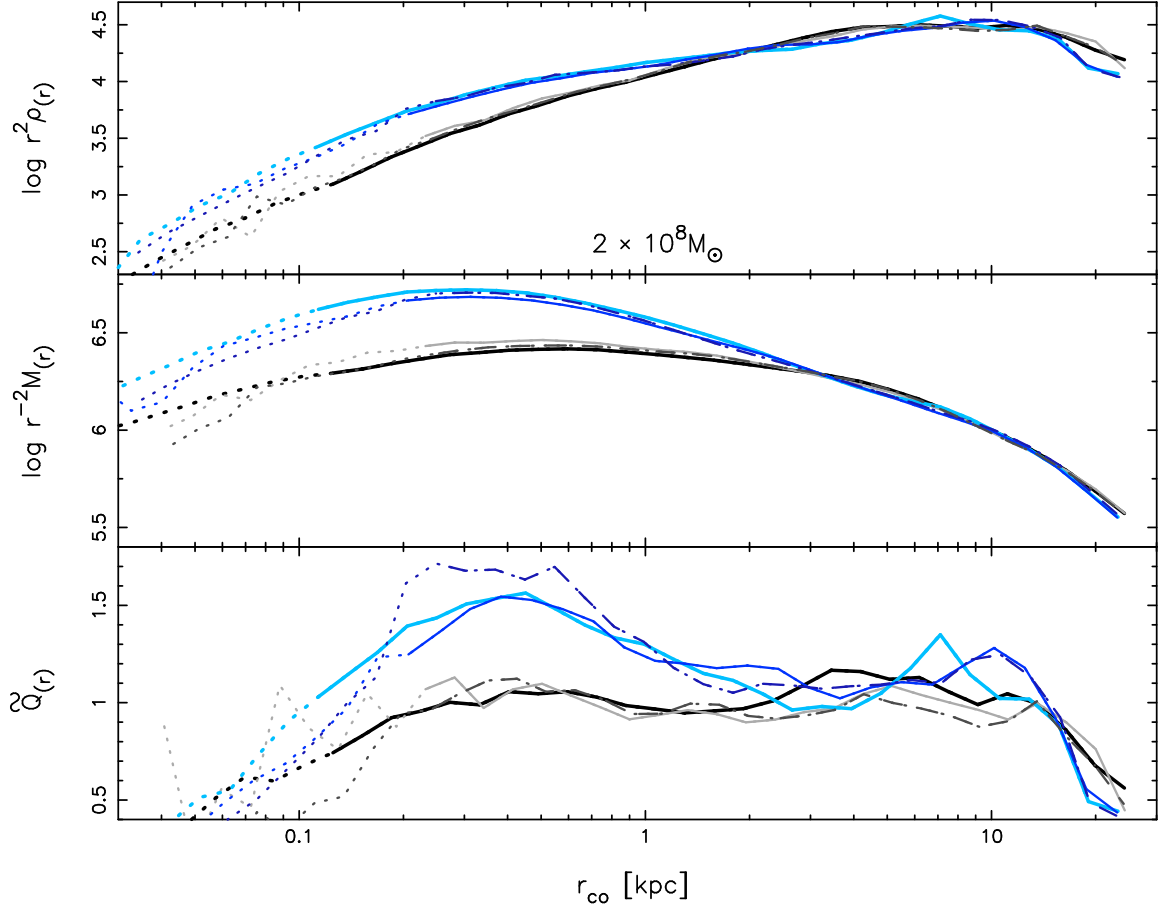
Figure 5.11: Comparison of the high and low resolution small mass simulations of Halo A. The high and low resolution CDM simulations are plotted in black and gray, respectively, the high and low 6 keV simulations in light and dark blue. The dashed lines are the low resolution 6 keV and CDM simulations started from a higher redshift. Profiles are plotted with solid lines where they satisfy the convergence criterion of Power et al. (2003) and are extended to 3ϵ with dotted lines. Consistent results are seen across simulations demonstrating the results are not affected by the mass resolution or starting redshift.

was delayed too long to catch up to the CDM halo before the end of the fast growth phase.

Figure 5.13 shows cumulative mass profiles for halos A-O at the normalization times when these halos are composed of $> 10^5$ particles in CDM and $> 3 \times 10^4$ in WDM. This is about the same resolution as the simulations of Ricotti (2003) but the volume sampled here is smaller and I examine the halo profiles individually rather than averaging. Halos J, L, and M have virial ratios, $2K/|U| - 1 > 0.8$, at these times due to recent or ongoing merging. I consider the profiles of these halos to be unreliable and focus the analysis on the other 12.

I first compare the CDM halos at large and small mass scales I note differences in nine of the 12 halos: A-G, I, and N. The difference is largely in the inner profile, $< 0.1R_{vir}$, with the larger halos being more dense. The exception is halo C where the small halo is denser over most of the profile.

Comparing the WDM profiles to the CDM, increased mass is seen in the inner WDM halos at one or both mass scales for six halos: A-E and H. Halo A is seen to be the most extreme with 2.5 times more mass at the convergence radius at the small mass scale while the others are less than a factor of 2. Halo F is unique in that it has nearly identical inner profiles while in the rest the WDM profiles are below the CDM.

The halos with dense cores in WDM are the ones where the halo mass catches up to the CDM halo early then evolves at the same rate afterwards. This is consistent with the view that if the WDM catches the CDM before the end of the fast growing phase the overdense core forms. Furthermore, halos A-F and H have masses equal
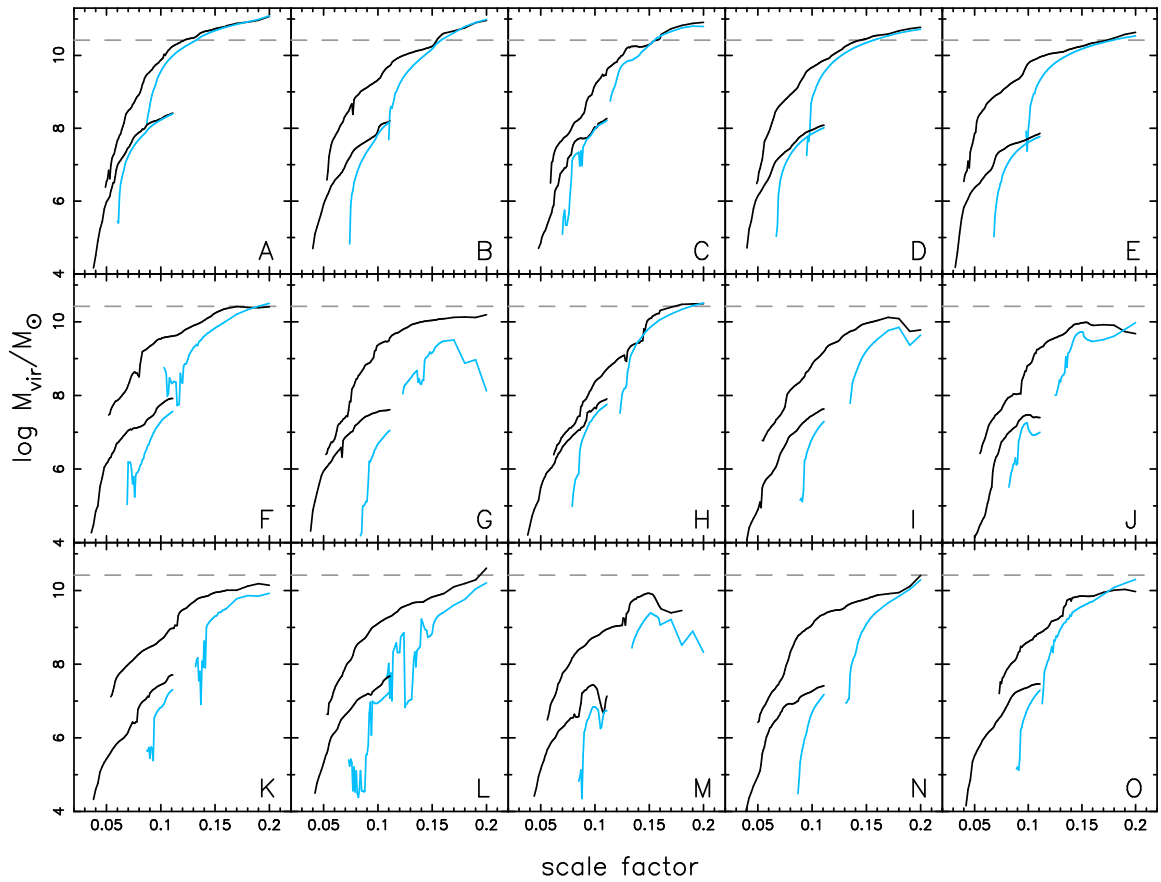
Figure 5.12: Growth in mass for the 15 largest halos in the low resolution, large refinement volume simulations at the small and large mass scales. CDM simulations are plotted in black and WDM in blue where the ratio of filtering scale to mass scale was the same for both simulation volumes. Gray dashed lines indicate the WDM filtering mass at the large mass scale.
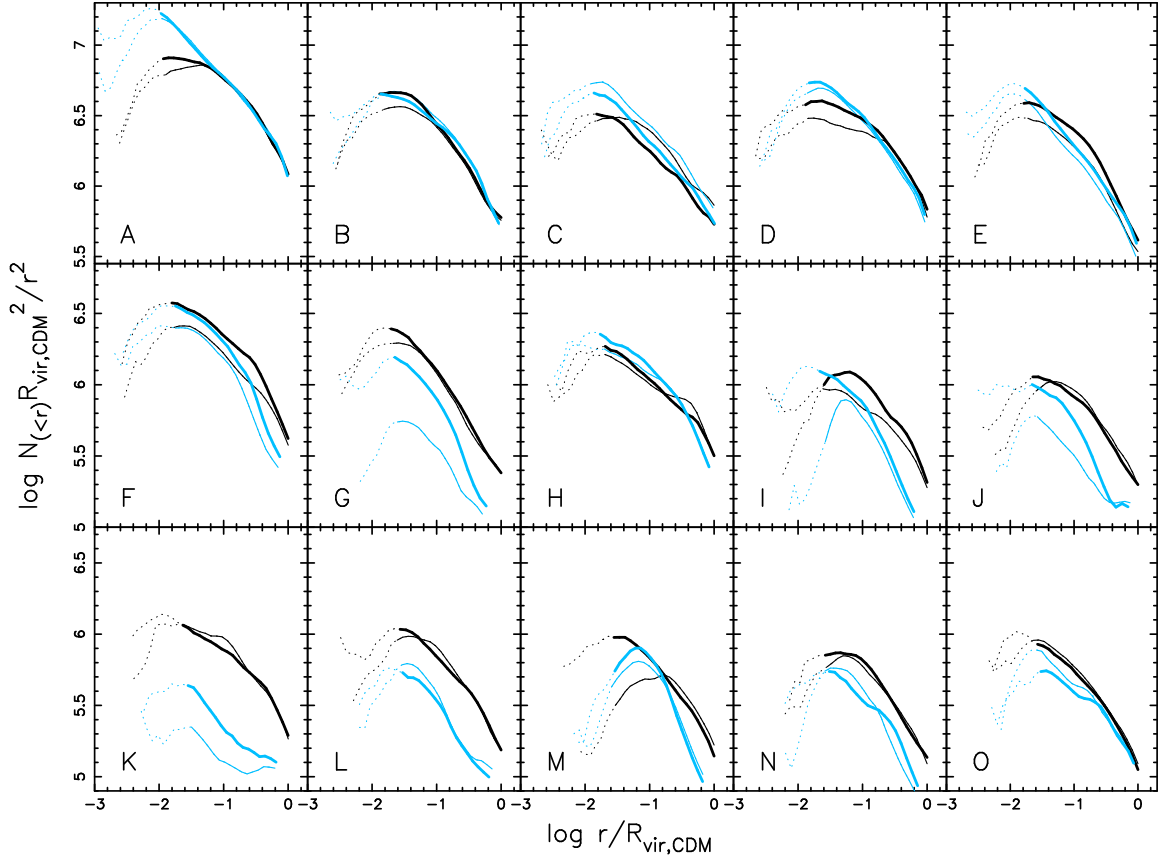
Figure 5.13: Cumulative mass profiles for the 15 largest halos in the low resolution, large refinement volume simulations at $a = 0.1$ and $a = 0.155$ at the small (thin lines) and large mass scales (thick lines), respectively. The CDM simulations are plotted in black and the WDM in blue. For comparing across mass scales the profiles are given in number of enclosed simulation particles and the radial coordinates have been normalized by the halo virial radii.

to or greater than the filtering mass before they enter the slow growth phase while the other halos are well below the filtering scale when their growth begins to slow.

I examine this further by running individual high resolution simulations of select halos in a similar manner as Halo A. Halos B-E were chosen for resimulation because they show dense cores in WDM. Halo F was chosen because it shows nearly identical profiles in CDM and WDM and because halo G was nearby such that one refinement volume could sample both halos. I ran the simulations at the large mass scale for CDM and 2 keV to reduce the filtering mass for halo G and guarantee the WDM halo formation doesn't start too late. Since these simulations were only conducted at one mass scale I compare the halos at the end of the simulations, $a = 0.16$, instead of the normalization time. The halos are composed of $2.4 - 10.8$ million particles at this time and their properties are listed in Table 5.3. Figure 5.14 shows the enclosed mass profiles for halos A-G. The profile of halo F again shows almost no difference in CDM and WDM. Curiously, halo F also has a significantly higher spin than the other halos. Although halo C shows a very dense WDM core it also has a large amount of substructure in CDM and hence may not be fully relaxed. I judge halo C to be inconclusive and conclude five out of seven halos show increased central mass in WDM. Note that the difference bewteen CDM and WDM is not as evident at large mass scales as for the small scales.
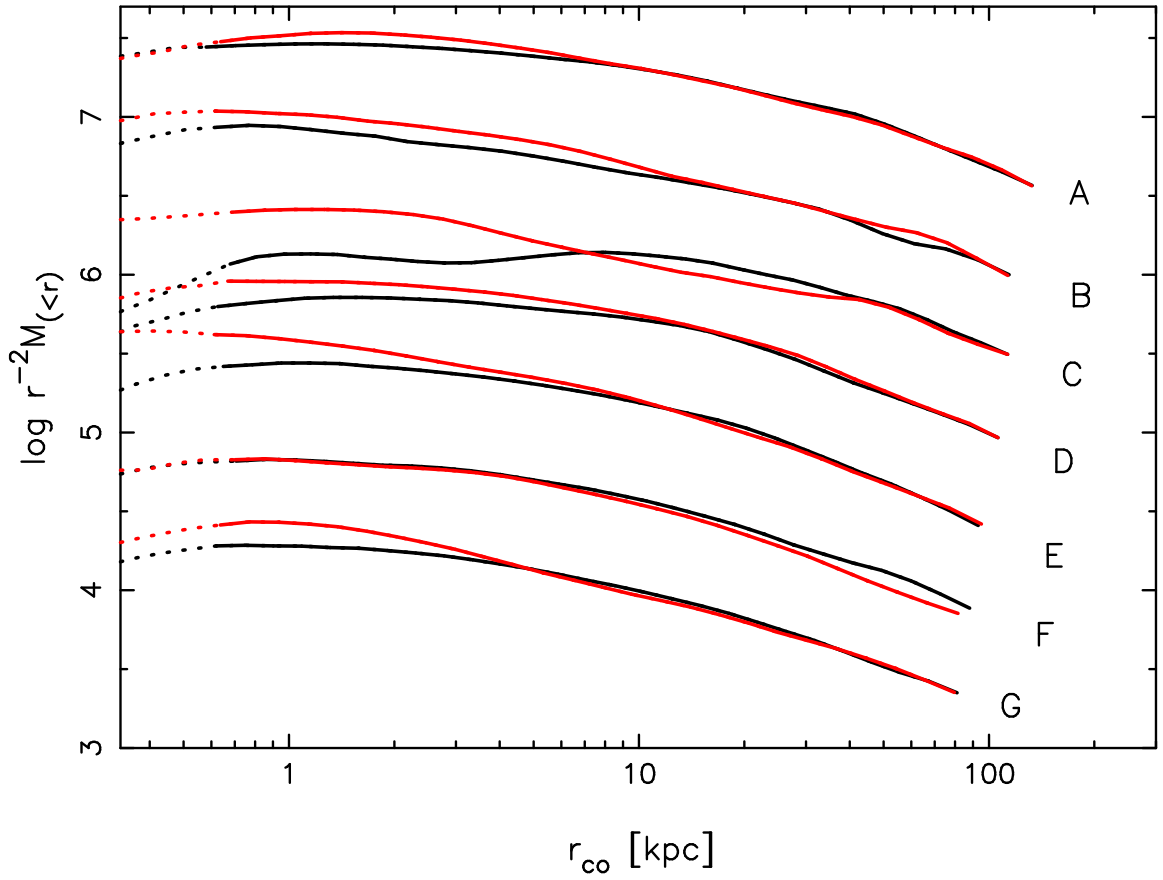
Figure 5.14: Cumulative mass profiles of all seven halos in the high resolution, large mass scale simulations at $a = 0.16$. The mass profiles have been multiplied by r^{-2} to reduce the dynamic range and offset downward in intervals of 0.5 dex for clarity.

Table 5.3: Properties of high resolution simulated halos A-G.

Cosmo	a	M_{vir}	λ'	x_{off}	$\frac{2K}{|U|} - 1$
		$[10^8 M_\odot]$	$[10^{-2}]$	$[R_{vir}]$	
(1)	(2)	(3)	(4)	(5)	(6)
Halos A-G - Large Box					
A CDM	0.16	648.777	2.11	0.09	0.38
A 2 keV	0.16	642.201	2.83	0.06	0.38
B CDM	0.16	411.910	1.32	0.01	0.48
B 2 keV	0.16	400.569	1.56	0.01	0.44
C CDM	0.16	425.037	0.96	0.10	0.49
C 2 keV	0.16	413.263	1.34	0.04	0.43
D CDM	0.16	329.871	2.01	0.06	0.28
D 2 keV	0.16	330.351	1.47	0.03	0.28
E CDM	0.16	223.489	1.00	0.05	0.27
E 2 keV	0.16	237.997	0.94	0.05	0.24
F CDM	0.16	188.720	7.73	0.08	0.55
F 2 keV	0.16	149.931	6.53	0.06	0.62
G CDM	0.16	147.183	3.01	0.05	0.51
G 2 keV	0.16	142.662	3.16	0.03	0.54

5.5 Origin of the Core

The simulations in this work have shown an increased mass in the inner $0.1R_{vir}$ is common for halos near the filtering mass in WDM cosmologies. This region will be referred to as the core although the scale where the halos diverge from their CDM counterparts is dependent on the filtering scale. In this section I examine the formation of the core, its stability, and investigate clues to its origin.

I begin by examining the core of Halo A. Here, I define the core radius for each mass scale as 3.1% of the CDM halo's virial radius at the normalization times. This radius was held constant in proper length and the number of particles within the

core was calculated for all cosmologies at all times a halo progenitor was identified. Figure 5.15 shows the growth in the number of core particles in all large mass scale simulations (similar results are seen for the medium and small mass scales). To show the average growth in the number of core particles I fit polynomials up to seventh order to the simulation data and plot these as thick lines in Figure 5.15. It is clear the core forms quickly in WDM while core growth is more gradual in CDM. The number of core particles remain approximately constant after formation in both CDM and WDM. The epoch of WDM core formation occurs shortly after the halo virial mass catches up to the CDM halo and the accretion rate slows to the CDM rate. For example, in the 1.1 keV ($M_f \sim 0.4M$) large mass scale simulation the core forms at $a \sim 0.11$, while Figure 5.2 shows the accretion rate slows to about the CDM rate at $a = 0.1$. I conclude the core forms as the fast growth phase ends and the halo transitions to the slow accretion phase.

The stability of the core after its formation is examined next. Figure 5.16 shows the deviations from power law in the phase-space density profiles of the medium mass scale simulations of Halo A at multiple epochs between $a = 0.105 - 0.121$. This is equivalent to a timescale of $\sim 1.4 \times 10^8$ yr. The mass within $r_{prop} = 0.5$ kpc is $\approx 10^8 M_\odot$, this timescale therefore spans > 6 dynamical times. The profiles show a scatter of $\sim 20\%$ but the scatter is not correlated with time demonstrating the inner halo is stable over this timescale.

The accretion rate, $\dot{M} \equiv d \log M / d \log a$, for these epochs is < 6 for the 3 keV cosmology and < 4 in CDM, 5 keV, and 4 keV. The 2 keV halo enters the slow growth phase later than the other cosmologies and $\tilde{Q}$ is only plotted at epochs $a > 0.115$
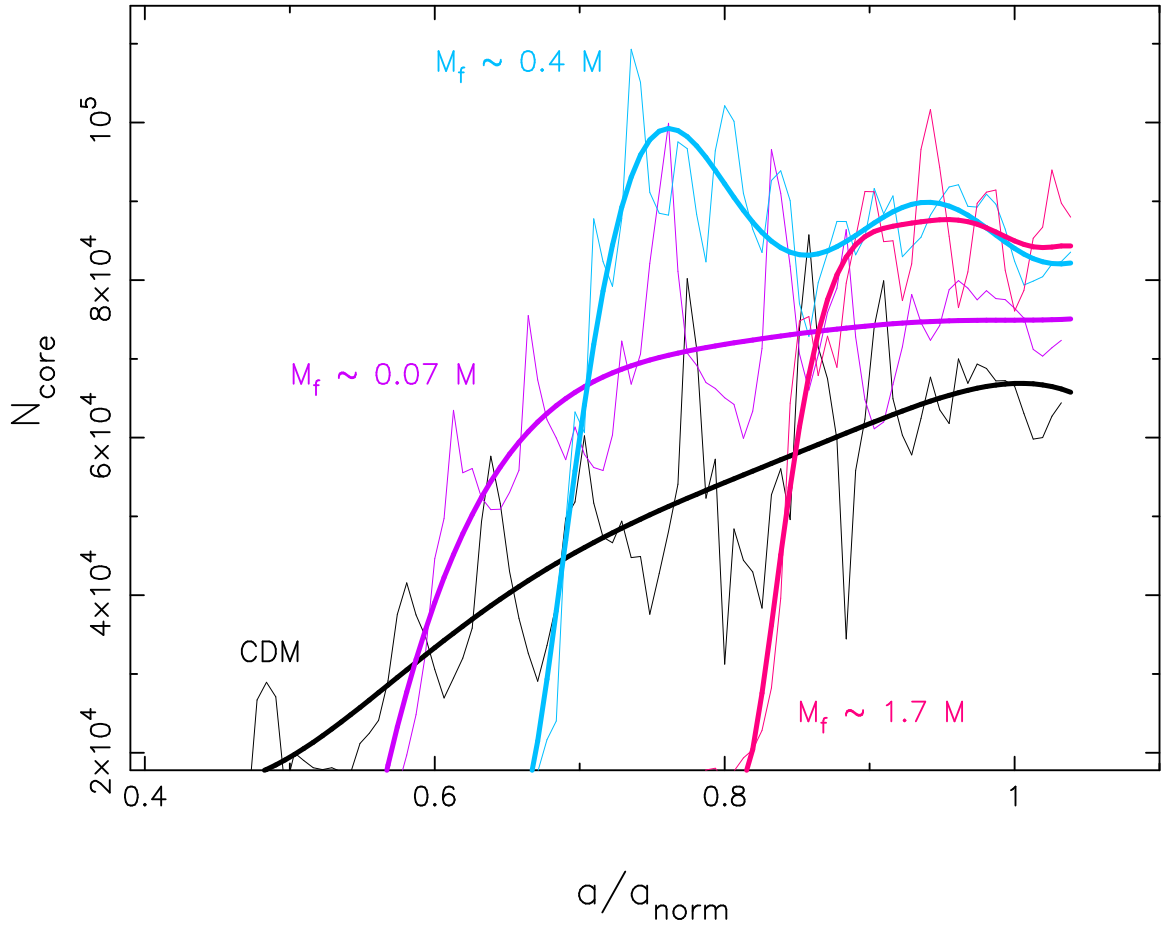
Figure 5.15: Evolution of the number of particles within the core in the high resolution, large mass scale simulations of Halo A. The simulation data is plotted as the thin lines and polynomial fits as thick lines. The core radius was held fixed in proper length at 620 pc. The scale factors have been normalized by a_{norm}.

in Figure 5.16 when $\dot{M} < 6$ for this simulation. Zhao et al. (2003b) found that halo growth in the fast phase is $M \propto H^{-4}$, and in the slow phase $M \propto H^{-1}$. In the matter dominated era the Hubble parameter depends on scale factor as $H \propto a^{-3/2}$. Therefore, the mass growth rate is $\dot{M} = 6$ in the fast phase and $\dot{M} = 3/2$ in the slow phase. I found the Q profiles are stable after the accretion rate drops $\lesssim 6$, which agrees with the core being formed at the end of the fast era. I conclude the structural and dynamical features in the inner WDM profiles are stable in the slow growth phase.

Having established when the core forms and shown it is stable after formation, I proceed to look for clues to the physical processes responsible for its creation. Figure 5.17 shows the core particles of Halo A in the small mass scale simulations at $a = 0.05$, well before core formation. The images are centered on the particles' center of mass. As the cosmology gets warmer the core particles become more symmetrically distributed around the center of mass. As noted by Busha et al. (2007), the filtered power spectra causes what were multiple clumps in CDM to become one collapsing clump in WDM.

I also examine the core particles of the high resolution, large mass scale simulations of halos B-G. For these halos the core radius is defined as 5.7 kpc in comoving units at $a = 0.16$. Figure 5.18 shows the core particles at $a = 0.075$. Halo F has minimal differences between CDM and WDM profiles and also appears to have the least differences between particle distributions. Its growth is least affected by the power spectrum cutoff. Halo F was also seen to have a much higher spin parameter than the other halos at the end of the simulation.
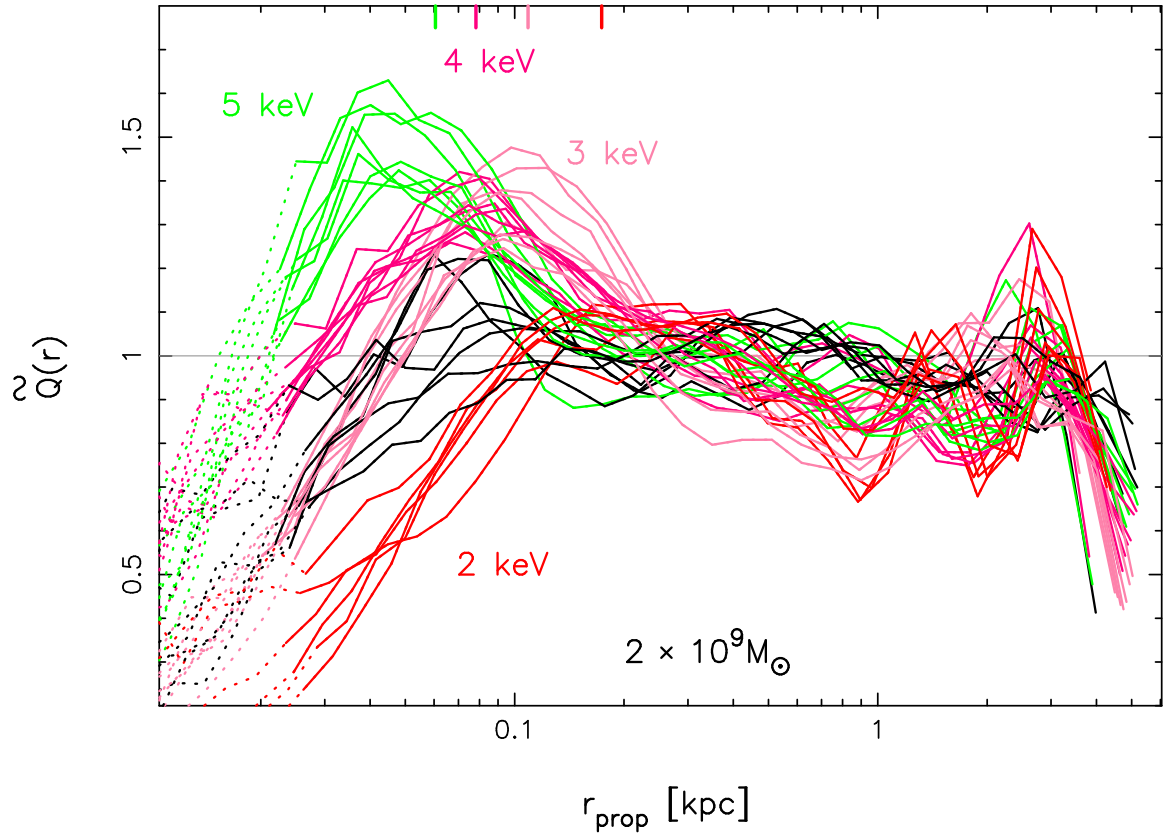
Figure 5.16: $\tilde{Q}$ profiles in proper radius for the medium mass scale simulations of Halo A for epochs $a = 0.105 - 0.121$. The scatter in the profiles is not correlated with epoch.
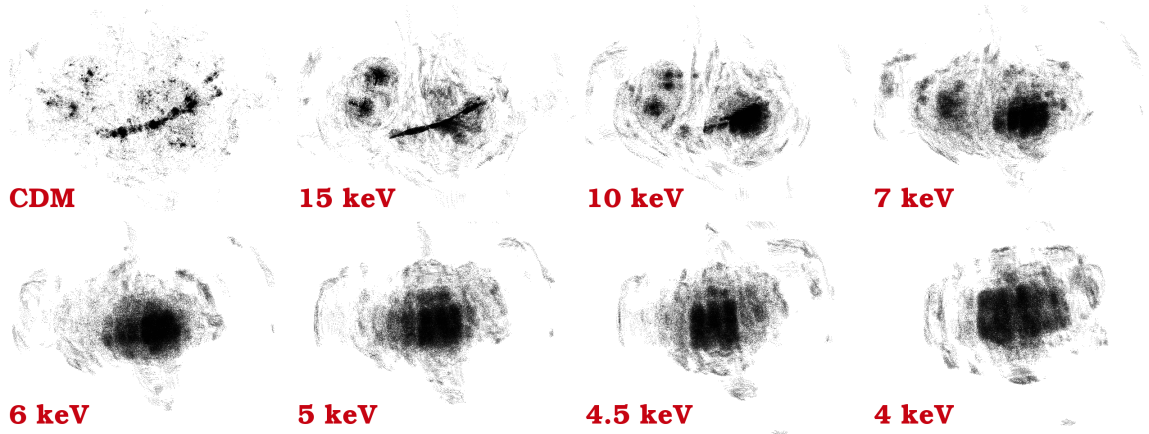
Figure 5.17: Positions at $a = 0.05$ of core particles in all cosmologies of the high resolution small mass scale simulations of Halo A. Images are centered on the center of mass of core particles.
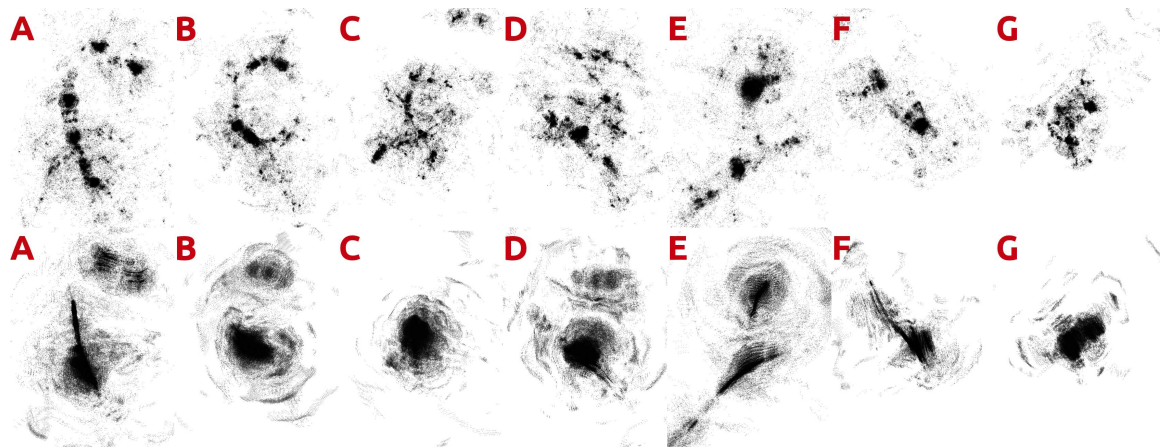
Figure 5.18: Positions at $a = 0.075$ of particles within a proper core radius of 914 pc at $a = 0.16$ in all seven halos of the high resolution, large mass scale simulations. CDM is shown in the top row, 2 keV WDM in the bottom row. Images are centered on the center of mass.

The evidence points toward angular momentum playing an important part in determining the structure of the core. The importance of angular momentum for the shape of the inner profile has been emphasized by a number of studies (Huss et al. 1999a,b; Hiotelis 2002; Ascasibar et al. 2004; Lu et al. 2006). Purely radial orbits give a steep inner profile, $\rho \propto r^{-2.25}$ (Bertschinger 1985). As the amount of angular momentum is increased particles remain closer to their maximum orbital radii resulting in shallower density profiles. Angular momentum is dominated by the tangential component of the velocity dispersions which are acquired dynamically in both the CDM and WDM simulations since thermal velocities were not added to the WDM particles. Interactions with substructure and the global tidal field produce tangential components to the particle velocities. An alternative possibility is radial orbit instability (Belokurov et al. 2008). I speculate that during collapse the particles in CDM acquire more tangential velocity, either through interactions with other subclumps or violent relaxation occurring within the subclumps, while in WDM the particles collapse radially before acquiring tangential dispersions. After collapse, the virialization process isotropizes the particle velocities equally well in both CDM and WDM as seen from Figure 5.10. The higher accretion rates in the WDM fast growth phase may also play a role in generating the core as seen in the models of Lu et al. (2006).

5.6 Discussion

I found the inner structure of dark matter halos in cosmologies with truncated power spectra may deviate from their profiles in CDM with mass moving from the intermediate regions to the center. In this section I discuss how my work compares to previous studies.

It is well established that in WDM cosmologies halos below the truncation scale form later and have lower concentrations than CDM halos of similar size (Avila-Reese et al. 2001; Bode et al. 2001; Knebe et al. 2002). The free parameter r_s in the concentration definition is frequently taken to be the radius where the logarithmic slope is -2. From Figure 5.3 it is clear that r_s and thus the concentration parameter is minimally affected by the rearrangement of mass in the inner WDM halos, as expected for halos above the filtering mass.

Investigations of Milky Way satellites in $1-4$ keV WDM cosmologies have shown the maximum circular velocity decreases and the radius where this occurs increases for dwarf galaxy-sized halos (Lovell et al. 2012; Anderhalden et al. 2013; Polisensky and Ricotti 2014). Figure 5.19 shows the circular velocity profiles of the medium mass scale simulations of Halo A at the normalization time. It is clear the increased mass at the core has not affected the maximum circular velocity or its location to be in disagreement with the conclusions of other work.

My WDM halo profiles are similar to the profiles seen by Colín et al. (2008). They simulated five galactic-sized halos in WDM and fit NFW profiles. They found their halo profiles were steeper and denser in the inner region than NFW. However,
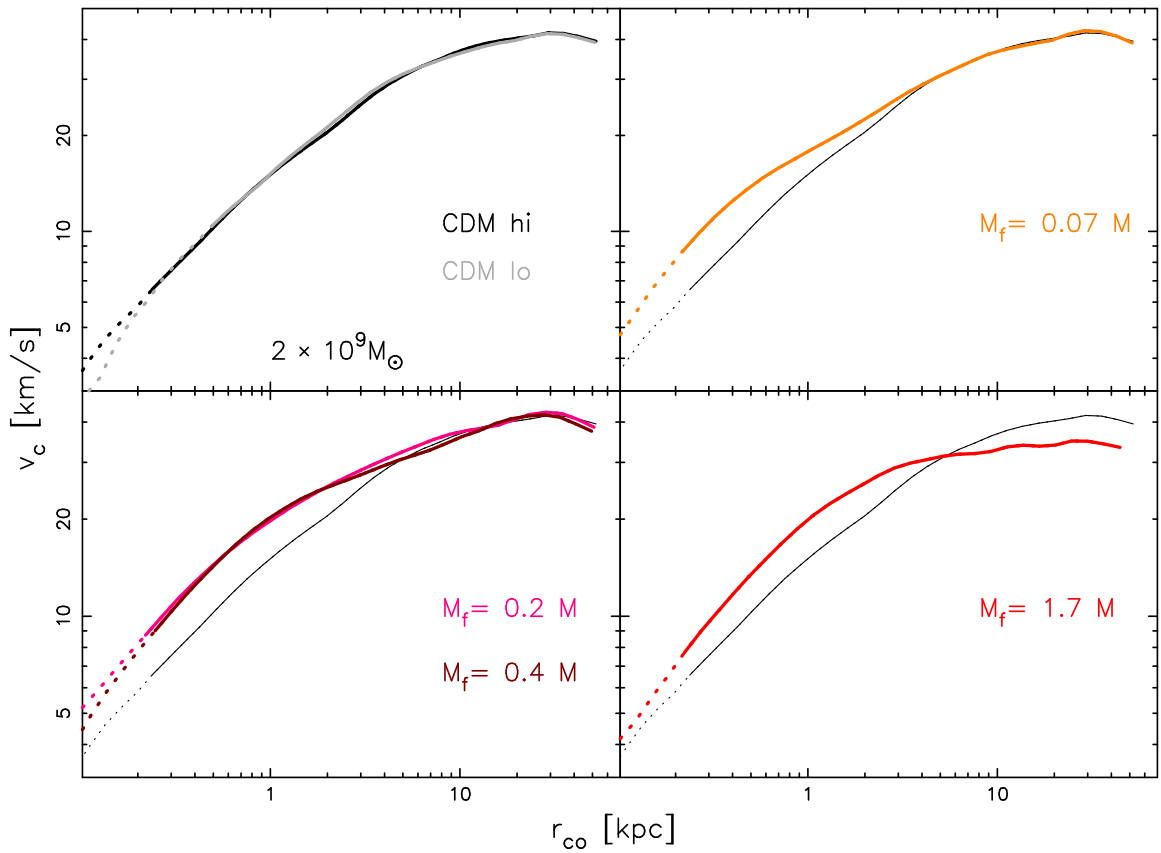
Figure 5.19: Circular velocity profiles of the medium mass scale simulations of Halo A. The WDM profiles have been grouped and plotted against the CDM profile for clarity.

only one of their halos had a corresponding CDM simulation and was seen to have less mass at the center than the CDM halo. This may be because for the transfer function they used the filtering mass is $M_f = 1.0 \times 10^{13} M_\odot$ while their 5 halos range $1.8 - 6.2 \times 10^{12} M_\odot$, well below the filtering mass. The simulations presented in Section 5.4 show halos below the filtering mass have lower core densities than in CDM.

My simulations also explain a feature seen in the HDM cluster simulations of Wang and White (2009). They stacked the $Q(r)$ profiles of their 20 most massive halos in both CDM and HDM and see a flattening in the inner $0.05R_{vir}$ of the HDM average profile (Figure 7 in Wang and White) similar to the flattening seen in the warmest simulations of Halo A.

My results seem to be in conflict with the work of Busha et al. (2007). They evolved their CDM and WDM simulations far into the future, until the scale factor $a = 100$. Past the current epoch ($a = 1$), the cosmological constant quickly dominates the density of the universe ($\Omega_\Lambda \to 1$) leading to exponential expansion. Halo accretion and structure growth essentially cease at $a \sim 3$. Thus, examining halo properties in the far future guarantees the halos have ample time to relax into their equilibrium states. Busha et al. find the average density profiles of halos in both cosmologies are well fit by the NFW form for $r > 0.05R_{vir}$ (although the outer slope is steeper due to the inflating universe, as noted by Ricotti 2003). They further examine the average density profiles for halos in mass ranges above, near, and below the filtering mass. They find all profiles are well fit by the NFW form for $r > 0.05R_{vir}$ with only lower concentrations below the filtering mass. However,

146

there are two things that complicate comparison of their simulations to mine. First is the difficulty due to the different epochs the halos are examined at. I examine my halos shortly after the end of the fast accretion phase when the inner profile is set but the outskirts are still growing while Busha et al. examine their halos well after all halo growth has stopped and R_{vir} has reached a maximum. Therefore, the effects I see in the inner halo will be at radii smaller than the convergence radius in their halos, $r < 0.05R_{vir}$. Also, their box sizes are larger than mine and they used a much greater filtering mass, $1.2 \times 10^{14} M_{\odot}$. In this work I have shown how even the density profiles of CDM halos have a dependence on mass with smaller differences between CDM and WDM profiles for larger halo masses, for a fixed ratio of the filtering mass to halo mass.

Finally, I comment on the effects of adding thermal velocities appropriate to the adopted WDM models to the simulation particles. Thermal WDM particles decouple with a finite fine-grain phase space density that imposes an upper limit on their density, resulting in soft cores in collapsed halos. The radius of this core depends on the mass of the WDM particle and the mass of the halo (Hogan and Dalcanton 2000). For the warmest cosmologies of Halo A the core radius is $\sim$ $4 \times 10^{-4} R_{vir}$ which agrees with the core sizes seen in the simulations of Macciò et al. (2012). The thermal core would be about the size of the adopted softening lengths, far below the scales where the WDM profiles deviate from the CDM profile.

5.7 Summary

I tested the claim that the virialization process erases all information about the initial conditions and produces universal mass density and phase space density profiles in gravitationally collapsed dark matter halos. I simulated an isolated halo with an early formation epoch at three mass scales in CDM and a variety of WDM cosmologies where the formation of structures below the filtering scale is suppressed. I examined the halo at epochs $z > 5$ when the halo was composed of $\sim 10^7$ particles at each mass scale and the halo was in the slow growth phase. I found the halos were changed both structurally and dynamically. Mass was rearranged in the WDM halos with radii $< 0.1 R_{vir}$ gaining mass at the expense of radii $0.1 - 0.4 R_{vir}$. Particle velocity dispersions also increase in the inner profiles resulting in deviations from power law behavior in the inner coarse-grain phase space density profiles. However, velocity anisotropies after virialization are largely similar across cosmologies.

I also found a dependence on mass in the CDM profiles with larger halos exhibiting a steeper density profile as in Ricotti (2003). The spin parameter decreases with increasing mass in agreement with the models of Del Popolo (2009) that more massive halos have less angular momentum resulting in steeper profiles. The WDM halos have similar spins across mass scales and also have similar profiles.

My work shows that the shape of halo profiles cannot be parameterized simply by a generalized NFW or Einasto profile with a concentration or scale radius dependent on the mass or cosmology. The halo shape is more complex, with logarithmic slopes that can vary non-monotonically and with features in the profile that reflect

the shape of the power spectrum. Thus, in general halos cannot be fitted by a universal density profile. This is actually good news because it may become feasibile to find fingerprints of the initial power spectrum of perturbations on galactic or sub-galactic scales in the density profiles of dark matter dominated dwarf galaxies or clusters.

Chapter 6:   Conclusion

I have shown how N-body simulations of the MW can be combined with observations of its satellite population to explore the nature of dark matter. Both the number of satellites and their densities are sensitive to the small scale power spectrum. One way the power spectrum can be reduced is by WDM where streaming motions in the early universe truncate the power below a scale dependent on the mass of the dark matter particle. I have shown how a thermal relic mass of ~ 2 keV is able to reproduce the total number of satellites, including the ultra-faint dwarfs discovered in the SDSS, and reconcile the observed stellar dynamics of the brightest dwarfs. It is intriguing that this is also the value recently shown for sterile neutrinos that would be consistent with the observed X-ray emission line from galaxy clusters. For masses > 2 keV the densities of the largest dwarfs are more sensitive to the small scale power determined by n_s and σ_8 than the nature of the dark matter.

If, however, the interpretation of the *Fermi* data is correct that the gamma ray emissions from the Galactic Center are caused by annihilating CDM particles with mass $\sim 30 - 100$ GeV the MW satellites still provide an excellent method to probe the power spectrum. This is important because while the *Fermi* observations can probe the inner density profile of the MW they do not constrain the small scale power

spectrum of CDM. If the dark matter is cold but with a cutoff like a 2 keV thermal relic the MW mass is $> 300 M_f$ and its density profile is indistinguishable from standard CDM. Determining the power spectrum is important for testing theories of CDM production and possible interactions with the photon-baryon plasma in the early universe. Future surveys will ensure that small scale structures in the local universe remain a powerful tool for probing the nature of dark matter by improving sky coverage and luminosity limits and reducing uncertainties in the number of MW satellites.

I have also shown how N-body simulations in CDM and WDM can be used to demonstrate the dependence of the structural and dynamical profiles of dark matter halos on the power spectrum of initial conditions. For halos near the filtering mass, the inner density profile in WDM deviates from CDM with a mass increase up to a factor of three in the inner halo. The scale of the deviation scales with the free streaming length indicating some memory of the initial conditions is retained in the halo core. A dependence on mass is also seen in the cold dark matter profiles with more massive halos exhibiting steeper profiles. The increased core mass is at the expense of matter at intermediate scales and supports analytic models of halo structure formation that include angular momentum and argue against a universal form for the density profile.

6.1 Future Work

Extensive simulation and modeling work over the past two decades have shown that reionization of the IGM at $z \sim 10$ suppresses gas accretion and prevents galaxy formation in dark matter halos with masses less than $10^{8-9} M_\odot$. Ricotti (2009) proposed, however, that these minihalos may experience a late-phase of gas accretion due to the increasing concentration of the dark matter halo and a decreasing IGM temperature due to helium reionization at $z < 3$. In this scenario the accreted gas for isolated minihalos in low density regions is expected to have very low metallicity and is unlikely to form stars. The gravitational potential well of the minihalo core grows deep enough for the ionized gas density to increase and allow a fraction of the gas to recombine. Lyman-α emission quickly cools the neutral hydrogen and allows the gas to condense isothermally. Core gas densities of $1 - 10$ neutral hydrogen atoms per cubic centimeter are predicted. These objects may be observable by their 21 cm emission with existing and future radio telescopes.

If these gas-rich minihalos exist they would be a unique probe of the power spectrum at scales smaller than the ultra-faint dwarfs of the Milky Way. They would further constrain the nature of dark matter and would address the question of what is the minimum mass a galaxy can have, a fundamental unanswered question in cosmology. They may also offer a unique probe of the thermal and metal enrichment history of the IGM and of the ionizing background radiation field.

Gas-rich minihalos offer exciting prospects but simulations must first be conducted to test the predictions of the theoretical arguments. The likelihood of mini-

halo formation, their sensitivity to the properties of the IGM, and their detectability must be quantified. I have started preliminary work on such simulations by identifying candidate minihalos in void regions of a cosmological volume and testing methods to decrease the computation time without affecting the accuracy in the refinement region. My preliminary simulations are limited by their low resolution and lack the hydrodynamics to model the baryonic gas in the dark matter halos. Ultimately, a mass dynamic range greater than 10^6 will be required to resolve the parsec-scale cores of minihalos while also sampling the gravitational forces from the mass distribution on Mpc scales.

I plan to pursue funding opportunities to continue this research. If funding can be acquired I will build on my preliminary work by testing the performance of more efficient N-body codes (GADGET3) and more robust initial condition generators (MUSIC, Hahn and Abel 2011). I will also add gas particles with detailed heating and cooling physics and run multiple simulations varying the free parameters of the radiation background, temperature of the IGM, and metallicity of the accreted gas. I will quantify the number, flux, and size distribution of minihalos and produce synthetic maps for 21 cm observations.

Chapter A: Testing for bias in subhalo abundances from BBKS

In Chapter 3 the BBKS formula for the CDM transfer function was used when generating the initial conditions for the high resolution simulations. This formula assumes a baryon density of zero. Eisenstein and Hu (1998) calculated transfer functions for CDM cosmologies that include baryon physics.

Plotted in Figure A.1 are the power spectrum from the fitting formula of Eisenstein & Hu and the spectrum calculated with the LINGER software (using $\Omega_b = 0.04$) normalized by BBKS. With $\Omega_m = 0.238$ a Milky Way-sized halo with mass $\sim 2 \times 10^{12} M_\odot$ would form from a spherical region with diameter 4.8 Mpc ($k = 0.28\, h/\text{Mpc}$); this is plotted along with the scale of the simulation box (90 Mpc) as solid vertical lines. Dashed vertical lines show the cell size in the refinement region of the low and high resolution simulations.

Figure A.1 shows that, for a fixed value of σ_8, BBKS underestimates power on scales $k \lesssim 0.1$ but the power spectra are nearly identical for scales $\lesssim 14$ Mpc with BBKS slightly power overabundant by $\sim 10\%$. The *set C* halos showed subhalo abundance variations much greater than 10% and the BBKS power overabundance is much less than the 30% (1σ) intrinsic scatter in subhalo abundance for MW-sized halos adopted in Chapter 3.
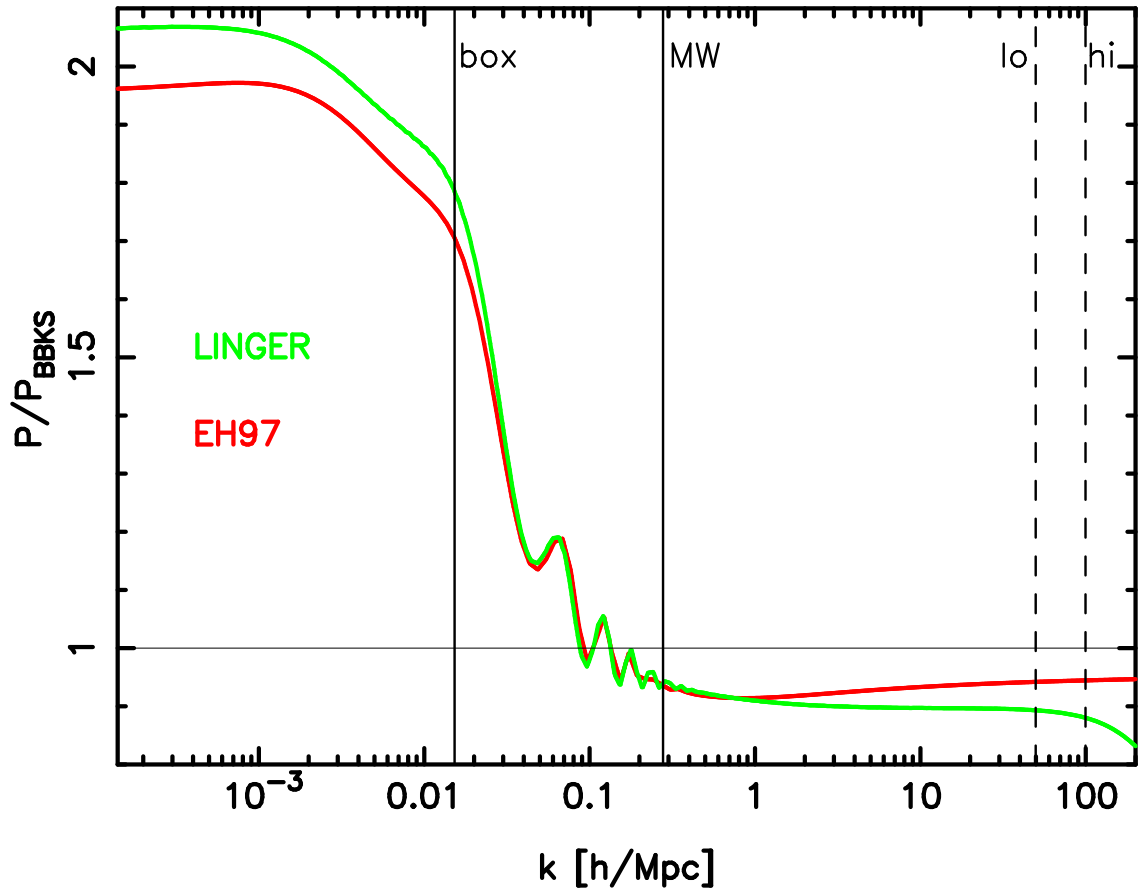
Figure A.1: Comparison of CDM power spectra calculated from the fitting formula of Eisenstein and Hu (1998) (EH97) and from the LINGER software normalized by BBKS. On scales $k > 0.1\ h/$Mpc (< 14 Mpc) the power spectra are nearly identical. The 'MW' vertical line is the diameter of a spherical region with density $\Omega_m \rho_c$ enclosing a Milky Way-sized mass $2 \times 10^{12} M_\odot$ (~ 5 Mpc). This scale is well within the range where the power spectra are nearly equal.
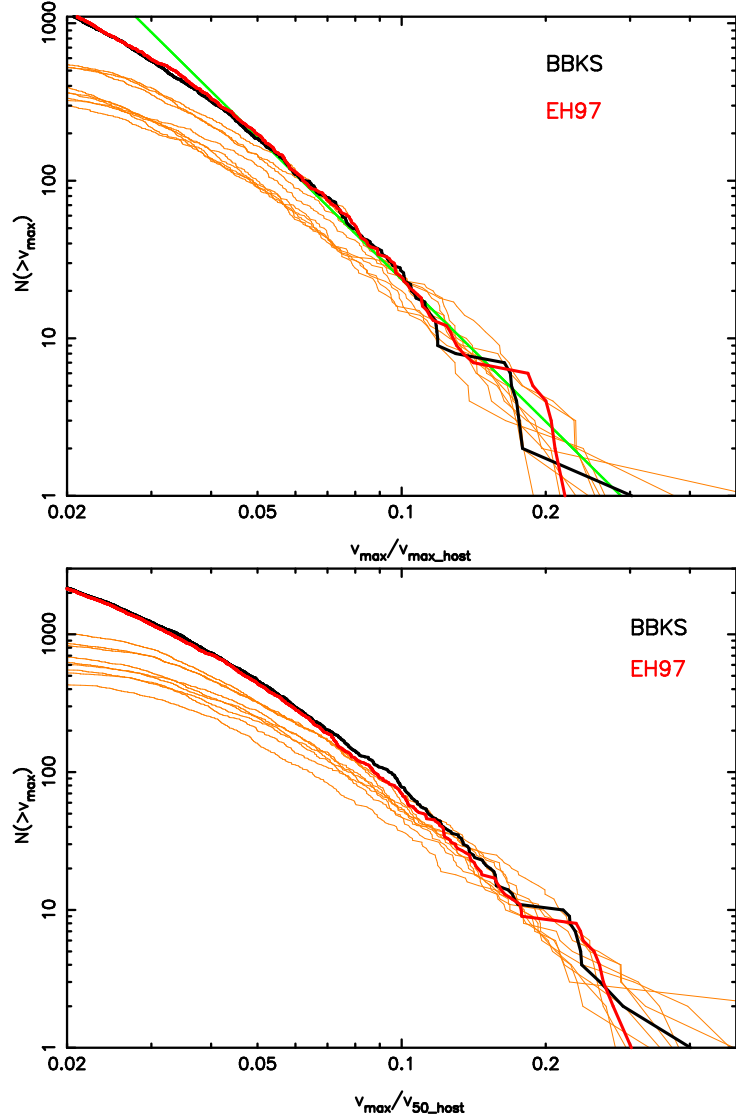
Figure A.2: Subhalo velocity function comparison for CDM high resolution set *B* simulations using fitting formula from BBKS and Eisenstein & Hu (*thick lines*) and the LINGER using *set C* simulations (*thin lines*). (*top*) Subhalos within R_{100} and velocities normalized by v_{max} of their host. The straight sloped line is the fitting formula from the Bolshoi simulation. (*bottom*) Subhalos within R_{50}, normalized by v_{50} of their host. The subhalo abundances between the BBKS and EH97 simulations are in good agreement and within the scatter of the *set C* halos.

To check if BBKS might affect the number of satellites, I reran the *set B* high resolution CDM simulation using initial conditions generated from the formula of Eisenstein & Hu. The panels of Figure A.2 compare the velocity functions of satellites and show good agreement between the simulations and within the scatter of the *set C* simulations. Based on this and the agreement between the BBKS and *set C* simulations seen in Section 3.3, I conclude that the use of BBKS has not introduced a systematic error into the results of Chapter 3.

Bibliography

K. Abazajian. Linear cosmological structure limits on warm dark matter. Phys. Rev. D, 73(6):063513–+, March 2006. doi: 10.1103/PhysRevD.73.063513.

K. Abazajian and S. M. Koushiappas. Constraints on sterile neutrino dark matter. Phys. Rev. D, 74(2):023527–+, July 2006. doi: 10.1103/PhysRevD.74.023527.

K. N. Abazajian. Resonantly-Produced 7 keV Sterile Neutrino Dark Matter Models and the Properties of Milky Way Satellites. *ArXiv e-prints*, March 2014.

K. N. Abazajian and M. Kaplinghat. Detection of a gamma-ray source in the Galactic Center consistent with extended emission from dark matter annihilation and concentrated astrophysical emission. Phys. Rev. D, 86(8):083511, October 2012. doi: 10.1103/PhysRevD.86.083511.

K. N. Abazajian, M. Markevitch, S. M. Koushiappas, and R. C. Hickox. Limits on the radiative decay of sterile neutrino dark matter from the unresolved cosmic and soft x-ray backgrounds. Phys. Rev. D, 75(6):063511–+, March 2007. doi: 10.1103/PhysRevD.75.063511.

K. N. Abazajian, N. Canac, S. Horiuchi, and M. Kaplinghat. Astrophysical and Dark Matter Interpretations of Extended Gamma Ray Emission from the Galactic Center. *ArXiv e-prints*, February 2014.

A. A. Aguilar-Arevalo, A. O. Bazarko, S. J. Brice, B. C. Brown, L. Bugel, J. Cao, L. Coney, J. M. Conrad, D. C. Cox, A. Curioni, Z. Djurcic, D. A. Finley, B. T. Fleming, R. Ford, F. G. Garcia, G. T. Garvey, C. Green, J. A. Green, T. L. Hart, E. Hawker, R. Imlay, R. A. Johnson, P. Kasper, T. Katori, T. Kobilar-cik, I. Kourbanis, S. Koutsoliotas, E. M. Laird, J. M. Link, Y. Liu, Y. Liu, W. C. Louis, K. B. M. Mahn, W. Marsh, P. S. Martin, G. McGregor, W. Met-calf, P. D. Meyers, F. Mills, G. B. Mills, J. Monroe, C. D. Moore, R. H. Nelson, P. Nienaber, S. Ouedraogo, R. B. Patterson, D. Perevalov, C. C. Polly, E. Pre-bys, J. L. Raaf, H. Ray, B. P. Roe, A. D. Russell, V. Sandberg, R. Schirato, D. Schmitz, M. H. Shaevitz, F. C. Shoemaker, D. Smith, M. Sorel, P. Spent-zouris, I. Stancu, R. J. Stefanski, M. Sung, H. A. Tanaka, R. Tayloe, M. Tzanov,

R. van de Water, M. O. Wascko, D. H. White, M. J. Wilking, H. J. Yang, G. P. Zeller, and E. D. Zimmerman. Search for Electron Neutrino Appearance at the $\Delta m^2 \sim 1$ eV^2 Scale. Phys. Rev. Lett., 98(23):231801–+, June 2007. doi: 10.1103/PhysRevLett.98.231801.

A. A. Aguilar-Arevalo, C. E. Anderson, A. O. Bazarko, S. J. Brice, B. C. Brown, L. Bugel, J. Cao, L. Coney, J. M. Conrad, D. C. Cox, A. Curioni, Z. Djurcic, D. A. Finley, B. T. Fleming, R. Ford, F. G. Garcia, G. T. Garvey, C. Green, J. A. Green, T. L. Hart, E. Hawker, R. Imlay, R. A. Johnson, G. Karagiorgi, P. Kasper, T. Katori, T. Kobilarcik, I. Kourbanis, S. Koutsoliotas, E. M. Laird, S. K. Linden, J. M. Link, Y. Liu, Y. Liu, W. C. Louis, K. B. M. Mahn, W. Marsh, G. McGregor, W. Metcalf, P. D. Meyers, F. Mills, G. B. Mills, J. Monroe, C. D. Moore, R. H. Nelson, V. T. Nguyen, P. Nienaber, J. A. Nowak, S. Ouedraogo, R. B. Patterson, D. Perevalov, C. C. Polly, E. Prebys, J. L. Raaf, H. Ray, B. P. Roe, A. D. Russell, V. Sandberg, R. Schirato, D. Schmitz, M. H. Shaevitz, F. C. Shoemaker, D. Smith, M. Sodeberg, M. Sorel, P. Spentzouris, I. Stancu, R. J. Stefanski, M. Sung, H. A. Tanaka, R. Tayloe, M. Tzanov, R. van de Water, M. O. Wascko, D. H. White, M. J. Wilking, H. J. Yang, G. P. Zeller, and E. D. Zimmerman. Unexplained Excess of Electronlike Events from a 1-GeV Neutrino Beam. Phys. Rev. Lett., 102(10):101802–+, March 2009. doi: 10.1103/PhysRevLett.102.101802.

A. A. Aguilar-Arevalo, C. E. Anderson, S. J. Brice, B. C. Brown, L. Bugel, J. M. Conrad, R. Dharmapalan, Z. Djurcic, B. T. Fleming, R. Ford, F. G. Garcia, G. T. Garvey, J. Mirabal, J. Grange, J. A. Green, R. Imlay, R. A. Johnson, G. Karagiorgi, T. Katori, T. Kobilarcik, S. K. Linden, W. C. Louis, K. B. M. Mahn, W. Marsh, C. Mauger, W. Metcalf, G. B. Mills, C. D. Moore, J. Mousseau, R. H. Nelson, V. Nguyen, P. Nienaber, J. A. Nowak, B. Osmanov, Z. Pavlovic, D. Perevalov, C. C. Polly, H. Ray, B. P. Roe, A. D. Russell, R. Schirato, M. H. Shaevitz, M. Sorel, J. Spitz, I. Stancu, R. J. Stefanski, R. Tayloe, M. Tzanov, R. G. van de Water, M. O. Wascko, D. H. White, M. J. Wilking, G. P. Zeller, and E. D. Zimmerman. Event Excess in the MiniBooNE Search for $\nu_\mu \rightarrow \nu_e$ Oscillations. Phys. Rev. Lett., 105(18):181801–+, October 2010. doi: 10.1103/PhysRevLett.105.181801.

E. Akhmedov and T. Schwetz. MiniBooNE and LSND data: non-standard neutrino interactions in a (3+1) scheme versus (3+2) oscillations. *J. High Energy Physics*, 10:115–+, October 2010. doi: 10.1007/JHEP10(2010)115.

D. Anderhalden, A. Schneider, A. V. Macciò, J. Diemand, and G. Bertone. Hints on the nature of dark matter from the properties of Milky Way satellites. JCAP, 3:014, March 2013. doi: 10.1088/1475-7516/2013/03/014.

T. Asaka, M. Shaposhnikov, and A. Kusenko. Opening a new window for warm dark matter. Phys. Rev. B, 638:401–406, July 2006. doi: 10.1016/j.physletb.2006.05.067.

Y. Ascasibar, G. Yepes, S. Gottlöber, and V. Müller. On the physical origin of dark matter density profiles. MNRAS, 352:1109–1120, August 2004. doi: 10.1111/j.1365-2966.2004.08005.x.

C. Athanassopoulos, L. B. Auerbach, D. A. Bauer, R. D. Bolton, B. Boyd, R. L. Burman, D. O. Caldwell, I. Cohen, B. D. Dieterle, J. B. Donahue, A. M. Eisner, A. Fazely, F. J. Federspiel, G. T. Garvey, M. Gray, and et al. Candidate events in a search for $\bar{\nu}_\mu \to \bar{\nu}_e$ oscillations. Phys. Rev. Lett., 75:2650–2653, October 1995. doi: 10.1103/PhysRevLett.75.2650.

C. Athanassopoulos, L. B. Auerbach, R. L. Burman, I. Cohen, D. O. Caldwell, B. D. Dieterle, J. B. Donahue, A. M. Eisner, A. Fazely, F. J. Federspiel, G. T. Garvey, M. Gray, R. M. Gunasingha, R. Imlay, K. Johnston, H. J. Kim, W. C. Louis, R. Majkic, J. Margulies, K. McIlhany, W. Metcalf, G. B. Mills, R. A. Reeder, V. Sandberg, D. Smith, I. Stancu, W. Strossman, R. Tayloe, G. J. Vandalen, W. Vernon, N. Wadia, J. Waltz, Y.-X. Wang, D. H. White, D. Works, Y. Xiao, and S. Yellin. Evidence for $\nu_\mu \to \nu_e$ Oscillations from the LSND Experiment at the Los Alamos Meson Physics Facility. Phys. Rev. Lett., 77:3082–3085, October 1996. doi: 10.1103/PhysRevLett.77.3082.

C. Athanassopoulos, L. B. Auerbach, R. L. Burman, D. O. Caldwell, E. D. Church, I. Cohen, J. B. Donahue, A. Fazely, F. J. Federspiel, G. T. Garvey, R. M. Gunasingha, R. Imlay, K. Johnston, H. J. Kim, W. C. Louis, R. Majkic, K. McIlhany, G. B. Mills, R. A. Reeder, V. Sandberg, D. Smith, I. Stancu, W. Strossman, R. Tayloe, G. J. Vandalen, W. Vernon, N. Wadia, J. Waltz, D. H. White, D. Works, Y. Xiao, and S. Yellin. Results on $\nu_\mu \to \nu_e$ Neutrino Oscillations from the LSND Experiment. Phys. Rev. Lett., 81:1774–1777, August 1998a. doi: 10.1103/PhysRevLett.81.1774.

C. Athanassopoulos, L. B. Auerbach, R. L. Burman, D. O. Caldwell, E. D. Church, I. Cohen, J. B. Donahue, A. Fazely, F. J. Federspiel, G. T. Garvey, R. M. Gunasingha, R. Imlay, K. Johnston, H. J. Kim, W. C. Louis, R. Majkic, K. McIlhany, W. Metcalf, G. B. Mills, R. A. Reeder, V. Sandberg, D. Smith, I. Stancu, W. Strossman, R. Tayloe, G. J. Vandalen, W. Vernon, N. Wadia, J. Waltz, D. H. White, D. Works, Y. Xiao, and S. Yellin. Results on $\nu_\mu \to \nu_e$ oscillations from pion decay in flight neutrinos. Phys. Rev. C, 58:2489–2511, October 1998b. doi: 10.1103/PhysRevC.58.2489.

C. G. Austin, L. L. R. Williams, E. I. Barnes, A. Babul, and J. J. Dalcanton. Semianalytical Dark Matter Halos and the Jeans Equation. ApJ, 634:756–774, November 2005. doi: 10.1086/497133.

V. Avila-Reese, P. Colín, O. Valenzuela, E. D'Onghia, and C. Firmani. Formation and Structure of Halos in a Warm Dark Matter Cosmology. ApJ, 559:516–530, October 2001. doi: 10.1086/322411.

J. M. Bardeen, J. R. Bond, N. Kaiser, and A. S. Szalay. The statistics of peaks of Gaussian random fields. ApJ, 304:15–61, May 1986. doi: 10.1086/164143.

R. Barkana, Z. Haiman, and J. P. Ostriker. Constraints on Warm Dark Matter from Cosmological Reionization. ApJ, 558:482–496, September 2001. doi: 10.1086/322393.

E. I. Barnes, L. L. R. Williams, A. Babul, and J. J. Dalcanton. Density Profiles of Collisionless Equilibria. I. Spherical Isotropic Systems. ApJ, 643:797–803, June 2006. doi: 10.1086/503025.

V. Belokurov, D. B. Zucker, N. W. Evans, J. T. Kleyna, S. Koposov, S. T. Hodgkin, M. J. Irwin, G. Gilmore, M. I. Wilkinson, M. Fellhauer, D. M. Bramich, P. C. Hewett, S. Vidrih, J. T. A. De Jong, J. A. Smith, H.-W. Rix, E. F. Bell, R. F. G. Wyse, H. J. Newberg, P. A. Mayeur, B. Yanny, C. M. Rockosi, O. Y. Gnedin, D. P. Schneider, T. C. Beers, J. C. Barentine, H. Brewington, J. Brinkmann, M. Harvanek, S. J. Kleinman, J. Krzesinski, D. Long, A. Nitta, and S. A. Snedden. Cats and Dogs, Hair and a Hero: A Quintet of New Milky Way Companions. ApJ, 654:897–906, January 2007. doi: 10.1086/509718.

V. Belokurov, M. G. Walker, N. W. Evans, D. C. Faria, G. Gilmore, M. J. Irwin, S. Koposov, M. Mateo, E. Olszewski, and D. B. Zucker. Leo V: A Companion of a Companion of the Milky Way Galaxy? ApJ, 686:L83–L86, October 2008. doi: 10.1086/592962.

V. Belokurov, M. G. Walker, N. W. Evans, G. Gilmore, M. J. Irwin, M. Mateo, L. Mayer, E. Olszewski, J. Bechtold, and T. Pickering. The discovery of Segue 2: a prototype of the population of satellites of satellites. MNRAS, 397:1748–1755, August 2009. doi: 10.1111/j.1365-2966.2009.15106.x.

V. Belokurov, M. G. Walker, N. W. Evans, G. Gilmore, M. J. Irwin, D. Just, S. Koposov, M. Mateo, E. Olszewski, L. Watkins, and L. Wyrzykowski. Big Fish, Little Fish: Two New Ultra-faint Satellites of the Milky Way. ApJ, 712: L103–L106, March 2010. doi: 10.1088/2041-8205/712/1/L103.

K. Belotsky, M. Khlopov, and K. Shibaev. Stable Matter of 4th Generation: Hidden in the Universe and Close to Detection? In A. Studenikin, editor, *Particle Physics at the Year of 250th Anniversary of Moscow University*, pages 180–+, 2006a.

K. M. Belotsky, M. Y. Khlopov, and K. I. Shibaev. Composite dark matter and its charged constituents. *Gravitation and Cosmology*, 12:93–99, June 2006b.

E. Bertschinger. Self-similar secondary infall and accretion in an Einstein-de Sitter universe. ApJS, 58:39–65, May 1985. doi: 10.1086/191028.

E. Bertschinger. Multiscale Gaussian Random Fields and Their Application to Cosmological Simulations. ApJS, 137:1–20, November 2001. doi: 10.1086/322526.

BICEP2 Collaboration, P. A. R Ade, R. W. Aikin, D. Barkats, S. J. Benton, C. A. Bischoff, J. J. Bock, J. A. Brevik, I. Buder, E. Bullock, C. D. Dowell, L. Duband, J. P. Filippini, S. Fliescher, S. R. Golwala, M. Halpern, M. Hasselfield, S. R.

Hildebrandt, G. C. Hilton, V. V. Hristov, K. D. Irwin, K. S. Karkare, J. P. Kaufman, B. G. Keating, S. A. Kernasovskiy, J. M. Kovac, C. L. Kuo, E. M. Leitch, M. Lueker, P. Mason, C. B. Netterfield, H. T. Nguyen, R. O'Brient, R. W. Ogburn, IV, A. Orlando, C. Pryke, C. D. Reintsema, S. Richter, R. Schwarz, C. D. Sheehy, Z. K. Staniszewski, R. V. Sudiwala, G. P. Teply, J. E. Tolan, A. D. Turner, A. G. Vieregg, C. L. Wong, and K. W. Yoon. BICEP2 I: Detection Of B-mode Polarization at Degree Angular Scales. *ArXiv e-prints*, March 2014.

G. R. Blumenthal, H. Pagels, and J. R. Primack. Galaxy formation by dissipationless particles heavier than neutrinos. Nature, 299:37, September 1982. doi: 10.1038/299037a0.

P. Bode, J. P. Ostriker, and N. Turok. Halo Formation in Warm Dark Matter Models. ApJ, 556:93–107, July 2001. doi: 10.1086/321541.

H. Böhringer. Clusters of Galaxies. In H. Böhringer, G. E. Morfill, and J. E. Trümper, editors, *Seventeeth Texas Symposium on Relativistic Astrophysics and Cosmology*, volume 759 of *Annals of the New York Academy of Sciences*, page 67, 1995. doi: 10.1111/j.1749-6632.1995.tb17517.x.

J. R. Bond, S. Cole, G. Efstathiou, and N. Kaiser. Excursion set mass functions for hierarchical Gaussian fluctuations. ApJ, 379:440–460, October 1991. doi: 10.1086/170520.

M. S. Bovill and M. Ricotti. Pre-Reionization Fossils, Ultra-Faint Dwarfs, and the Missing Galactic Satellite Problem. ApJ, 693:1859–1870, March 2009a. doi: 10.1088/0004-637X/693/2/1859.

M. S. Bovill and M. Ricotti. Pre-Reionization Fossils, Ultra-Faint Dwarfs, and the Missing Galactic Satellite Problem. ApJ, 693:1859–1870, March 2009b. doi: 10.1088/0004-637X/693/2/1859.

M. S. Bovill and M. Ricotti. Where are the Fossils of the First Galaxies? I. Local Volume Maps and Properties of the Undetected Dwarfs. ApJ, 741:17, November 2011a. doi: 10.1088/0004-637X/741/1/17.

M. S. Bovill and M. Ricotti. Where are the Fossils of the First Galaxies? II. True Fossils, Ghost Halos, and the Missing Bright Satellites. ApJ, 741:18, November 2011b. doi: 10.1088/0004-637X/741/1/18.

A. Boyarsky, A. Neronov, O. Ruchayskiy, and M. Shaposhnikov. Restrictions on parameters of sterile neutrino dark matter from observations of galaxy clusters. Phys. Rev. D, 74(10):103506–+, November 2006a. doi: 10.1103/PhysRevD.74.103506.

A. Boyarsky, A. Neronov, O. Ruchayskiy, and M. Shaposhnikov. Constraints on sterile neutrinos as dark matter candidates from the diffuse X-ray background. MNRAS, 370:213–218, July 2006b. doi: 10.1111/j.1365-2966.2006.10458.x.

A. Boyarsky, J. Nevalainen, and O. Ruchayskiy. Constraints on the parameters of radiatively decaying dark matter from the dark matter halos of the Milky Way and Ursa Minor. A&A, 471:51–57, August 2007. doi: 10.1051/0004-6361:20066774.

A. Boyarsky, O. Ruchayskiy, and M. Markevitch. Constraints on Parameters of Radiatively Decaying Dark Matter from the Galaxy Cluster 1E 0657-56. ApJ, 673:752–757, February 2008. doi: 10.1086/524397.

A. Boyarsky, J. Lesgourgues, O. Ruchayskiy, and M. Viel. Realistic Sterile Neutrino Dark Matter with KeV Mass does not Contradict Cosmological Bounds. Phys. Rev. Lett., 102(20):201304–+, May 2009. doi: 10.1103/PhysRevLett.102.201304.

A. Boyarsky, O. Ruchayskiy, D. Iakubovskyi, and J. Franse. An unidentified line in X-ray spectra of the Andromeda galaxy and Perseus galaxy cluster. *ArXiv e-prints*, February 2014.

M. Boylan-Kolchin, J. S. Bullock, and M. Kaplinghat. Too big to fail? The puzzling darkness of massive Milky Way subhaloes. MNRAS, 415:L40–L44, July 2011. doi: 10.1111/j.1745-3933.2011.01074.x.

M. Boylan-Kolchin, J. S. Bullock, and M. Kaplinghat. The Milky Way's bright satellites as an apparent failure of ΛCDM. MNRAS, 422:1203–1218, May 2012a. doi: 10.1111/j.1365-2966.2012.20695.x.

M. Boylan-Kolchin, J. S. Bullock, S. T. Sohn, G. Besla, and R. P. van der Marel. The Space Motion of Leo I: The Mass of the Milky Way's Dark Matter Halo. *ArXiv e-prints*, October 2012b.

G. L. Bryan and M. L. Norman. Statistical Properties of X-Ray Clusters: Analytic and Numerical Comparisons. ApJ, 495:80–+, March 1998. doi: 10.1086/305262.

E. Bulbul, M. Markevitch, A. Foster, R. K. Smith, M. Loewenstein, and S. W. Randall. Detection of An Unidentified Emission Line in the Stacked X-ray spectrum of Galaxy Clusters. *ArXiv e-prints*, February 2014.

J. S. Bullock, A. V. Kravtsov, and D. H. Weinberg. Reionization and the Abundance of Galactic Satellites. ApJ, 539:517–521, August 2000. doi: 10.1086/309279.

J. S. Bullock, T. S. Kolatt, Y. Sigad, R. S. Somerville, A. V. Kravtsov, A. A. Klypin, J. R. Primack, and A. Dekel. Profiles of dark haloes: evolution, scatter and environment. MNRAS, 321:559–575, March 2001a. doi: 10.1046/j.1365-8711.2001.04068.x.

J. S. Bullock, A. V. Kravtsov, and D. H. Weinberg. Hierarchical Galaxy Formation and Substructure in the Galaxy's Stellar Halo. ApJ, 548:33–46, February 2001b. doi: 10.1086/318681.

M. T. Busha, A. E. Evrard, and F. C. Adams. The Asymptotic Form of Cosmic Structure: Small-Scale Power and Accretion History. ApJ, 665:1–13, August 2007. doi: 10.1086/518764.

F. J. Castander. The Sloan Digital Sky Survey. Ap&SS, 263:91–94, June 1998. doi: 10.1023/A:1002196414003.

D. Clowe, M. Bradač, A. H. Gonzalez, M. Markevitch, S. W. Randall, C. Jones, and D. Zaritsky. A Direct Empirical Proof of the Existence of Dark Matter. ApJ, 648:L109–L113, September 2006. doi: 10.1086/508162.

P. Colín, V. Avila-Reese, and O. Valenzuela. Substructure and Halo Density Profiles in a Warm Dark Matter Cosmology. ApJ, 542:622–630, October 2000. doi: 10.1086/317057.

P. Colín, O. Valenzuela, and V. Avila-Reese. On the Structure of Dark Matter Halos at the Damping Scale of the Power Spectrum with and without Relict Velocities. ApJ, 673:203–214, January 2008. doi: 10.1086/524030.

R. J. Cooke, M. Pettini, R. A. Jorgenson, M. T. Murphy, and C. C. Steidel. Precision Measures of the Primordial Abundance of Deuterium. ApJ, 781:31, January 2014. doi: 10.1088/0004-637X/781/1/31.

T. Daylan, D. P. Finkbeiner, D. Hooper, T. Linden, S. K. N. Portillo, N. L. Rodd, and T. R. Slatyer. The Characterization of the Gamma-Ray Signal from the Central Milky Way: A Compelling Case for Annihilating Dark Matter. *ArXiv e-prints*, February 2014.

J. T. A. de Jong, N. F. Martin, H.-W. Rix, K. W. Smith, S. Jin, and A. V. Maccio'. The enigmatic pair of dwarf galaxies Leo IV and Leo V: coincidence or common origin? *ArXiv e-prints*, December 2009.

G. De Lucia, G. Kauffmann, V. Springel, S. D. M. White, B. Lanzoni, F. Stoehr, G. Tormen, and N. Yoshida. Substructures in cold dark matter haloes. MNRAS, 348:333–344, February 2004. doi: 10.1111/j.1365-2966.2004.07372.x.

A. Dekel, J. Devor, and G. Hetzroni. Galactic halo cusp-core: tidal compression in mergers. MNRAS, 341:326–342, May 2003. doi: 10.1046/j.1365-8711.2003.06432.x.

A. Del Popolo. The Cusp/Core Problem and the Secondary Infall Model. ApJ, 698: 2093–2113, June 2009. doi: 10.1088/0004-637X/698/2/2093.

A. Del Popolo. On the universality of density profiles. MNRAS, 408:1808–1817, November 2010. doi: 10.1111/j.1365-2966.2010.17288.x.

A. di Cintio, A. Knebe, N. I. Libeskind, G. Yepes, S. Gottlöber, and Y. Hoffman. Too small to succeed? Lighting up massive dark matter subhaloes of the Milky Way. MNRAS, 417:L74–L78, October 2011. doi: 10.1111/j.1745-3933.2011.01123.x.

A. Di Cintio, A. Knebe, N. I. Libeskind, C. Brook, G. Yepes, S. Gottlöber, and Y. Hoffman. Size matters: the non-universal density profile of subhaloes in SPH simulations and implications for the Milky Way's dSphs. MNRAS, March 2013. doi: 10.1093/mnras/stt240.

J. Diemand, B. Moore, and J. Stadel. Convergence and scatter of cluster density profiles. MNRAS, 353:624–632, September 2004. doi: 10.1111/j.1365-2966.2004.08094.x.

J. Diemand, M. Kuhlen, and P. Madau. Dark Matter Substructure and Gamma-Ray Annihilation in the Milky Way Halo. ApJ, 657:262–270, March 2007. doi: 10.1086/510736.

J. Diemand, M. Kuhlen, P. Madau, M. Zemp, B. Moore, D. Potter, and J. Stadel. Clumps and streams in the local dark matter distribution. Nature, 454:735–738, August 2008. doi: 10.1038/nature07153.

S. Dodelson and L. M. Widrow. Sterile neutrinos as dark matter. Phys. Rev. Lett., 72:17–20, January 1994. doi: 10.1103/PhysRevLett.72.17.

F. Donato, G. Gentile, and P. Salucci. Cores of dark matter haloes correlate with stellar scalelengths. MNRAS, 353:L17–L22, September 2004. doi: 10.1111/j.1365-2966.2004.08220.x.

J. Dubinski, J. C. Mihos, and L. Hernquist. Using Tidal Tails to Probe Dark Matter Halos. ApJ, 462:576, May 1996. doi: 10.1086/177174.

G. Efstathiou. Suppressing the formation of dwarf galaxies via photoionization. MNRAS, 256:43P–47P, May 1992.

J. Einasto. On the Construction of a Composite Model for the Galaxy and on the Determination of the System of Galactic Parameters. *Trudy Astrofizicheskogo Instituta Alma-Ata*, 5:87–100, 1965.

D. J. Eisenstein and W. Hu. Baryonic Features in the Matter Transfer Function. ApJ, 496:605–+, March 1998. doi: 10.1086/305424.

D. J. Eisenstein and P. Hut. HOP: A New Group-Finding Algorithm for N-Body Simulations. ApJ, 498:137–+, May 1998. doi: 10.1086/305535.

V. R. Eke, S. Cole, and C. S. Frenk. Cluster evolution as a diagnostic for Omega. MNRAS, 282:263–280, September 1996.

D. Fabricant, M. Lecar, and P. Gorenstein. X-ray measurements of the mass of M87. ApJ, 241:552–560, October 1980. doi: 10.1086/158369.

D. P. Finkbeiner, M. Su, and C. Weniger. Is the 130 GeV line real? A search for systematics in the Fermi-LAT data. JCAP, 1:029, January 2013. doi: 10.1088/1475-7516/2013/01/029.

L. Gao, S. D. M. White, A. Jenkins, F. Stoehr, and V. Springel. The subhalo populations of ΛCDM dark haloes. MNRAS, 355:819–834, December 2004. doi: 10.1111/j.1365-2966.2004.08360.x.

M. Geha, B. Willman, J. D. Simon, L. E. Strigari, E. N. Kirby, D. R. Law, and J. Strader. The Least-Luminous Galaxy: Spectroscopy of the Milky Way Satellite Segue 1. ApJ, 692:1464–1475, February 2009. doi: 10.1088/0004-637X/692/2/1464.

G. Gentile, A. Burkert, P. Salucci, U. Klein, and F. Walter. The Dwarf Galaxy DDO 47 as a Dark Matter Laboratory: Testing Cusps Hiding in Triaxial Halos. ApJ, 634:L145–L148, December 2005. doi: 10.1086/498939.

G. Gentile, P. Salucci, U. Klein, and G. L. Granato. NGC 3741: the dark halo profile from the most extended rotation curve. MNRAS, 375:199–212, February 2007. doi: 10.1111/j.1365-2966.2006.11283.x.

S. Ghigna, B. Moore, F. Governato, G. Lake, T. Quinn, and J. Stadel. Density Profiles and Substructure of Dark Matter Halos: Converging Results at Ultra-High Numerical Resolution. ApJ, 544:616–628, December 2000. doi: 10.1086/317221.

C. Giocoli, G. Tormen, and F. C. van den Bosch. The population of dark matter subhaloes: mass functions and average mass-loss rates. MNRAS, 386:2135–2144, June 2008. doi: 10.1111/j.1365-2966.2008.13182.x.

S. Gninenko. A resolution of puzzles from the LSND, KARMEN, and MiniBooNE experiments. *ArXiv e-prints*, September 2010.

S. N. Gninenko and D. S. Gorbunov. MiniBooNE anomaly, the decay $D_s^+ \rightarrow \mu^+ \nu_\mu$ and heavy sterile neutrino. Phys. Rev. D, 81(7):075013–+, April 2010. doi: 10.1103/PhysRevD.81.075013.

L. Goodenough and D. Hooper. Possible Evidence For Dark Matter Annihilation In The Inner Milky Way From The Fermi Gamma Ray Space Telescope. *ArXiv e-prints*, October 2009.

D. Gorbunov, A. Khmelnitsky, and V. Rubakov. Is gravitino still a warm dark matter candidate? *Journal of High Energy Physics*, 12:55–+, December 2008. doi: 10.1088/1126-6708/2008/12/055.

J. R. Gott, III. On the Formation of Elliptical Galaxies. ApJ, 201:296–310, October 1975. doi: 10.1086/153887.

A. W. Graham, D. Merritt, B. Moore, J. Diemand, and B. Terzić. Empirical Models for Dark Matter Halos. II. Inner Profile Slopes, Dynamical Profiles, and ρ/σ^3. AJ, 132:2701–2710, December 2006. doi: 10.1086/508990.

A. M. Green, S. Hofmann, and D. J. Schwarz. The power spectrum of SUSY-CDM on subgalactic scales. MNRAS, 353:L23–L27, September 2004. doi: 10.1111/j.1365-2966.2004.08232.x.

J. E. Gunn and J. R. Gott, III. On the Infall of Matter Into Clusters of Galaxies and Some Effects on Their Evolution. ApJ, 176:1, August 1972. doi: 10.1086/151605.

O. Hahn and T. Abel. Multi-scale initial conditions for cosmological simulations. MNRAS, 415:2101–2121, August 2011. doi: 10.1111/j.1365-2966.2011.18820.x.

F. Hammer, M. Puech, L. Chemin, H. Flores, and M. D. Lehnert. The Milky Way, an Exceptionally Quiet Galaxy: Implications for the Formation of Spiral Galaxies. ApJ, 662:322–334, June 2007. doi: 10.1086/516727.

A. Hektor, M. Raidal, and E. Tempel. Evidence for Indirect Detection of Dark Matter from Galaxy Clusters in Fermi γ-Ray Data. ApJ, 762:L22, January 2013. doi: 10.1088/2041-8205/762/2/L22.

A. Helmi, S. D. White, and V. Springel. The phase-space structure of a dark-matter halo: Implications for dark-matter direct detection experiments. Phys. Rev. D, 66(6):063502–+, September 2002. doi: 10.1103/PhysRevD.66.063502.

G. Hinshaw, D. Larson, E. Komatsu, D. N. Spergel, C. L. Bennett, J. Dunkley, M. R. Nolta, M. Halpern, R. S. Hill, N. Odegard, L. Page, K. M. Smith, J. L. Weiland, B. Gold, N. Jarosik, A. Kogut, M. Limon, S. S. Meyer, G. S. Tucker, E. Wollack, and E. L. Wright. Nine-Year Wilkinson Microwave Anisotropy Probe (WMAP) Observations: Cosmological Parameter Results. *ArXiv e-prints*, December 2012.

N. Hiotelis. Density profiles in a spherical infall model with non-radial motions. A&A, 382:84–91, January 2002. doi: 10.1051/0004-6361:20011620.

C. J. Hogan and J. J. Dalcanton. New dark matter physics: Clues from halo structure. Phys. Rev. D, 62(6):063511, September 2000. doi: 10.1103/PhysRevD.62.063511.

D. Hooper and L. Goodenough. Dark matter annihilation in the Galactic Center as seen by the Fermi Gamma Ray Space Telescope. *Physics Letters B*, 697:412–428, March 2011. doi: 10.1016/j.physletb.2011.02.029.

S. Horiuchi, P. J. Humphrey, J. Onorbe, K. N. Abazajian, M. Kaplinghat, and S. Garrison-Kimmel. Sterile neutrino dark matter bounds from galaxies of the Local Group. *ArXiv e-prints*, November 2013.

A. Huss, B. Jain, and M. Steinmetz. The formation and evolution of clusters of galaxies in different cosmogonies. MNRAS, 308:1011–1031, October 1999a. doi: 10.1046/j.1365-8711.1999.02757.x.

A. Huss, B. Jain, and M. Steinmetz. How Universal Are the Density Profiles of Dark Halos? ApJ, 517:64–69, May 1999b. doi: 10.1086/307161.

167

M. J. Irwin, V. Belokurov, N. W. Evans, E. V. Ryan-Weber, J. T. A. de Jong, S. Koposov, D. B. Zucker, S. T. Hodgkin, G. Gilmore, P. Prema, L. Hebb, A. Begum, M. Fellhauer, P. C. Hewett, R. C. Kennicutt, Jr., M. I. Wilkinson, D. M. Bramich, S. Vidrih, H.-W. Rix, T. C. Beers, J. C. Barentine, H. Brewington, M. Harvanek, J. Krzesinski, D. Long, A. Nitta, and S. A. Snedden. Discovery of an Unusual Dwarf Galaxy in the Outskirts of the Milky Way. ApJ, 656:L13–L16, February 2007. doi: 10.1086/512183.

T. Ishiyama, T. Fukushige, and J. Makino. Variation of the Subhalo Abundance in Dark Matter Halos. ApJ, 696:2115–2125, May 2009. doi: 10.1088/0004-637X/696/2/2115.

N. Jarosik, C. L. Bennett, J. Dunkley, B. Gold, M. R. Greason, M. Halpern, R. S. Hill, G. Hinshaw, A. Kogut, E. Komatsu, D. Larson, M. Limon, S. S. Meyer, M. R. Nolta, N. Odegard, L. Page, K. M. Smith, D. N. Spergel, G. S. Tucker, J. L. Weiland, E. Wollack, and E. L. Wright. Seven-Year Wilkinson Microwave Anisotropy Probe (WMAP) Observations: Sky Maps, Systematic Errors, and Basic Results. *ArXiv e-prints*, January 2010.

J. H. Jeans. The Stability of a Spherical Nebula. *Royal Society of London Philosophical Transactions Series A*, 199:1–53, 1902. doi: 10.1098/rsta.1902.0012.

Y. P. Jing. The Density Profile of Equilibrium and Nonequilibrium Dark Matter Halos. ApJ, 535:30–36, May 2000. doi: 10.1086/308809.

Y. P. Jing and Y. Suto. The Density Profiles of the Dark Matter Halo Are Not Universal. ApJ, 529:L69–L72, February 2000. doi: 10.1086/312463.

M. Kamionkowski and A. R. Liddle. The Dearth of Halo Dwarf Galaxies: Is There Power on Short Scales? Phys. Rev. Lett., 84:4525–4528, May 2000. doi: 10.1103/PhysRevLett.84.4525.

M. Kaplinghat. Dark matter from early decays. Phys. Rev. D, 72(6):063510–+, September 2005. doi: 10.1103/PhysRevD.72.063510.

G. Karagiorgi, Z. Djurcic, J. M. Conrad, M. H. Shaevitz, and M. Sorel. Viability of $\Delta m^2 \sim 1eV^2$ sterile neutrino mixing models in light of MiniBooNE electron neutrino and antineutrino data from the Booster and NuMI beamlines. Phys. Rev. D, 80(7):073001–+, October 2009. doi: 10.1103/PhysRevD.80.073001.

H. Katz and M. Ricotti. Two Epochs of Globular Cluster Formation from Deep Fields Luminosity Functions: Implications for Reionization and the Milky Way Satellites. *ArXiv e-prints*, November 2012.

M. Y. Khlopov. Composite dark matter from 4th generation. *ArXiv Astrophysics e-prints*, November 2005.

M. Y. Khlopov. New symmetries in microphysics, new stable forms of matter around us. *ArXiv Astrophysics e-prints*, July 2006.

M. Y. Khlopov. Composite dark matter from stable charged constituents. *ArXiv e-prints*, June 2008.

M. Y. Khlopov and C. Kouvaris. Strong interactive massive particles from a strong coupled theory. Phys. Rev. D, 77(6):065002–+, March 2008a. doi: 10.1103/PhysRevD.77.065002.

M. Y. Khlopov and C. Kouvaris. Composite dark matter from a model with composite Higgs boson. Phys. Rev. D, 78(6):065040–+, September 2008b. doi: 10.1103/PhysRevD.78.065040.

A. Klypin, A. V. Kravtsov, O. Valenzuela, and F. Prada. Where Are the Missing Galactic Satellites? ApJ, 522:82–92, September 1999. doi: 10.1086/307643.

A. A. Klypin, S. Trujillo-Gomez, and J. Primack. Dark Matter Halos in the Standard Cosmological Model: Results from the Bolshoi Simulation. ApJ, 740:102, October 2011. doi: 10.1088/0004-637X/740/2/102.

A. Knebe, J. E. G. Devriendt, A. Mahmood, and J. Silk. Merger histories in warm dark matter structure formation scenarios. MNRAS, 329:813–828, February 2002. doi: 10.1046/j.1365-8711.2002.05017.x.

A. Knebe, J. E. G. Devriendt, B. K. Gibson, and J. Silk. Top-down fragmentation of a warm dark matter filament. MNRAS, 345:1285–1290, November 2003. doi: 10.1046/j.1365-2966.2003.07044.x.

S. R. Knollmann and A. Knebe. AHF: Amiga's Halo Finder. ApJS, 182:608–624, June 2009. doi: 10.1088/0067-0049/182/2/608.

J. A. Kollmeier, A. Gould, S. Shectman, I. B. Thompson, G. W. Preston, J. D. Simon, J. D. Crane, Ž. Ivezić, and B. Sesar. Spectroscopic Confirmation of the Pisces Overdensity. ApJ, 705:L158–L162, November 2009. doi: 10.1088/0004-637X/705/2/L158.

E. Komatsu, J. Dunkley, M. R. Nolta, C. L. Bennett, B. Gold, G. Hinshaw, N. Jarosik, D. Larson, M. Limon, L. Page, D. N. Spergel, M. Halpern, R. S. Hill, A. Kogut, S. S. Meyer, G. S. Tucker, J. L. Weiland, E. Wollack, and E. L. Wright. Five-Year Wilkinson Microwave Anisotropy Probe Observations: Cosmological Interpretation. ApJS, 180:330–376, February 2009. doi: 10.1088/0067-0049/180/2/330.

E. Komatsu, K. M. Smith, J. Dunkley, C. L. Bennett, B. Gold, G. Hinshaw, N. Jarosik, D. Larson, M. R. Nolta, L. Page, D. N. Spergel, M. Halpern, R. S. Hill, A. Kogut, M. Limon, S. S. Meyer, N. Odegard, G. S. Tucker, J. L. Weiland, E. Wollack, and E. L. Wright. Seven-year Wilkinson Microwave Anisotropy Probe (WMAP) Observations: Cosmological Interpretation. ApJS, 192:18, February 2011. doi: 10.1088/0067-0049/192/2/18.

S. Koposov, V. Belokurov, N. W. Evans, P. C. Hewett, M. J. Irwin, G. Gilmore, D. B. Zucker, H.-W. Rix, M. Fellhauer, E. F. Bell, and E. V. Glushkova. The Luminosity Function of the Milky Way Satellites. ApJ, 686:279–291, October 2008. doi: 10.1086/589911.

A. Kusenko. Sterile Neutrinos, Dark Matter, and Pulsar Velocities in Models with a Higgs Singlet. Phys. Rev. Lett., 97(24):241301–+, December 2006. doi: 10.1103/PhysRevLett.97.241301.

A. Kusenko. Sterile neutrinos: The dark side of the light fermions. *Phys. Reports*, 481:1–28, September 2009. doi: 10.1016/j.physrep.2009.07.004.

R. Kuzio de Naray, G. D. Martinez, J. S. Bullock, and M. Kaplinghat. The Case Against Warm or Self-Interacting Dark Matter as Explanations for Cores in Low Surface Brightness Galaxies. ApJ, 710:L161–L166, February 2010. doi: 10.1088/2041-8205/710/2/L161.

C. Lacey and S. Cole. Merger rates in hierarchical models of galaxy formation. MNRAS, 262:627–649, June 1993.

D. Larson, J. Dunkley, G. Hinshaw, E. Komatsu, M. R. Nolta, C. L. Bennett, B. Gold, M. Halpern, R. S. Hill, N. Jarosik, A. Kogut, M. Limon, S. S. Meyer, N. Odegard, L. Page, K. M. Smith, D. N. Spergel, G. S. Tucker, J. L. Weiland, E. Wollack, and E. L. Wright. Seven-Year Wilkinson Microwave Anisotropy Probe (WMAP) Observations: Power Spectra and WMAP-Derived Parameters. *ArXiv e-prints*, January 2010.

Antony Lewis and Sarah Bridle. Cosmological parameters from CMB and other data: a Monte- Carlo approach. *Phys. Rev.*, D66:103511, 2002.

A. Loeb and M. Zaldarriaga. Small-scale power spectrum of cold dark matter. Phys. Rev. D, 71(10):103520, May 2005. doi: 10.1103/PhysRevD.71.103520.

M. Loewenstein, A. Kusenko, and P. L. Biermann. New Limits on Sterile Neutrinos from Suzaku Observations of the Ursa Minor Dwarf Spheroidal Galaxy. ApJ, 700: 426–435, July 2009. doi: 10.1088/0004-637X/700/1/426.

M. R. Lovell, V. Eke, C. S. Frenk, L. Gao, A. Jenkins, T. Theuns, J. Wang, S. D. M. White, A. Boyarsky, and O. Ruchayskiy. The haloes of bright satellite galaxies in a warm dark matter universe. MNRAS, 420:2318–2324, March 2012. doi: 10.1111/j.1365-2966.2011.20200.x.

M. R. Lovell, C. S. Frenk, V. R. Eke, A. Jenkins, L. Gao, and T. Theuns. The properties of warm dark matter haloes. *ArXiv e-prints*, August 2013.

Y. Lu, H. J. Mo, N. Katz, and M. D. Weinberg. On the origin of cold dark matter halo density profiles. MNRAS, 368:1931–1940, June 2006. doi: 10.1111/j.1365-2966.2006.10270.x.

LUX Collaboration, D. S. Akerib, H. M. Araujo, X. Bai, A. J. Bailey, J. Balajthy, S. Bedikian, E. Bernard, A. Bernstein, A. Bolozdynya, A. Bradley, D. Byram, S. B. Cahn, M. C. Carmona-Benitez, C. Chan, J. J. Chapman, A. A. Chiller, C. Chiller, K. Clark, T. Coffey, A. Currie, A. Curioni, S. Dazeley, L. de Viveiros, A. Dobi, J. Dobson, E. M. Dragowsky, E. Druszkiewicz, B. Edwards, C. H. Faham, S. Fiorucci, C. Flores, R. J. Gaitskell, V. M. Gehman, C. Ghag, K. R. Gibson, M. G. D. Gilchriese, C. Hall, M. Hanhardt, S. A. Hertel, M. Horn, D. Q. Huang, M. Ihm, R. G. Jacobsen, L. Kastens, K. Kazkaz, R. Knoche, S. Kyre, R. Lander, N. A. Larsen, C. Lee, D. S. Leonard, K. T. Lesko, A. Lindote, M. I. Lopes, A. Lyashenko, D. C. Malling, R. Mannino, D. N. McKinsey, D.-M. Mei, J. Mock, M. Moongweluwan, J. Morad, M. Morii, A. S. J. Murphy, C. Nehrkorn, H. Nelson, F. Neves, J. A. Nikkel, R. A. Ott, M. Pangilinan, P. D. Parker, E. K. Pease, K. Pech, P. Phelps, L. Reichhart, T. Shutt, C. Silva, W. Skulski, C. J. Sofka, V. N. Solovov, P. Sorensen, T. Stiegler, K. O'Sullivan, T. J. Sumner, R. Svoboda, M. Sweany, M. Szydagis, D. Taylor, B. Tennyson, D. R. Tiedt, M. Tripathi, S. Uvarov, J. R. Verbus, N. Walsh, R. Webb, J. T. White, D. White, M. S. Witherell, M. Wlasenko, F. L. H. Wolfs, M. Woods, and C. Zhang. First results from the LUX dark matter experiment at the Sanford Underground Research Facility. *ArXiv e-prints*, October 2013.

D. Lynden-Bell. Statistical mechanics of violent relaxation in stellar systems. MN-RAS, 136:101, 1967.

A. V. Maccio' and F. Fontanot. How cold is Dark Matter? Constraints from Milky Way Satellites. *ArXiv e-prints*, October 2009.

A. V. Macciò, A. A. Dutton, F. C. van den Bosch, B. Moore, D. Potter, and J. Stadel. Concentration, spin and shape of dark matter haloes: scatter and the dependence on mass and environment. MNRAS, 378:55–71, June 2007. doi: 10.1111/j.1365-2966.2007.11720.x.

A. V. Macciò, A. A. Dutton, and F. C. van den Bosch. Concentration, spin and shape of dark matter haloes as a function of the cosmological model: WMAP1, WMAP3 and WMAP5 results. MNRAS, 391:1940–1954, December 2008. doi: 10.1111/j.1365-2966.2008.14029.x.

A. V. Macciò, S. Paduroiu, D. Anderhalden, A. Schneider, and B. Moore. Cores in warm dark matter haloes: a Catch 22 problem. MNRAS, 424:1105–1112, August 2012. doi: 10.1111/j.1365-2966.2012.21284.x.

M. Maltoni and T. Schwetz. Sterile neutrino oscillations after first MiniBooNE results. Phys. Rev. D, 76(9):093005–+, November 2007. doi: 10.1103/Phys-RevD.76.093005.

A. Manrique, A. Raig, E. Salvador-Solé, T. Sanchis, and J. M. Solanes. On the Origin of the Inner Structure of Halos. ApJ, 593:26–37, August 2003. doi: 10.1086/376403.

N. F. Martin, R. A. Ibata, S. C. Chapman, M. Irwin, and G. F. Lewis. A Keck/DEIMOS spectroscopic survey of faint Galactic satellites: searching for the least massive dwarf galaxies. MNRAS, 380:281–300, September 2007. doi: 10.1111/j.1365-2966.2007.12055.x.

M. L. Mateo. Dwarf Galaxies of the Local Group. ARA&A, 36:435–506, 1998. doi: 10.1146/annurev.astro.36.1.435.

P. McDonald, U. Seljak, S. Burles, D. J. Schlegel, D. H. Weinberg, R. Cen, D. Shih, J. Schaye, D. P. Schneider, N. A. Bahcall, J. W. Briggs, J. Brinkmann, R. J. Brunner, M. Fukugita, J. E. Gunn, Ž. Ivezić, S. Kent, R. H. Lupton, and D. E. Vanden Berk. The Lyα Forest Power Spectrum from the Sloan Digital Sky Survey. ApJS, 163:80–109, March 2006. doi: 10.1086/444361.

A. Melchiorri, O. Mena, S. Palomares-Ruiz, S. Pascoli, A. Slosar, and M. Sorel. Sterile neutrinos in light of recent cosmological and oscillation data: a multi-flavor scheme approach. JCAP, 1:36–+, January 2009. doi: 10.1088/1475-7516/2009/01/036.

A. L. Melott. Comment on 'Discreteness Effects in Simulations of Hot/Warm Dark Matter' by J. Wang & S.D.M. White. *ArXiv e-prints*, September 2007.

P. Meszaros. The behaviour of point masses in an expanding cosmological substratum. A&A, 37:225–228, December 1974.

M. Milgrom. A modification of the Newtonian dynamics as a possible alternative to the hidden mass hypothesis. ApJ, 270:365–370, July 1983. doi: 10.1086/161130.

M. Miranda and A. V. Macciò. Constraining warm dark matter using QSO gravitational lensing. MNRAS, 382:1225–1232, December 2007. doi: 10.1111/j.1365-2966.2007.12440.x.

B. Moore, S. Ghigna, F. Governato, G. Lake, T. Quinn, J. Stadel, and P. Tozzi. Dark Matter Substructure within Galactic Halos. ApJ, 524:L19–L22, October 1999a. doi: 10.1086/312287.

B. Moore, T. Quinn, F. Governato, J. Stadel, and G. Lake. Cold collapse and the core catastrophe. MNRAS, 310:1147–1152, December 1999b. doi: 10.1046/j.1365-8711.1999.03039.x.

J. F. Navarro, C. S. Frenk, and S. D. M. White. The Structure of Cold Dark Matter Halos. ApJ, 462:563, May 1996. doi: 10.1086/177173.

J. F. Navarro, C. S. Frenk, and S. D. M. White. A Universal Density Profile from Hierarchical Clustering. ApJ, 490:493, December 1997. doi: 10.1086/304888.

J. F. Navarro, E. Hayashi, C. Power, A. R. Jenkins, C. S. Frenk, S. D. M. White, V. Springel, J. Stadel, and T. R. Quinn. The inner structure of ΛCDM haloes - III. Universality and asymptotic slopes. MNRAS, 349:1039–1051, April 2004. doi: 10.1111/j.1365-2966.2004.07586.x.

A. F. Neto, L. Gao, P. Bett, S. Cole, J. F. Navarro, C. S. Frenk, S. D. M. White, V. Springel, and A. Jenkins. The statistics of Λ CDM halo concentrations. MN-RAS, 381:1450–1462, November 2007. doi: 10.1111/j.1365-2966.2007.12381.x.

A. Nusser and R. K. Sheth. Mass growth and density profiles of dark matter haloes in hierarchical clustering. MNRAS, 303:685–695, March 1999. doi: 10.1046/j.1365-8711.1999.02197.x.

J. P. Ostriker and P. J. E. Peebles. A Numerical Study of the Stability of Flattened Galaxies: or, can Cold Galaxies Survive? ApJ, 186:467–480, December 1973. doi: 10.1086/152513.

H. Päs, S. Pakvasa, and T. J. Weiler. Sterile-active neutrino oscillations and short-cuts in the extra dimension. Phys. Rev. D, 72(9):095017–+, November 2005. doi: 10.1103/PhysRevD.72.095017.

P. J. E. Peebles. The Gravitational-Instability Picture and the Nature of the Distribution of Galaxies. ApJ, 189:L51, April 1974. doi: 10.1086/181462.

Planck Collaboration, P. A. R. Ade, N. Aghanim, C. Armitage-Caplan, M. Arnaud, M. Ashdown, F. Atrio-Barandela, J. Aumont, C. Baccigalupi, A. J. Banday, and et al. Planck 2013 results. XVI. Cosmological parameters. *ArXiv e-prints*, March 2013.

E. Polisensky and M. Ricotti. Constraints on the dark matter particle mass from the number of Milky Way satellites. Phys. Rev. D, 83(4):043506, February 2011. doi: 10.1103/PhysRevD.83.043506.

E. Polisensky and M. Ricotti. Massive Milky Way satellites in cold and warm dark matter: dependence on cosmology. MNRAS, 437:2922–2931, January 2014. doi: 10.1093/mnras/stt2105.

C. Power, J. F. Navarro, A. Jenkins, C. S. Frenk, S. D. M. White, V. Springel, J. Stadel, and T. Quinn. The inner structure of ΛCDM haloes - I. A numerical convergence study. MNRAS, 338:14–34, January 2003. doi: 10.1046/j.1365-8711.2003.05925.x.

F. Prada, A. A. Klypin, A. J. Cuesta, J. E. Betancort-Rijo, and J. Primack. Halo concentrations in the standard Λ cold dark matter cosmology. MNRAS, 423: 3018–3030, July 2012. doi: 10.1111/j.1365-2966.2012.21007.x.

W. H. Press and P. Schechter. Formation of Galaxies and Clusters of Galaxies by Self-Similar Gravitational Condensation. ApJ, 187:425–438, February 1974. doi: 10.1086/152650.

C. W. Purcell and A. R. Zentner. Bailing out the Milky Way: variation in the properties of massive dwarfs among galaxy-sized systems. JCAP, 12:007, December 2012. doi: 10.1088/1475-7516/2012/12/007.

M. Ricotti. Dependence of the inner dark matter profile on the halo mass. MNRAS, 344:1237–1249, October 2003. doi: 10.1046/j.1365-8711.2003.06910.x.

M. Ricotti. Late gas accretion on to primordial minihaloes: a model for Leo T, dark galaxies and extragalactic high-velocity clouds. MNRAS, 392:L45–L49, January 2009. doi: 10.1111/j.1745-3933.2008.00586.x.

M. Ricotti. The First Galaxies and the Likely Discovery of Their Fossils in the Local Group. *Advances in Astronomy*, 2010, 2010. doi: 10.1155/2010/271592.

M. Ricotti and N. Y. Gnedin. Formation Histories of Dwarf Galaxies in the Local Group. ApJ, 629:259–267, August 2005a. doi: 10.1086/431415.

M. Ricotti and N. Y. Gnedin. Formation Histories of Dwarf Galaxies in the Local Group. ApJ, 629:259–267, August 2005b. doi: 10.1086/431415.

M. Ricotti and J. P. Ostriker. X-ray pre-ionization powered by accretion on the first black holes - I. A model for the WMAP polarization measurement. MNRAS, 352: 547–562, August 2004. doi: 10.1111/j.1365-2966.2004.07942.x.

M. Ricotti, N. Y. Gnedin, and J. M. Shull. The Evolution of the Effective Equation of State of the Intergalactic Medium. ApJ, 534:41–56, May 2000. doi: 10.1086/308733.

M. Ricotti, N. Y. Gnedin, and J. M. Shull. The Fate of the First Galaxies. II. Effects of Radiative Feedback. ApJ, 575:49–67, August 2002a. doi: 10.1086/341256.

M. Ricotti, N. Y. Gnedin, and J. M. Shull. The Fate of the First Galaxies. I. Self-consistent Cosmological Simulations with Radiative Transfer. ApJ, 575:33–48, August 2002b. doi: 10.1086/341255.

M. Ricotti, J. P. Ostriker, and N. Y. Gnedin. X-ray pre-ionization powered by accretion on the first black holes - II. Cosmological simulations and observational signatures. MNRAS, 357:207–219, February 2005. doi: 10.1111/j.1365-2966.2004.08623.x.

M. Ricotti, A. Pontzen, and M. Viel. Is the Concentration of Dark Matter Halos at Virialization Universal? ApJ, 663:L53–L56, July 2007. doi: 10.1086/520113.

M. Ricotti, N. Y. Gnedin, and J. M. Shull. The Fate of the First Galaxies. III. Properties of Primordial Dwarf Galaxies and Their Impact on the Intergalactic Medium. ApJ, 685:21–39, September 2008a. doi: 10.1086/590901.

M. Ricotti, N. Y. Gnedin, and J. M. Shull. The Fate of the First Galaxies. III. Properties of Primordial Dwarf Galaxies and Their Impact on the Intergalactic Medium. ApJ, 685:21–39, September 2008b. doi: 10.1086/590901.

S. Riemer-Sørensen and S. H. Hansen. Decaying dark matter in the Draco dwarf galaxy. A&A, 500:L37–L40, June 2009. doi: 10.1051/0004-6361/200912430.

S. Riemer-Sørensen, S. H. Hansen, and K. Pedersen. Sterile Neutrinos in the Milky Way: Observational Constraints. ApJ, 644:L33–L36, June 2006. doi: 10.1086/505330.

S. Riemer-Sorensen, K. Pedersen, S. H. Hansen, and H. Dahle. Probing the nature of dark matter with cosmic x rays: Constraints from "dark blobs" and grating spectra of galaxy clusters. Phys. Rev. D, 76(4):043524–+, August 2007. doi: 10.1103/PhysRevD.76.043524.

V. C. Rubin, N. Thonnard, and W. K. Ford, Jr. Extended rotation curves of high-luminosity spiral galaxies. IV - Systematic dynamical properties, SA through SC. ApJ, 225:L107–L111, November 1978. doi: 10.1086/182804.

P. Salucci, A. Lapi, C. Tonini, G. Gentile, I. Yegorova, and U. Klein. The universal rotation curve of spiral galaxies - II. The dark matter distribution out to the virial radius. MNRAS, 378:41–47, June 2007. doi: 10.1111/j.1365-2966.2007.11696.x.

T. Sawala, C. S. Frenk, R. A. Crain, A. Jenkins, J. Schaye, T. Theuns, and J. Zavala. The abundance of (not just) dark matter haloes. *ArXiv e-prints*, June 2012.

J. Schaye, T. Theuns, M. Rauch, G. Efstathiou, and W. L. W. Sargent. The thermal history of the intergalactic medium*. MNRAS, 318:817–826, November 2000. doi: 10.1046/j.1365-8711.2000.03815.x.

K. B. Schmidt, S. H. Hansen, and A. V. Macciò. Alas, the Dark Matter Structures Were Not That Trivial. ApJ, 689:L33–L36, December 2008. doi: 10.1086/595783.

A. Schneider, D. Anderhalden, A. Maccio, and J. Diemand. Warm Dark Matter: The End is Nigh. *ArXiv e-prints*, September 2013.

C. Schultz, J. Oñorbe, K. N. Abazajian, and J. S. Bullock. The High-z Universe Confronts Warm Dark Matter: Galaxy Counts, Reionization and the Nature of Dark Matter. *ArXiv e-prints*, January 2014.

U. Seljak, A. Makarov, P. McDonald, and H. Trac. Can Sterile Neutrinos Be the Dark Matter? Phys. Rev. Lett., 97(19):191303–+, November 2006. doi: 10.1103/PhysRevLett.97.191303.

Uros Seljak and Matias Zaldarriaga. A line of sight approach to cosmic microwave background anisotropies. *Astrophys. J.*, 469:437–444, 1996.

X. Shi and G. M. Fuller. New Dark Matter Candidate: Nonthermal Sterile Neutrinos. Phys. Rev. Lett., 82:2832–2835, April 1999. doi: 10.1103/PhysRevLett.82.2832.

M. H. Siegel, M. D. Shetrone, and M. Irwin. Trimming Down the Willman 1 dSph. AJ, 135:2084–2094, June 2008. doi: 10.1088/0004-6256/135/6/2084.

K. Sigurdson and M. Kamionkowski. Charged-Particle Decay and Suppression of Primordial Power on Small Scales. Phys. Rev. Lett., 92(17):171302–+, April 2004. doi: 10.1103/PhysRevLett.92.171302.

J. D. Simon and M. Geha. The Kinematics of the Ultra-faint Milky Way Satellites: Solving the Missing Satellite Problem. ApJ, 670:313–331, November 2007. doi: 10.1086/521816.

J. D. Simon, A. D. Bolatto, A. Leroy, L. Blitz, and E. L. Gates. High-Resolution Measurements of the Halos of Four Dark Matter-Dominated Galaxies: Deviations from a Universal Density Profile. ApJ, 621:757–776, March 2005. doi: 10.1086/427684.

J. Sommer-Larsen and A. Dolgov. Formation of Disk Galaxies: Warm Dark Matter and the Angular Momentum Problem. ApJ, 551:608–623, April 2001. doi: 10.1086/320211.

M. Sorel, J. M. Conrad, and M. H. Shaevitz. Combined analysis of short-baseline neutrino experiments in the (3+1) and (3+2) sterile neutrino oscillation hypotheses. Phys. Rev. D, 70(7):073004–+, October 2004. doi: 10.1103/PhysRevD.70.073004.

D. N. Spergel, L. Verde, H. V. Peiris, E. Komatsu, M. R. Nolta, C. L. Bennett, M. Halpern, G. Hinshaw, N. Jarosik, A. Kogut, M. Limon, S. S. Meyer, L. Page, G. S. Tucker, J. L. Weiland, E. Wollack, and E. L. Wright. First-Year Wilkinson Microwave Anisotropy Probe (WMAP) Observations: Determination of Cosmological Parameters. ApJS, 148:175–194, September 2003. doi: 10.1086/377226.

D. N. Spergel, R. Bean, O. Doré, M. R. Nolta, C. L. Bennett, J. Dunkley, G. Hinshaw, N. Jarosik, E. Komatsu, L. Page, H. V. Peiris, L. Verde, M. Halpern, R. S. Hill, A. Kogut, M. Limon, S. S. Meyer, N. Odegard, G. S. Tucker, J. L. Weiland, E. Wollack, and E. L. Wright. Three-Year Wilkinson Microwave Anisotropy Probe (WMAP) Observations: Implications for Cosmology. ApJS, 170:377–408, June 2007. doi: 10.1086/513700.

V. Springel. The cosmological simulation code GADGET-2. MNRAS, 364:1105–1134, December 2005. doi: 10.1111/j.1365-2966.2005.09655.x.

V. Springel, S. D. M. White, G. Tormen, and G. Kauffmann. Populating a cluster of galaxies - I. Results at [formmu2]z=0. MNRAS, 328:726–750, December 2001. doi: 10.1046/j.1365-8711.2001.04912.x.

V. Springel, J. Wang, M. Vogelsberger, A. Ludlow, A. Jenkins, A. Helmi, J. F. Navarro, C. S. Frenk, and S. D. M. White. The Aquarius Project: the subhaloes of galactic haloes. MNRAS, 391:1685–1711, December 2008. doi: 10.1111/j.1365-2966.2008.14066.x.

F. Stoehr, S. D. M. White, G. Tormen, and V. Springel. The satellite population of the Milky Way in a ΛCDM universe. MNRAS, 335:L84–L88, October 2002. doi: 10.1046/j.1365-8711.2002.05891.x.

M. Su and D. P. Finkbeiner. Strong Evidence for Gamma-ray Line Emission from the Inner Galaxy. *ArXiv e-prints*, June 2012.

K. Subramanian, R. Cen, and J. P. Ostriker. The Structure of Dark Matter Halos in Hierarchical Clustering Theories. ApJ, 538:528–542, August 2000. doi: 10.1086/309152.

R. A. Swaters, B. F. Madore, F. C. van den Bosch, and M. Balcells. The Central Mass Distribution in Dwarf and Low Surface Brightness Galaxies. ApJ, 583: 732–751, February 2003. doi: 10.1086/345426.

D. Syer and S. D. M. White. Dark halo mergers and the formation of a universal profile. MNRAS, 293:337, February 1998. doi: 10.1046/j.1365-8711.1998.01285.x.

J. E. Taylor and J. F. Navarro. The Phase-Space Density Profiles of Cold Dark Matter Halos. ApJ, 563:483–488, December 2001. doi: 10.1086/324031.

A. A. Thoul and D. H. Weinberg. Hydrodynamic Simulations of Galaxy Formation. II. Photoionization and the Formation of Low-Mass Galaxies. ApJ, 465:608–+, July 1996. doi: 10.1086/177446.

E. J. Tollerud, J. S. Bullock, L. E. Strigari, and B. Willman. Hundreds of Milky Way Satellites? Luminosity Bias in the Satellite Luminosity Function. ApJ, 688: 277–289, November 2008. doi: 10.1086/592102.

F. C. van den Bosch and R. A. Swaters. Dwarf galaxy rotation curves and the core problem of dark matter haloes. MNRAS, 325:1017–1038, August 2001. doi: 10.1046/j.1365-8711.2001.04456.x.

F. C. van den Bosch, G. Tormen, and C. Giocoli. The mass function and average mass-loss rate of dark matter subhaloes. MNRAS, 359:1029–1040, May 2005. doi: 10.1111/j.1365-2966.2005.08964.x.

C. A. Vera-Ciro, A. Helmi, E. Starkenburg, and M. A. Breddels. Not too big, not too small: the dark haloes of the dwarf spheroidals in the Milky Way. MNRAS, 428:1696–1703, January 2013. doi: 10.1093/mnras/sts148.

J. Viñas, E. Salvador-Solé, and A. Manrique. Typical density profile for warm dark matter haloes. MNRAS, 424:L6–L10, July 2012. doi: 10.1111/j.1745-3933.2012.01274.x.

M. Viel, J. Lesgourgues, M. G. Haehnelt, S. Matarrese, and A. Riotto. Constraining warm dark matter candidates including sterile neutrinos and light gravitinos with WMAP and the Lyman-α forest. Phys. Rev. D, 71(6):063534–+, March 2005. doi: 10.1103/PhysRevD.71.063534.

M. Viel, J. Lesgourgues, M. G. Haehnelt, S. Matarrese, and A. Riotto. Can Sterile Neutrinos Be Ruled Out as Warm Dark Matter Candidates? Phys. Rev. Lett., 97(7):071301–+, August 2006. doi: 10.1103/PhysRevLett.97.071301.

M. Viel, G. D. Becker, J. S. Bolton, M. G. Haehnelt, M. Rauch, and W. L. W. Sargent. How Cold Is Cold Dark Matter? Small-Scales Constraints from the Flux Power Spectrum of the High-Redshift Lyman-α Forest. Phys. Rev. Lett., 100(4): 041304–+, February 2008. doi: 10.1103/PhysRevLett.100.041304.

M. Viel, J. S. Bolton, and M. G. Haehnelt. Cosmological and astrophysical constraints from the Lyman α forest flux probability distribution function. MNRAS, 399:L39–L43, October 2009. doi: 10.1111/j.1745-3933.2009.00720.x.

M. Viel, G. D. Becker, J. S. Bolton, and M. G. Haehnelt. Warm dark matter as a solution to the small scale crisis: New constraints from high redshift Lyman-α forest data. Phys. Rev. D, 88(4):043502, August 2013. doi: 10.1103/PhysRevD.88.043502.

M. Vogelsberger, J. Zavala, and A. Loeb. Subhaloes in self-interacting galactic dark matter haloes. MNRAS, 423:3740–3752, July 2012. doi: 10.1111/j.1365-2966.2012.21182.x.

M. G. Walker, M. Mateo, E. W. Olszewski, J. Peñarrubia, N. Wyn Evans, and G. Gilmore. A Universal Mass Profile for Dwarf Spheroidal Galaxies? ApJ, 704: 1274–1287, October 2009. doi: 10.1088/0004-637X/704/2/1274.

S. M. Walsh, H. Jerjen, and B. Willman. A Pair of Boötes: A New Milky Way Satellite. ApJ, 662:L83–L86, June 2007. doi: 10.1086/519684.

S. M. Walsh, B. Willman, and H. Jerjen. The Invisibles: A Detection Algorithm to Trace the Faintest Milky Way Satellites. AJ, 137:450–469, January 2009. doi: 10.1088/0004-6256/137/1/450.

J. Wang and S. D. M. White. Discreteness effects in simulations of hot/warm dark matter. MNRAS, 380:93–103, September 2007. doi: 10.1111/j.1365-2966.2007.12053.x.

J. Wang and S. D. M. White. Are mergers responsible for universal halo properties? MNRAS, 396:709–717, June 2009. doi: 10.1111/j.1365-2966.2009.14755.x.

J. Wang, C. S. Frenk, J. F. Navarro, L. Gao, and T. Sawala. The missing massive satellites of the Milky Way. MNRAS, 424:2715–2721, August 2012. doi: 10.1111/j.1365-2966.2012.21357.x.

L. L. Watkins, N. W. Evans, V. Belokurov, M. C. Smith, P. C. Hewett, D. M. Bramich, G. F. Gilmore, M. J. Irwin, S. Vidrih, Ł. Wyrzykowski, and D. B. Zucker. Substructure revealed by RRLyraes in SDSS Stripe 82. MNRAS, 398: 1757–1770, October 2009. doi: 10.1111/j.1365-2966.2009.15242.x.

C. R. Watson, J. F. Beacom, H. Yüksel, and T. P. Walker. Direct x-ray constraints on sterile neutrino warm dark matter. Phys. Rev. D, 74(3):033009–+, August 2006. doi: 10.1103/PhysRevD.74.033009.

C. R. Watson, Z. Li, and N. K. Polley. Constraining sterile neutrino warm dark matter with Chandra observations of the Andromeda galaxy. JCAP, 3:018, March 2012. doi: 10.1088/1475-7516/2012/03/018.

R. H. Wechsler, J. S. Bullock, J. R. Primack, A. V. Kravtsov, and A. Dekel. Concentrations of Dark Halos from Their Assembly Histories. ApJ, 568:52–70, March 2002. doi: 10.1086/338765.

D. T. F. Weldrake, W. J. G. de Blok, and F. Walter. A high-resolution rotation curve of NGC 6822: a test-case for cold dark matter. MNRAS, 340:12–28, March 2003. doi: 10.1046/j.1365-8711.2003.06170.x.

C. Weniger. A tentative gamma-ray line from Dark Matter annihilation at the Fermi Large Area Telescope. JCAP, 8:007, August 2012. doi: 10.1088/1475-7516/2012/08/007.

S. D. M. White. Violent Relaxation in Hierarchical Clustering. In O. Lahav, E. Terlevich, and R. J. Terlevich, editors, *Gravitational dynamics*, page 121, 1996.

R. J. Wilkinson, J. Lesgourgues, and C. Boehm. Using the CMB angular power spectrum to study Dark Matter-photon interactions. *ArXiv e-prints*, September 2013.

L. L. R. Williams, A. Babul, and J. J. Dalcanton. Investigating the Origins of Dark Matter Halo Density Profiles. ApJ, 604:18–39, March 2004. doi: 10.1086/381722.

B. Willman, M. R. Blanton, A. A. West, J. J. Dalcanton, D. W. Hogg, D. P. Schneider, N. Wherry, B. Yanny, and J. Brinkmann. A New Milky Way Companion: Unusual Globular Cluster or Extreme Dwarf Satellite? AJ, 129:2692–2700, June 2005. doi: 10.1086/430214.

J. Wolf, G. D. Martinez, J. S. Bullock, M. Kaplinghat, M. Geha, R. R. Muñoz, J. D. Simon, and F. F. Avedo. Accurate masses for dispersion-supported galaxies. MNRAS, 406:1220–1237, August 2010. doi: 10.1111/j.1365-2966.2010.16753.x.

Y. B. Zel'dovich. Gravitational instability: An approximate theory for large density perturbations. A&A, 5:84–89, March 1970.

A. R. Zentner and J. S. Bullock. Halo Substructure and the Power Spectrum. ApJ, 598:49–72, November 2003. doi: 10.1086/378797.

D. H. Zhao, Y. P. Jing, H. J. Mo, and G. Börner. Mass and Redshift Dependence of Dark Halo Structure. ApJ, 597:L9–L12, November 2003a. doi: 10.1086/379734.

D. H. Zhao, H. J. Mo, Y. P. Jing, and G. Börner. The growth and structure of dark matter haloes. MNRAS, 339:12–24, February 2003b. doi: 10.1046/j.1365-8711.2003.06135.x.

D. H. Zhao, Y. P. Jing, H. J. Mo, and G. Börner. Accurate Universal Models for the Mass Accretion Histories and Concentrations of Dark Matter Halos. ApJ, 707: 354–369, December 2009. doi: 10.1088/0004-637X/707/1/354.

A. Zolotov, A. M. Brooks, B. Willman, F. Governato, A. Pontzen, C. Christensen, A. Dekel, T. Quinn, S. Shen, and J. Wadsley. Baryons Matter: Why Luminous Satellite Galaxies have Reduced Central Masses. ApJ, 761:71, December 2012. doi: 10.1088/0004-637X/761/1/71.

D. B. Zucker, V. Belokurov, N. W. Evans, M. I. Wilkinson, M. J. Irwin, T. Sivarani, S. Hodgkin, D. M. Bramich, J. M. Irwin, G. Gilmore, B. Willman, S. Vidrih, M. Fellhauer, P. C. Hewett, T. C. Beers, E. F. Bell, E. K. Grebel, D. P. Schneider, H. J. Newberg, R. F. G. Wyse, C. M. Rockosi, B. Yanny, R. Lupton, J. A. Smith, J. C. Barentine, H. Brewington, J. Brinkmann, M. Harvanek, S. J. Kleinman, J. Krzesinski, D. Long, A. Nitta, and S. A. Snedden. A New Milky Way Dwarf Satellite in Canes Venatici. ApJ, 643:L103–L106, June 2006. doi: 10.1086/505216.

F. Zwicky. Die Rotverschiebung von extragalaktischen Nebeln. *Helvetica Physica Acta*, 6:110–127, 1933.

F. Zwicky. On the Masses of Nebulae and of Clusters of Nebulae. ApJ, 86:217, October 1937. doi: 10.1086/143864.